January 1996

Model-Based Shape and Motion Analysis: Left Ventricle of a Heart

Jinah Park
University of Pennsylvania

University of Pennsylvania Institute for Research in Cognitive Science Technical Report No. IRCS-96-33.

Model-Based Shape and Motion Analysis: Left Ventricle of a Heart

Abstract
The accurate and clinically useful estimation of the shape, motion, and deformation of the left ventricle of a heart (LV) is an important yet open research problem. Recently, computer vision techniques for reconstructing the 3-D shape and motion of the LV have been developed. The main drawback of these techniques, however, is that their models are formulated in terms of either too many local parameters that require non-trivial processing to be useful for close to real time diagnosis, or too few parameters to offer an adequate approximation to the LV motion.

To address the problem, we present a new class of volumetric primitives for a compact and accurate LV shape representation in which model parameters are *functions*. Lagrangian dynamics are employed to convert geometric models into dynamic models that can deform according to the forces manifested in the data points. It is thus possible to make a precise estimation of the deformation of the LV shape endocardial, epicardial and anywhere in between with a small number of intuitive parameter functions.

We believe that the proposed technique has a wide range of potential applications. In this thesis, we demonstrate the possibility by applying it to the 3-D LV shape and motion characterization from magnetic tagging data (MRI-SPAMM). We show that the results of our experiments with normal and abnormal heart data enable us to quantitatively verify the physicians' qualitative conception of the left ventricular wall motion.

Comments
University of Pennsylvania Institute for Research in Cognitive Science Technical Report No. IRCS-96-33.

MODEL-BASED SHAPE AND MOTION ANALYSIS: LEFT VENTRICLE OF A HEART

JINAH PARK

A DISSERTATION

in

COMPUTER AND INFORMATION SCIENCE

Presented to the Faculties of the University of Pennsylvania in Partial Fulfillment of the Requirements for the Degree of Doctor of Philosophy

1996

Dimitris N. Metaxas

Supervisor of Dissertation

Peter Buneman

Graduate Group Chairperson

In Memory of

My Beloved Aunt

고 모

Acknowledgments

Looking back upon the years at Penn for my Ph.D studies, my heart is filled with immense gratitude towards all the professors, researchers, physicians, friends and family who have supported and encouraged me against all odds. Without any single one of them, I wouldn't be who I am now.

The first person who comes to my mind is Dr. Bernice Rogowitz, my former manager at IBM Thomas J. Watson Research Center, who strongly encouraged me to return to school to pursue a Ph.D degree. I feel fortunate to have her blessings since the beginning of my studies.

My first year at Penn was rather tough, due to the lack of any basic computer science background. However, I managed to get through with a lot of help from Prof. K. Wohn and many good friends like Anand, Craig, Haresh, Hyun, Mani, Robbie, Roh and Susan. Special thanks to Haresh Assumal who patiently showed me all about the UNIX system, and Susan Nowicki who always invited me to study groups.

With unconditional support from Prof. Norm Badler, I have met Dr. Eric Hoffman at Radiology Department who introduced me to the exciting field of cardiothoracic imaging and its potential. I can never forget our late night studies on dogs at the Hospital of U. Penn and his wonderful devotion to the field. His moral support throughout the years, even after he left Penn for Iowa as the chief of Physiologic Imaging, has provided me with the energy to move forward.

I am very grateful to Dr. Ken Fellows, the chief of Radiology at the Children's Hospital of Philadelphia, for his generous support and faith. Without his financial support, it would not have been possible for me to continue my Ph.D work. I also feel very lucky to work

with many wonderful people at the Children's Hospital, especially Dr. Paul Weinberg at Cardiology whom I respect very much for his role as a bridge between clinicians and computer scientists. The kind words from Dr. Sue Kramer have always perked me up, Dr. Zimmerman's Christmas dinners gave me a sense of belonging, meetings with Dr. Haselgrove always gave me something to think about, and small talks with Alison, Brent, Doug, Jerry, Jill, John, Lou, Mammie, Mark, Pat, and Val kept me going everyday at the MRI computer room. Thanks to Daniel who helped me resolve most of the hardware problems over the phone. I also feel very lucky to work closely with the free-minded C-expert John Hoford with whom I had many interesting discussions.

I would like to thank Prof. Dimitris Metaxas for bringing the physics-based modeling framework to Penn, and for sharing his interests in medical applications with me. Throughout the years of developing my thesis, his guidance and protection were enormous. I should also thank him for pushing me very hard to publish the work. His openness has allowed me to closely observe many sides of the academic life. I am very lucky to have him as my thesis advisor.

I cannot begin to express my gratitude towards Dr. Alistair Young, who is currently at the University of Auckland in New Zealand, for all his initiation and insights which became the seeds of my thesis. His noble stance as a researcher has been, and will continue to be, the model that I aspire to have.

My unlimited thanks also go to Dan, Zahi, Chang and Dara who have given me a full-hearted help every time I requested for image data sets - especially to Dan Bloomgarden for all his time and effort in gel phantom experiments.

No one will argue that I had a remarkable thesis committee. It was my great honor to have Prof. Norm Badler as the chair. Although I was working mostly alone on a medical application in CIS department, his consistent support in every aspect made me always feel at home in the department during the studies. I feel very lucky to have on my thesis committee Dr. Leon Axel, the exemplary physician and researcher in Cardiac Imaging, and I very much look forward to working with him more closely in the forthcoming years of my postdoctoral training. Very special thanks go to Prof. Jean Gallier who makes everything so wonderfully French and taught me how to appreciate the beauty of the theory and

mathematics. My most sincere respect goes to my external committee member, Dr. Jim Duncan at Yale University. His incredible encouragement has allowed me to grow and to see what lies beyond.

I also would like to thank Prof. Bonnie Webber who has been watching over me from a distance with great support in her eyes, and Prof. Insup Lee and his wife for their hospitality. I also owe many thanks to many SeonBaeNimDul, DongRyoDul and HooBaeNimDul who made the life at Penn so comfortable to make me forget that I am far away from Korea.

While spending most of my time at the Center for Human Modeling and Simulation (Graphics Lab) working on my thesis, I was very fortunate to get to know so many wonderful friends - especially Doug DeCarlo who knows almost everything about the system and software, Bond-Jay Ting who can fix almost anything in our office, Jonathan Kaye whose humor sometimes goes beyond our perception, the late-night worker and proof-reader Nick Foster and the most-helpful Ken Noble who has never complained about the last minute video productions. There are many more friends who made my life at Penn so much diverse and exciting - Angela, Barry, Brett, Christine, Diane, Donna, Edith, Emily, Frances, Gopal, Hannen, Ioannis, Jeff, Julie, Karen, Kris, Libby, Limsoon, Michael, Nan, Nobo, Paul, Paula, Pei-Hwa, Rama, Susan, Sylvia, Ulf, Wallace, Xinmin, etc. ...

I do not know how to thank my father and mother for their great love and faith in me all these years of my life, and my sisters and brothers for their love and support. I feel most blessed to have wonderful parents-in-law who have also nurtured me with at least the same amount of love and respect. I am also grateful to my beloved aunt who had prayed for my well-being until she passed onto the heaven shortly after my thesis defense. The fond memory of her will always be cherished. The very person I am most indebted to is Jong, my husband and my best friend. He is the one who has been always there to partake in all my hardships and to celebrate every single joyous moment in my days and nights at Penn. I thank God for His blessing in allowing Jong to be my life-time partner. I would like to dedicate my dissertation to my family especially to my husband Jong.

Abstract

MODEL-BASED SHAPE AND MOTION ANALYSIS: LEFT VENTRICLE OF A HEART

Jinah Park

Dimitris Metaxas

The accurate and clinically useful estimation of the shape, motion, and deformation of the left ventricle of a heart (LV) is an important yet open research problem. Recently, computer vision techniques for reconstructing the 3D shape and motion of the LV have been developed. The main drawback of these techniques, however, is that their models are formulated in terms of either too many local parameters that require non-trivial processing to be useful for close to real time diagnosis, or too few parameters to offer an adequate approximation to the LV motion.

To address the problem, we present a new class of volumetric primitives for a compact and accurate LV shape representation in which model parameters are *functions*. Lagrangian dynamics are employed to convert geometric models into dynamic models that can deform according to the forces manifested in the data points. It is thus possible to make a precise estimation of the deformation of the LV shape (endocardial, epicardial and anywhere in between) with a small number of intuitive parameter functions.

We believe that the proposed technique has a wide range of potential applications. In this thesis, we demonstrate the possibility by applying it to the 3-D LV shape and motion characterization from magnetic tagging data (MRI-SPAMM). We show that the results of our experiments with normal and abnormal heart data enable us to quantitatively verify the physicians' qualitative conception of the left ventricular wall motion.

Contents

List of Tables

List of Figures

Chapter 1

Introduction

1.1 Motivation

Alteration of heart wall motion is a sensitive indicator of heart disease such as ischemia [96], which is typically caused by occlusion of a coronary vessel: The local anemia caused by the obstruction of the blood supply results in abnormal ventricular wall motion even before any significant change can be detected from the electrocardiogram or clinical symptoms develop [69]. Moreover, abnormalities in heart wall motion are taken very seriously by clinicians because their extent can result in subsequent morbidity and mortality. However, since a heart undergoes such a complex motion during its cycle – e.g., the heart contracts, bends, twists, rotates, and translates during its systole – a proper characterization of its motion still remains an open and challenging research problem.

If we can derive the strain and stress distributions in myocardium from medical imaging modalities, the knowledge would provide us with a valuable insight into normal ventricular function. However, one of the main difficulties in assessing heart wall motion comes from the limitation of conventional cardiac imaging methods of providing *good* data sets. The obvious criterion for good image data is the signal-to-noise ratio. Although standard image processing techniques used in computer vision have been adapted to the medical imaging domain to improve the quality of the image, the gap between ideal image data and real world data is still too large. Another important criterion, especially for motion analyses, is the ability to obtain data correspondence between the images taken at subsequent time

phases. Recently, the introduction of a new technology in Magnetic Resonance Imaging (MRI) in conjunction with *magnetic tagging* [6, 116] has provided a potentially powerful tool for the study of heart wall motion. The MR tagging method provides a means to non-invasively mark and track a number of material points, and therefore provides a temporal correspondence for the material points on featureless structures like the heart wall. Unfortunately, the tagged MR images are not easily analyzed with simple qualitative viewing, especially for the 3-D motion. In addition, current quantitative analysis techniques are not only time consuming but yield data that may not be easily interpreted for diagnoses. This also leads us to the other main difficulty in assessing heart wall motion – the absence of computational techniques for automatic extraction of the three dimensional (3-D) heart wall motion parameters in a way that is *useful* to physicians. A precise model that can reflect the mechanics of ventricular myocardium would provide a better understanding of the complex regional changes under pathological conditions. Furthermore, it is also important that the model be constructed and analyzed in close to real-time to be useful in a clinical setting.

The goal of this thesis is to develop computational techniques for automatic extraction of the 3-D heart wall motion parameters that are not only compact but also can give accurate descriptions of ventricular function based on tagged MR images.

1.2 Problem Statement

Although there have been many computer vision and computer graphics techniques developed for reconstructing the 3-D shape and motion of the left ventricle of a heart (LV)[1] from medical image data, they still have major limitations as described below:

1. They are formulated in terms of either *many local parameters* that require non-trivial post-processing to be used by a physician or *very few parameters* that can offer only a gross approximation of the motion of a heart.

2. They do not capture the *twisting* motion of the heart, known to occur during systole.

[1] LV represents the main cardiac chamber since it has major role in the cardiovascular system [36], and it is where most effects of heart diseases appear.

3. Most of the techniques furnish only a surface model, while the heart muscle has a significant *volume*.

A natural approach to estimating the shape, motion, and deformations of an LV as accurately as possible is the use of a 3-D deformable model for the LV. The finite element representation is a popular choice. However, since it provides only a set of local measurements, it does not directly lend itself to understanding the underlying kinematics in such a way that is useful to physicians, i.e., compact, accurate and intuitive. In order to be able to describe the deformations of the LV in a way that is useful for clinical evaluation, we have developed a new class of physics-based *volumetric Deformable Models* whose *global Parameters* are *Functions* (or DMPF) [74, 76]. In this way, the shape and complex motion of the LV can be characterized with a few intuitive parameters such as the amount of contraction and the amount of twisting across and throughout the myocardium. We have utilized and further developed a physics-based framework for shape and motion analysis originally developed by Metaxas and Terzopoulos [60, 63], where the volumetric primitives are converted into models that deform due to forces exerted by the data points. In order to capture the twisting motion of the LV, we have utilized the data obtained from the MR tagging technique known as SPAMM (SPAtial Modulation of Magnetization) [6]. This fast, non-invasive technique promises to be very useful in the analysis of heart wall motion because it provides temporal correspondence for material points within the heart wall.

The crucial advantage of using the proposed DMPF in conjunction with tagged MRI data is that with a small number of parameters we will be able to characterize the shape and deformation of the heart in a physically intuitive way, in close to real time. None of the other current conventional imaging and modeling techniques can capture such 3-D motions, based on the above criteria.

1.3 Structure of the Dissertation

The thesis is presented in three parts. The first part discusses the main concepts and background of the thesis including model parameter functions, physics-based deformable models and MRI-SPAMM (Chapters 2-4). The second part reviews the related prior work and

develops the proposed LV model in the physics-based framework (Chapters 5-8). Finally, the third part describes the implementation of the thesis and the results from experiments involving shape and motion analysis of the LV during systole from MRI-SPAMM (Chapters 9-12).

The following is a very short summary of each chapter:

Chapter 1 Introduction :

We provide the motivation of the present thesis.

Chapter 2 Model Parameters :

We introduce the concept of model parameter functions which provide a powerful degrees of freedom in characterizing the shape of an object.

Chapter 3 Physics-Based Deformable Model :

We describe a general framework of physics-based modeling with Lagrangian dynamics.

Chapter 4 MRI-SPAMM :

We study the methods of obtaining data for cardiac motion analysis including the MRI-SPAMM data.

Chapter 5 Related Work on Heart Modeling :

We review various models of an LV developed by other researchers.

Chapter 6 Model Geometry :

We define the geometry of the proposed volumetric deformable models with parameter functions (DMPF) as LV models.

Chapter 7 Model Dynamics :

We develop the relevant algorithms for computing forces from the MRI-SPAMM data sets.

Chapter 8 Model Parameters :

We discuss in detail the interpretation for each parameter function of the DMPF.

Chapter 9 Feasibility Study :

We test our hypothesis that the complex LV motion can be described with a small number of intuitive parameters.

Chapter 10 Experiments :

We describe the experimental results with normal and abnormal heart data.

Chapter 11 Visualization :

We demonstrate visualization techniques for analyzing the motion of the LV.

Chapter 12 Validation :

We perform various experiments with deformable gel phantom for validation of the proposed technique.

Chapter 13 Conclusion :

We provide the list of contribution of the present thesis.

Part I

Theoretical Underpinnings

Part Overview

Throughout the first part of the thesis, we build the terminologies which are necessary to convey the main ideas of the dissertation. These include material coordinates, model parameters, global and local deformations, generalized coordinates, SPAMM data and material points. We first define the novel concept of *model parameter functions* in Chapter 2, and we present the general framework for the physics-based deformable models in Chapter 3, providing the chronology where the present thesis stands. Finally, MRI-SPAMM biomedical image data for cardiac motion studies are introduced in Chapter 4.

Chapter 2

Model Parameters

> "A representation is a formal system for making explicit certain entities or types of information, together with a specification of how the system does this. And I shall call the result of using a representation to describe a given entity a description of the entity in that representation." ([55]: p. 20)

2.1 Parameter Functions: A Simple Example

Consider Fig. 2.1(a). It shows a circular shape with five "bumps". In order to represent it, one could simply take a collection of a sufficient number of points on the curve. The set of sampled points as shown in Fig. 2.1(b) will enable us to reconstruct the original shape up to a certain degree. However, we can clearly see that it does not explicitly provide us

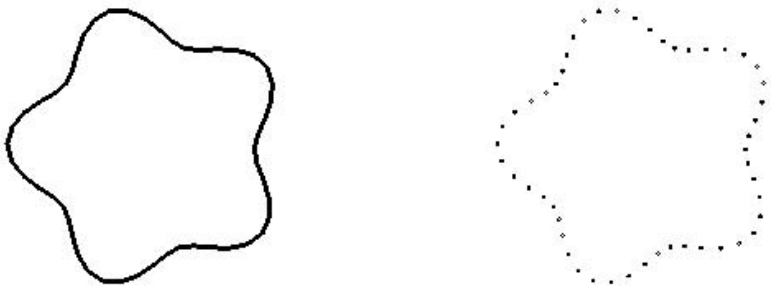

(a) (b)

Figure 2.1: Corolla

any interesting characteristics regarding the original shape.

We can instead view the shape as a deformed circle, and attempt to utilize the following parametric equation:

$$\mathbf{p} = \begin{bmatrix} p_x(u) \\ p_y(u) \end{bmatrix} = \begin{bmatrix} r(u)\cos u \\ r(u)\sin u \end{bmatrix}, \tag{2.1}$$

$$\text{and} \qquad r(u) = 1 - \gamma\cos(n\ u), \tag{2.2}$$

where $-\pi \leq u < \pi$, $\gamma = 0.15$, and $n = 5$.

We may call the primitive defined in (2.1) a *generalized circle*. $r(u)$ is the radius of the generalized circle. While $r(u)$ can be arbitrary, the formulation in (2.2) shows that it is considered to vary in a sinusoidal fashion dependent upon n and γ, which specify the number and the size of the ripples, respectively. For the shape in Fig. 2.1(a), n is set to 5 and γ is set to 0.15. The value of n tells us that it has 5 bumps, and the value of γ tells us that the size of bumps is 15% of the radius of the undeformed circle.

When we build an object model, we create the representation that can be easily handled and analyzed for certain tasks at hand. In this example, the intension was to capture the "bumpiness" of the shape. Fig. 2.2 demonstrates a series of shapes from a pentagon to a daisy. Such a family of curves can be obtained by varying γ while keeping $n = 5$. Inner bumps are created from a "negative" radius when $\gamma > 1.0$. If $0 < \gamma \ll 1$, we can create smooth-edged regular polygons (e.g., a triangle, a square, a pentagon, a hexagon, etc.) by increasing n as shown in Fig. 2.3. Fig. 2.4 shows more examples of the shapes created by varying the parameters.

2.2 Terminology (I)

In this thesis, vectors will be denoted by bold-faced letters like $\mathbf{x}$ or $\mathbf{u}$, and scalars will be denoted by italic letters like x or u.

2.2.1 Frame of Reference

The representation is given in an object-centered coordinate frame, so that the shape description does not depend on where the object is placed in a world coordinate frame or where it is viewed from.

- **inertial frame of reference :** three dimensional Cartesian space (X, Y, Z) whose origin and orientation defines the world coordinate frame. In short, it is called the inertial frame and and denoted by Φ.

- **model frame of reference :** three dimensional Cartesian space (x, y, z) where the model is defined. We define the model frame which is non-inertial[1] and object-centered. It is denoted by ϕ.

2.2.2 Material Coordinates

A model may be represented in a parameterized form [18]. A parameterization is a mapping $\Pi : \mathrm{U} \mapsto \Upsilon$ where $\mathrm{U} \subset \Re^m$ is an open set and $\Upsilon \subset \Re^n$ such that $m \leq n$ and Π is differentiable. If $m = 2$ and $n = 3$, for example, Π is a mapping from a two dimensional parameter space to a three dimensional Cartesian space. The following is such a parameterization of a surface in a three dimensional space:

$$\mathbf{p} = \mathbf{p}(u,v) = \begin{bmatrix} p_x(u,v) \\ p_y(u,v) \\ p_z(u,v) \end{bmatrix} \; ; \quad \mathbf{u} = \begin{bmatrix} u \\ v \end{bmatrix} \subset \Re^2 \tag{2.3}$$

where the Cartesian coordinates $\mathbf{p} = (p_x, p_y, p_z)$ of a surface point are differentiable functions of u and v. We write the auxiliary variables[2] u and v into a vector $\mathbf{u}$, and call them *material coordinates*. In order to avoid potential problems concerning the parameterization, we need a regular parameterization [17].

[1] Inertial system is a frame of reference where an object remains in its state of rest or its velocity as long as there is no external force. But for our application of shape recovery, we want to have a non-inertial model frame so that once the forces are gone the object stops moving/deforming.

[2] Conventionally, they are called parameters. However, we avoid the term in order not to be confused with the term 'model parameter'.

- **material coordinates :** intrinsic coordinates of a model. They are based on the parameterization of the object, and denoted by **u**.

2.2.3 Model Parameter Function

Let's consider a simple model of a sphere defined in its material coordinates (u, v) as shown below.

$$\mathbf{s} = \begin{bmatrix} R\cos u\cos v \\ R\cos u\sin v \\ R\sin u \end{bmatrix} \tag{2.4}$$

By setting the value for R, we can obtain the sphere with a specific radius. In fact, the only thing we are allowed to tweak in this model is the value of R. Therefore, we say that the model has 1 degree of freedom, namely via R which is a *model parameter*. If the model parameter is allowed to vary along the material coordinates, it is called a *model parameter function* [78]. An example model parameter function is $r(u)$ in the equations (2.1) and (2.2) in the previous section.

- **model parameters (or parameters) :** a set of variables used for the definition of a model. Each value of the (model) parameters restricts or determines the specific form of the model.

- **model parameter function (or parameter function) :** the model parameter which is defined as a function of **u**.

Utilizing model parameters, we can extract global properties of the object in a compact way. However, it may not have enough degrees of freedom to account for fine details. By carefully selecting a set of model parameter *functions* instead, we can capture the fine details of the shape more precisely without sacrificing compactness. This thesis develops such a technique applied to heart modeling.

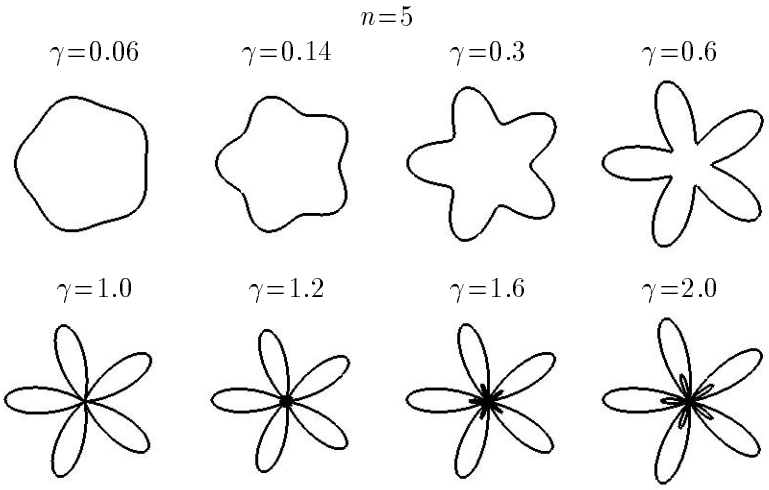

Figure 2.2: Radius as a parameter function (variation of γ)

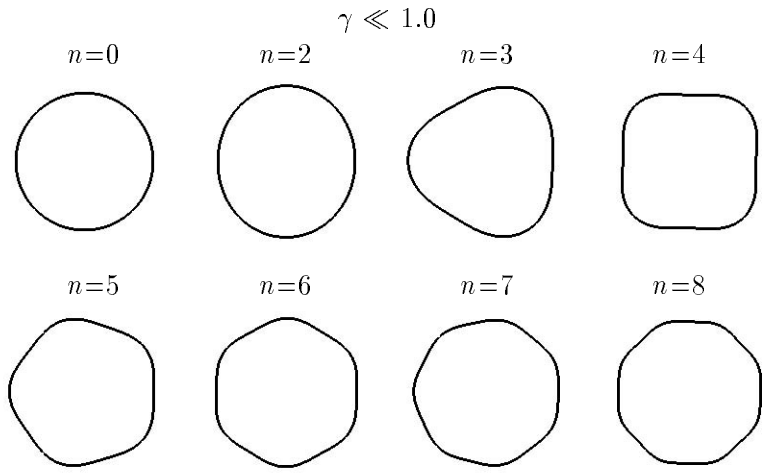

Figure 2.3: Radius as a parameter function (variation of n)

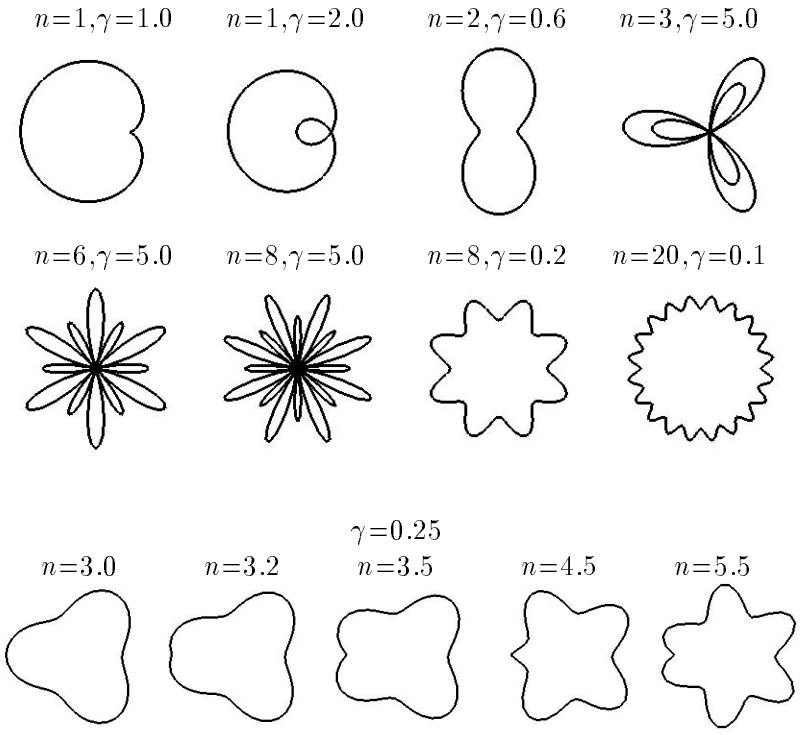

Figure 2.4: Radius as a parameter function (more examples)

Chapter 3

Physics-Based Deformable Model

> "One may think of a physical system, changing as time goes on from one state or configuration to another, as progressing along a particular evolutionary path, and ask, from this point of view, why it selects that particular path out of all the paths imaginable. The answer is that the physical system sums the values of its Lagrangian function for all the points along each imaginable path and then selects that path with the smallest result. This answer suggests that the Lagrangian function measures something analogous to increments of distance, in which case one may say, in an abstract way, that physical systems always take the shortest paths." ([20]: p. 102)

3.1 Brief History of Deformable Models

The history of the shape modeling based on physical principles goes back to the classical spline representation which is an abstraction of elasticity theory [30]. Coming from the Computer Vision discipline, the early work of Terzopoulos [97, 98], who employed variational models for visual surface reconstruction from visual constraints, has evolved into a physics-based modeling framework where the objects are modeled as elastically deformable bodies subject to continuum mechanical laws [102]. In late 1980's, together with other researchers such as Barr, Fleischer, Kass, Platt and Witkin, they delivered the *active* model – e.g., "symmetry-seeking model" [102] which is initially motivated by the generalized

cylinder idea [16], and the "snakes" [52] which is an energy-minimizing spline – into the Computer Vision community of the shape recovery and segmentation from image data.

Since the deformable models react to external forces and constraints, and are suitable for representing natural shapes, they have also attracted attention from Computer Graphics community where animation has been one of primary areas of research [101]. However, while the descriptive power of deformable models based on the generalized spline allows the representation of natural objects with asymmetries and fine details, it is very difficult to abstract the shape in a compact way.

Superellipsoid, which was first discovered by Peit Hein [38], was introduced to Computer Graphics by Barr [12] in the early 1980's. Barr further prescribed the hierarchical structure for deformations of superquadric primitives based on Jacobian matrices [13]. Superquadrics are a very powerful family of shapes, and yield a variety of useful forms based on model parameters. Starting in the late 1980's, many researchers [9, 19, 94, 81] in Computer Vision have utilized the superquadrics as primitives for shape representation.

In the early 1990's, Metaxas and Terzopoulos [61, 62, 63] developed a hybrid model named "deformable superquadrics" which is a product of combining superquadric ellipsoid subject to parameterized geometric bending and tapering with generalized splines represented by finite elements. While the local deformational degrees of freedom from finite elements allow one to render shape details, the global parameters in deformable superquadrics may be utilized for abstracting gross approximation of the shape. Their extended physics-based framework facilitates efficient modeling of non-rigid multi-body objects.

In this thesis, we have adapted the framework by Metaxas [60] where the geometric models are converted into dynamic models that deform due to forces exerted from the data points so as to conform to the given dataset. However, by proposing the formulation of model parameter functions [76], we have provided a means for capturing the local details in terms of a few parameters that can be utilized for shape and non-rigid motion analyses. We have been, therefore, able to capture the shape detail precisely using only the global parameter functions, without utilizing the large number of local parameters required for free-form deformations in the hybrid model of Metaxas. This new class of models is called

"deformable models with parameter functions" (DMPF). Furthermore, the DMPF has been extended to a volumetric model from a surface model and applied to cardiac motion analyses [74]. Fig. 3.1 depicts the chronology related to the thesis.

3.2 Terminology (II)

3.2.1 Deformation

The motion of a deformable body can be classified into two – rigid and non-rigid motion. Suppose $\mathbf{p}$ represents the points of a single-body[1] object at an initial time, and $\mathbf{p}'$ the corresponding points after experiencing some motion, where both $\mathbf{p}$ and $\mathbf{p}'$ are expressed with respect to the object-centered coordinate frame of reference.

$$\mathbf{p}' = \mathcal{M}(\mathbf{p}) \tag{3.1}$$

When the body experiences only rigid motion, the $\mathbf{p}$ and the corresponding $\mathbf{p}'$ are exactly the same and the distance of any two points of the body remains the same as that before the motion. Therefore, the rigid-motion can be described solely based on the kinematics of the local frame of reference. However, when the object undergoes a non-rigid motion, the shape of the body "deforms" so that the distance of any two points in the body no longer remains the same. In this case, the operation $\mathcal{M}$ will modify the coordinates of the points in space. We can apply $\mathcal{M}$ either *globally* based on parameters, or *locally* without imposing any constraints.

- **rigid motion :** shape invariant motion. These are translational and rotational motion.

- **deformation :** an operation which explicitly modifies the local coordinates of the points of a body as a result of non-rigid motion.

- **global deformation :** constraint deformation which is inherited from parameterized geometry. (e.g., scaling, bending, tapering, twisting)

- **local deformation :** free-form deformation

[1] In this thesis, we do not deal with multi-body systems.

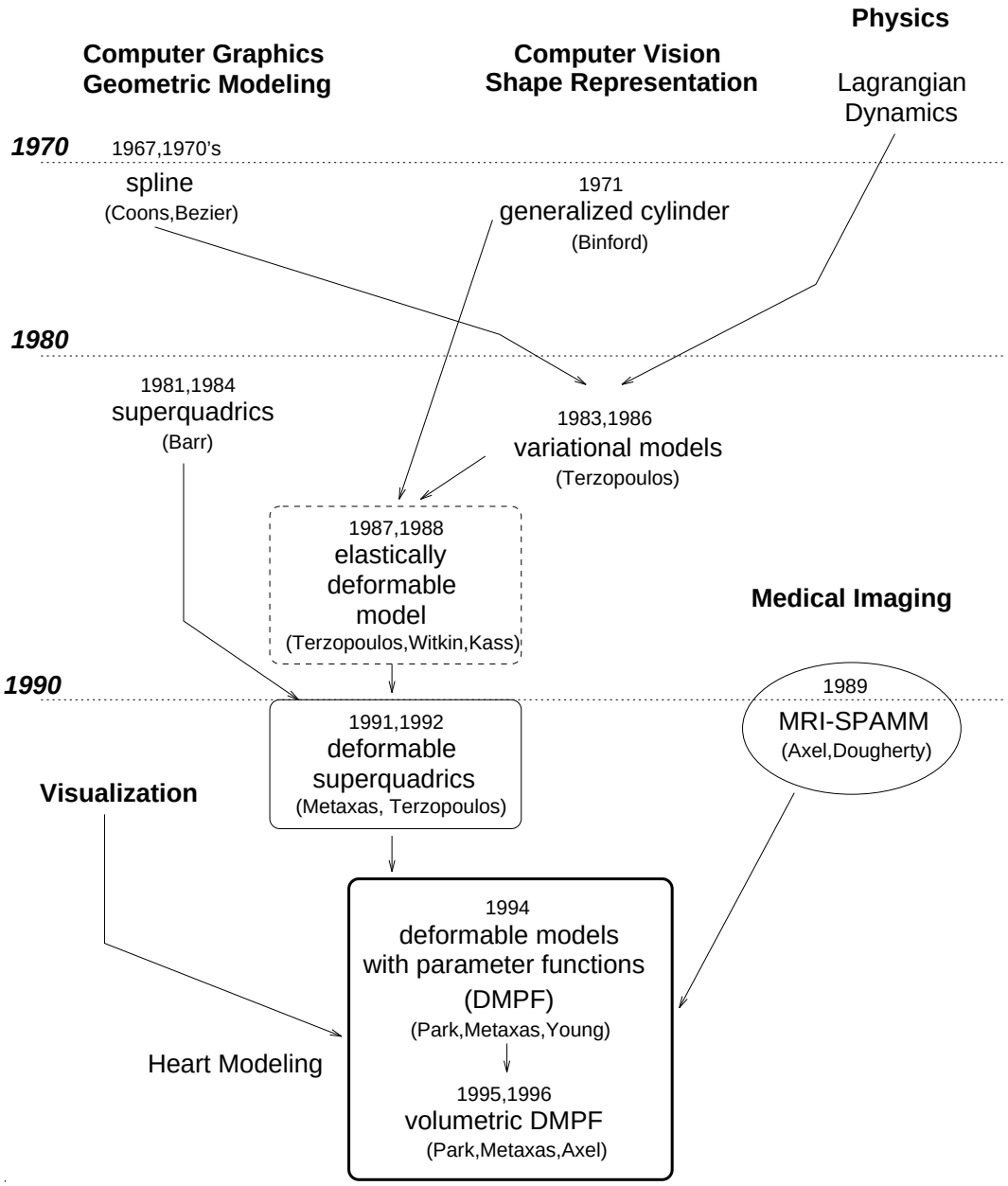

Figure 3.1: Chronology

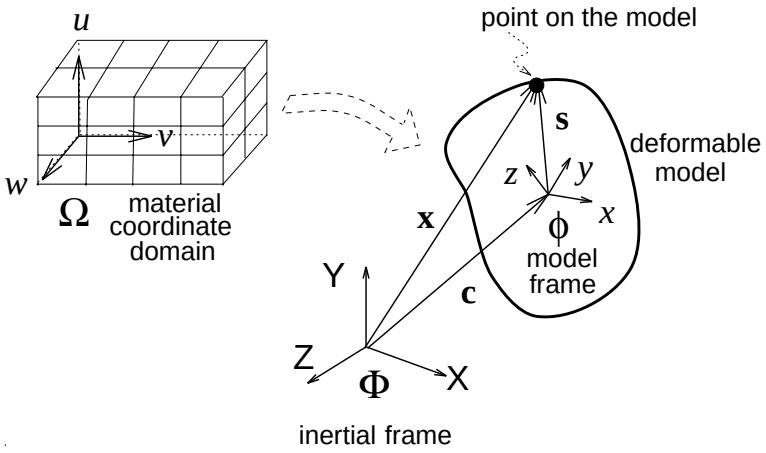

Figure 3.2: Geometry of a deformable model

3.2.2 Generalized Coordinates

Often the dynamics variables can be reduced to a set of a small number of independent *generalized coordinates*. For example, the configuration of a rigid-body can be completely described with six independent coordinates – three coordinates $\mathbf{q}_c$ for the location of the origin of the body and three rotational coordinates $\mathbf{q}_\theta$ for the orientation of the body with respect to a fixed frame [89]. For a deformable body we need deformation parameters $\mathbf{q}_s$ for non-rigid motion, in addition to $\mathbf{q}_c$ and $\mathbf{q}_\theta$ for rigid motion. These variables, written symbolically as $\mathbf{q} = (\mathbf{q}_c^\top, \mathbf{q}_\theta^\top, \mathbf{q}_s^\top)^\top$ where $^\top$ denotes transposition, are called the generalized coordinates of the system.

- **generalized coordinates :** a set of variables which completely define the location and orientation of each body in the system. These are put into a vector, denoted by $\mathbf{q}$.

3.3 Geometry of Deformable Models

The geometry of a 3-D deformable model is parametrically defined in the material coordinates $\mathbf{u} = (u, v, w)$ in domain Ω. The positions of points on the model relative to an inertial

frame of reference Φ in 3-D space are given by a vector-valued, time-varying function of $\mathbf{u}$:

$$\mathbf{x}(\mathbf{u},t) = \begin{bmatrix} x(\mathbf{u},t) \\ y(\mathbf{u},t) \\ z(\mathbf{u},t) \end{bmatrix}. \tag{3.2}$$

In order to decouple the rigid motion and non-rigid motion in our single-body system, we set up a non-inertial, model-centered reference frame ϕ and express the position of a point on a model as

$$\mathbf{x} = \mathbf{c} + \mathbf{R}\mathbf{s}, \tag{3.3}$$

where $\mathbf{c}(t)$ is the translation of the model defined at the origin of ϕ and $\mathbf{R}(t)$ is the rotation matrix which gives the orientation of ϕ relative to Φ. $\mathbf{s}(\mathbf{u},t)$ is the position of points on the model relative to the model frame (see Fig. 3.2).

The above equation (3.3) is an adapted definition of the hybrid model developed by Metaxas and Terzopoulos [60, 63, 100]. In [60], the position of a point on the model relative to the model frame[2] is expressed as the sum of a reference shape and a displacement function. For the DMPF, however, the displacement function (local deformations) is not necessary, since the reference shape is defined based on global parameter functions capable of capturing the local variation of the shape of an object.

In general, the reference shape is defined geometrically as follows:

$$\mathbf{s} = \mathbf{T}(\mathbf{e}(\mathbf{u};\alpha_0,\alpha_1,\ldots);\beta_0,\beta_1,\ldots), \tag{3.4}$$

where $\mathbf{e}(\mathbf{u};\alpha_0,\alpha_1,\ldots)$ or $\mathbf{e}$ is a geometric primitive defined parametrically in $\mathbf{u}$ and parameterized by the variables α_i. The shape represented by $\mathbf{e}$ is subject to the *deformation* $\mathbf{T}$ which depends on the deformation parameter functions β_i. Although generally nonlinear, $\mathbf{e}$ and $\mathbf{T}$ are assumed to be differentiable so that we may compute the Jacobian of $\mathbf{s}$. By concatenating these parameters α_i and β_i into the vector $\mathbf{q}_s$

$$\mathbf{q}_s = (\alpha_0,\alpha_1,\ldots,\beta_0,\beta_1,\ldots)^\top, \tag{3.5}$$

we collect the degrees of freedom of the model with respect to the deformation parameters. The Jacobian matrix is then computed as follows:

$$\mathbf{J} = \frac{\partial \mathbf{s}}{\partial \mathbf{q}_s} \tag{3.6}$$

[2] s in equation (3.3)

$\mathbf{T}$ may be a composite sequence of primitive deformation functions

$$\mathbf{T}(\mathbf{e}) = \mathbf{T}_n(\mathbf{T}_{n-1}(\ldots\mathbf{T}_2(\mathbf{T}_1(\mathbf{e})))). \tag{3.7}$$

When we apply multiple global deformations $(\mathbf{T}_1, \cdots, \mathbf{T}_n)$ to a shape primitive $\mathbf{e}$, it is much easier to compute the Jacobian $\mathbf{J}$ based on the chain rules rather than to compute it directly from complicated expressions of the shape $\mathbf{s}$. We can rewrite $\mathbf{q}_s$ in equation (3.5) by grouping the parameters as follows:

$$\begin{aligned} \mathbf{q}_s &= (\mathbf{q}_\alpha^\top, \mathbf{q}_\beta^\top)^\top \\ &= (\mathbf{q}_\alpha^\top, \mathbf{q}_{T_1}^\top, \mathbf{q}_{T_2}^\top, \cdots, \mathbf{q}_{T_n}^\top)^\top \end{aligned} \tag{3.8}$$

Let $\mathbf{s}_0 = \mathbf{e}$ and $\mathbf{s}_k = \mathbf{T}_k(\mathbf{s}_{k-1})$, where $1 \le k \le n$. Then we can compute $\mathbf{J}$ in a modular way using the following recurrence relations [31]:

$$\mathbf{J}_0 = \mathbf{J}_e = \frac{\partial \mathbf{e}}{\partial \mathbf{q}_\alpha} \tag{3.9}$$

$$\mathbf{J}_k = \left[\frac{\partial \mathbf{s}_k}{\partial \mathbf{s}_{k-1}} \mathbf{J}_{k-1} + \frac{\partial \mathbf{s}_k}{\partial \mathbf{q}_\alpha} \mid \frac{\partial \mathbf{s}_k}{\partial \mathbf{q}_{T_k}} \right] \qquad (1 \le k \le n) \tag{3.10}$$

$$\mathbf{J} = \mathbf{J}_n. \tag{3.11}$$

The parameters α_i and β_i of the DMPF are not constants [63, 100], but *functions* of $\mathbf{u}$:

$$\begin{aligned} \alpha_i &= \alpha_i(\mathbf{u}); \\ \beta_i &= \beta_i(\mathbf{u}). \end{aligned} \tag{3.12}$$

This definition allows us to generalize definitions of volumetric primitives (e.g., volumetric superquadrics) and parameterized deformations (e.g., twisting). It will be shown in the next part of the thesis and was demonstrated in [75, 78].

3.4 Kinematics of System

From equation (3.3), the velocity of points $\dot{\mathbf{x}} = \frac{d\mathbf{x}}{dt}$ on the model is given by,

$$\dot{\mathbf{x}} = \frac{d(\mathbf{c} + \mathbf{R}\mathbf{s})}{dt} \tag{3.13}$$

$$= \dot{\mathbf{c}} + \dot{\mathbf{R}}\mathbf{s} + \mathbf{R}\dot{\mathbf{s}}. \tag{3.14}$$

$\dot{\mathbf{s}}$, the time derivative of the shape primitive with respect to the model frame ϕ, can be written in terms of the model deformation parameters as follows:

$$\dot{\mathbf{s}} = \left[\frac{\partial \mathbf{s}}{\partial \mathbf{q}_s}\right] \dot{\mathbf{q}}_s = \mathbf{J}\ \dot{\mathbf{q}}_s, \tag{3.15}$$

where $\mathbf{J}$ is the Jacobian of the shape primitive.

In [89], Shabana showed that

$$\dot{\mathbf{R}}\mathbf{s} = -\mathbf{R}\ \tilde{\mathbf{s}}\ \mathbf{G}\ \dot{\boldsymbol{\theta}}, \tag{3.16}$$

where $\boldsymbol{\theta} = (\cdots, \theta_i, \cdots)^\top$ is the quaternion representation [23, 93] of rotational coordinates of the model; $\mathbf{G}$, also expressed in terms of quaternion representation, is derived from the time derivative of the angular velocity of the deformable model with respect to the model frame ϕ; and $\tilde{\mathbf{s}}$ is the dual 3×3 matrix of the position vector $\mathbf{s}$[3]. Therefore, we can rewrite (3.14) as follows:

$$\dot{\mathbf{x}} \quad = \quad \dot{\mathbf{c}} + \mathbf{B}\dot{\boldsymbol{\theta}} + \mathbf{R}\dot{\mathbf{s}}, \tag{3.19}$$

where

$$\mathbf{B} = \left[\cdots, \frac{\partial(\mathbf{R}\mathbf{s})}{\partial \theta_i}, \cdots\right] = -\mathbf{R}\ \tilde{\mathbf{s}}\ \mathbf{G}. \tag{3.20}$$

The corresponding rotation matrix $\mathbf{R}$ to a quaternion $\boldsymbol{\theta}$ is given in (B.1).

Finally, we can write (3.19) utilizing a matrix notation as follows:

$$\begin{aligned} \dot{\mathbf{x}} &= [\mathbf{I}\ \mathbf{B}\ \mathbf{R}\mathbf{J}]\ \dot{\mathbf{q}} \\ &= \mathbf{L}\ \dot{\mathbf{q}}, \end{aligned} \tag{3.21}$$

where

$$\mathbf{q} = (\mathbf{q}_c^\top, \mathbf{q}_\theta^\top, \mathbf{q}_s^\top)^\top, \tag{3.22}$$

[3] Let $\boldsymbol{\theta} = [\omega, \mathbf{v}] = (\omega, v_1, v_2, v_3)^\top$ and $\mathbf{s} = (s_1, s_2, s_3)^\top$. Then

$$\mathbf{G} \quad = \quad 2 \begin{bmatrix} -v_1 & \omega & v_3 & -v_2 \\ -v_2 & -v_3 & \omega & v_1 \\ -v_3 & v_2 & -v_1 & \omega \end{bmatrix}; \tag{3.17}$$

and

$$\tilde{\mathbf{s}} \quad = \quad \begin{bmatrix} 0 & -s_3 & s_2 \\ s_3 & 0 & s_1 \\ -s_2 & s_1 & 0 \end{bmatrix}. \tag{3.18}$$

with $\mathbf{q}_c = \mathbf{c}$ and $\mathbf{q}_\theta = \boldsymbol{\theta}$. $\mathbf{I}$ is an identity matrix. Intuitively, $\mathbf{L}$ is the model Jacobian matrix which maps the model's parameter space into the 3-D space.

The goal of fitting the model to data points is to recover the vector of degrees of freedom $\mathbf{q}$. This is achieved by carrying out the fitting procedure derived from Lagrangian dynamics – where the traction forces from data points are applied to the surface of the model [100].

3.5 Lagrangian Dynamics

When dealing with the dynamic problem of a system, we examine its dynamic parameters specifying both the potential energy of the system (which depends on the coordinates of all its particle) and the kinetic energy (which depends on their velocities). The Lagrangian dynamic formulation provides a means for deriving the equations of motion from the difference between the kinetic energy and the potential energy of the system [29].

The Lagrangian dynamics are expressed in terms of generalized coordinates $\mathbf{q}$ with associated *generalized force*. For a deformable body, we can make the model dynamic in $\mathbf{q}$ by introducing mass, damping, and a deformation strain energy. In general, the governing Lagrangian equations of motion[4] for a deformable body are second order differential equations given as follows:

$$\frac{d}{dt}\left(\frac{\partial \mathcal{T}}{\partial \dot{\mathbf{q}}}\right)^\top - \frac{d}{dt}\left(\frac{\partial \mathcal{T}}{\partial \mathbf{q}}\right)^\top + \frac{d}{dt}\left(\frac{\partial \mathcal{F}}{\partial \dot{\mathbf{q}}}\right)^\top + \delta_{\mathbf{q}}\mathcal{E} = \mathbf{f}_{\mathbf{q}} \tag{3.23}$$

where $\mathcal{T}$ is the kinetic energy of the deformable model, $\mathcal{F}$ is the kinetic energy dissipation, $\mathcal{E}$ is the deformation strain energy of the model, and $\mathbf{f}_{\mathbf{q}}$ is the generalized force. Utilizing a matrix notation, these equations can be written in the following form:

$$\mathbf{M}\ddot{\mathbf{q}} + \mathbf{D}\dot{\mathbf{q}} + \mathbf{K}\mathbf{q} = \mathbf{g}_q + \mathbf{f}_q, \tag{3.24}$$

where $\mathbf{M}$, $\mathbf{D}$ and $\mathbf{K}$ are the mass, damping and stiffness matrices, respectively. $\mathbf{g}_q$ are inertial forces arising from the dynamic coupling between the local and global degrees of

[4]The Lagrangian equations of motion are derived from the Newton's second law, known as the law of motion, which states that the force which acts on a particle and causes its motion is equal to the rate of change of momentum of the particle [89].

freedom. $\mathbf{f}_q$ are the generalized external forces associated with the components of $\mathbf{q}$, and they are computed using the formula

$$\mathbf{f}_q = \int \mathbf{L}^\top \mathbf{f}\, d\mathrm{u}, \tag{3.25}$$

where $\mathbf{f}$ is the 3-D force distribution applied to the model, and $\mathbf{L}$ is the model Jacobian matrix derived in (3.21). $\mathbf{f}_q$ can be decomposed into $(\mathbf{f}_c, \mathbf{f}_\theta, \mathbf{f}_s)$ where

$$\mathbf{f}_c = \int \mathbf{f}\, d\mathrm{u}; \tag{3.26}$$

$$\mathbf{f}_\theta = \int \mathbf{B}^\top \mathbf{f}\, d\mathrm{u}; \tag{3.27}$$

$$\mathbf{f}_s = \int (\mathbf{RJ})^\top \mathbf{f}\, d\mathrm{u}. \tag{3.28}$$

As shown in [60], for the applications to vision problems, the equations of motion in (3.24) can be simplified while preserving useful dynamics. By setting the mass density to zero, we obtain the following equations which yield a model that has no inertia and comes to rest as soon as all the applied forces equilibrate or vanish:

$$\mathbf{D}\dot{\mathbf{q}} + \mathbf{K}\mathbf{q} = \mathbf{f}_q. \tag{3.29}$$

In Chapter 7, we will simplify the above equations of motion even further for our application to cardiac motion estimation, and develop the relevant algorithms to compute the forces $\mathbf{f}$ from the medical image data.

Chapter 4

MRI-SPAMM

> "In 1932 Hamilton and Rompf sutured metal markers to the surface of the ventricles of dogs and observed their movements fluoroscopically. Rushmer and collaborators also sutured radiopaque objects to the heart and subsequently cineradiographic studies permitted detailed analyses of the motion of individual portions of the heart..." ([45]: p. 448)

4.1 Cardiac Motion Data Extraction

Characterization of heart wall motion on a regional level is required to understand cardiac mechanics and the processes signifying a disease. In order to accurately measure heart wall motion, a number of material points must be located and tracked. Methods of providing intra-myocardial markers in the past have included:

1. the implantation of radiopaque markers [45, 21, 59, 3], lead beads [104] or ultrasonic crystals [84, 103],
2. use of naturally occurring landmarks [53, 26, 107, 111], and
3. magnetic resonance (MR) tagging [116, 6, 65, 8, 32, 34].

Although the implantation methods [45, 84, 21, 59, 104, 103, 3] are widely used and provide the most accurate localization, the invasive nature of the procedures does not allow

a sufficient number of markers to be implanted for an adequate reconstruction of the LV geometry. Moreover, it poses potential problems of local myocardium property alteration due to the introduction of foreign objects. On the other hand, the methods which utilize naturally occurring landmarks, like bifurcations of coronary arteries [53, 26, 107, 111], do not require surgery and can potentially provide many markers. However, intra-coronary injection of contrast medium is usually required to highlight the blood vessels in acquired images. Moreover, when the blood supply is severely obstructed due to arterial occlusion, the tracing of the feature points around the region can be very difficult to achieve [53].

MR tagging has its advantages over the aforementioned approaches because a large number of material points may be marked and tracked during systole in a non-invasive manner. By locally perturbing the magnetization in tissue, one can create spatially encoded patterns such as star-bursts (e.g., [116, 65, 8, 32]) or grids (e.g., [6, 109, 34]). Those patterns or magnetization tags are seen as dark regions in subsequent images (within a certain relaxation time T_1). As magnetization moves with tissue, the magnetization tags will move in the corresponding images, directly reflecting the motion of the underlying tissue, allowing us to follow the motion patterns within otherwise featureless structures such as heart wall. One drawback of current MR tagging technique is that the tracking is possible only during systole or diastole at one time (i.e., not for a complete heart cycle), due to decay of the magnetization signal over time.[1]

Recently, curvature-based point correspondence recovery techniques have been proposed by researchers as an alternative to the above methods. The method by Goldgof *et al.* [64, 50] is based on the computation of the Gaussian curvature of a model that deforms based on the assumption of conformal motion. The method by Amini and Duncan [1, 90] utilizes the potential energy of their bending and stretching model to estimate the curvature. Shi *et al.* [91] combined curvature extraction with Phase Velocity MRI, in an attempt to assess the transmural myocardial deformation in 2-D. Friboulet *et al.* [35] demonstrated the stability of the Gaussian curvature computation in an experiment where the Gaussian curvature was computed through an iterative relaxation scheme from voxel-based surface rendering of CT left-ventricle volumetric data over a cardiac cycle. The derivation of point

[1] The weakening of the magnetization signal over time can be observed in Fig. 4.1 as well.

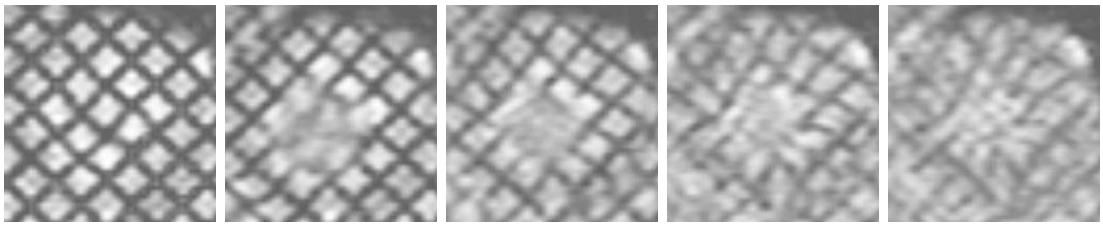

end diastole early systole mid systole end systole

Figure 4.1: MRI-SPAMM images of a mid left ventricle during systole

correspondences based on curvature has promising potential, in the sense that it can be widely used with data sets from many different medical imaging modalities, and it can provide point correspondence over an entire heart cycle.

4.2 Data Based on MRI-SPAMM

We propose to use a set of data from Magnetic Resonance Imaging with Spatial Modulation of Magnetization (SPAMM) [6], an MR tagging method, as an input to the proposed model for LV wall motion studies. The advantages of the SPAMM technique over the others are that a number of material points can be marked in a very short time with a simple procedure, and that they can be tracked during systole in a non-invasive setting, providing temporal correspondence of the material points. SPAMM technique has been previously used to demonstrate regional motion patterns during systole [7, 86, 115], and the methods for estimating material deformation have been validated using deformable phantoms [110]. Fig. 4.1 [courtesy of Dr. Leon Axel at the Radiology Department in the University of Pennsylvania] shows MRI-SPAMM images of an LV from end-diastole to end-systole. We can easily observe that these images reveal the underlying motion of the myocardium.

4.2.1 Terminology (III)

The SPAMM data collection technique is based on the application prior to imaging of a saturation pulse sequence where the amplitude of the magnetization varies spatially, in a sinusoidal-like fashion. This saturation pulse sequence forms the **tagging planes**. At the minima of this sinusoidal-like variation of the magnetization, dark stripes appear in

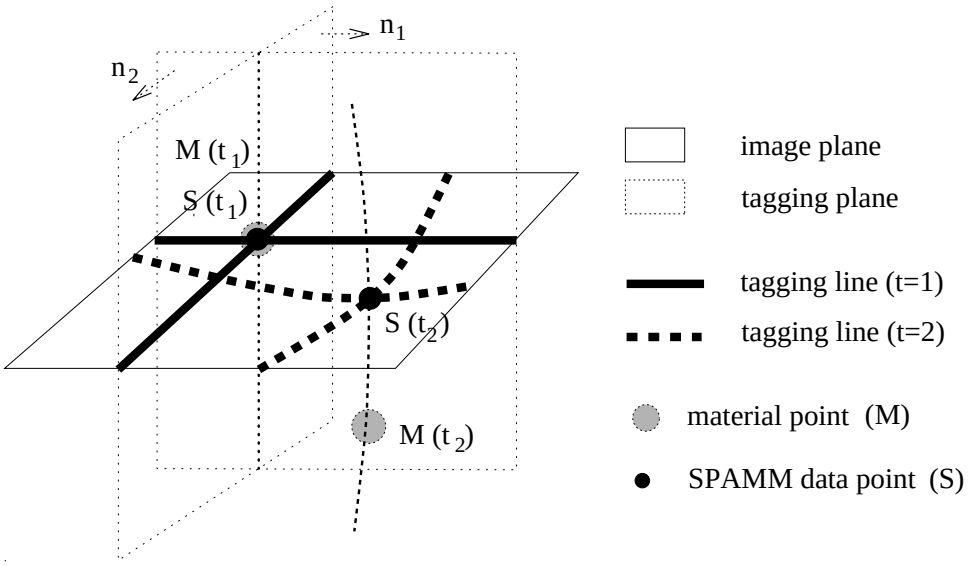

Figure 4.2: Tagging planes and image planes

the **image plane** which intersects the tagging planes. Note that the tagging planes are orthogonal to the image plane as shown in Fig. 4.2. Those dark stripes on the image plane are referred to as **tagging lines**. If we continue to image the tissue after the saturation pulse sequence is applied, we can see those tagging lines move, allowing us to track the motion of the underlying tissue. In order to track points instead of lines, another set of saturation pulse sequences is applied to form a set of tagging planes orthogonal to the previous set of tagging planes (n_1 and n_2 in Fig. 4.2). As a result, the grids appear in the image plane. The SPAMM data points are defined by the intersections of the respective tagging lines.

- **SPAMM data points :** intersections of the two orthogonal tagging lines (dark stripes) on an image plane. $\mathbf{S}(t)$ denotes the location of a SPAMM data point at time t.

- **material points :** specific points of the actual myocardium being imaged. Sometimes we use the term to refer to the corresponding points on the heart model. $\mathbf{M}(t)$ denotes the location of a material point at time t.

4.2.2 Time-Varying 2-D Data

Given that every image plane is spatially fixed, while a heart being imaged moves, the *through-plane* motion [86, 34] cannot be captured by the SPAMM data points on the image plane. Fig. 4.2 shows the location of a SPAMM data point $\mathbf{S}$ at two different times t_1 and t_2. Initially, $\mathbf{S}(t_1)$ coincides with a material point $\mathbf{M}(t_1)$. However, the motion of the SPAMM data point between these two time-instances corresponds to the components on the image plane of the motion of the material point $\mathbf{M}$, which lies somewhere along the line where the tagging planes intersect at time t_2. A possible position of the material point $\mathbf{M}$ at t_2 is marked in Fig. 4.2.

Therefore, we can only obtain *in-plane* motion from SPAMM images acquired over time. In order to assess the 3-D motion of material points of the LV from the set of such 2-D time-varying data, we need to combine, though a model-based approach, two sets of data obtained from mutually orthogonal image planes (see Figs. 10.1 and 10.2).

4.2.3 SPAMM Data Point Extraction

As described above, each SPAMM data point is defined as the intersection of two tagging lines. Young *et al.* [113] developed a method for extracting the intersection points of tagged lines. The method can be summarized as follows. For each image sequence, the tag stripes within the heart muscle are tracked semi-automatically using a 2-D active contour model [52]. In this procedure, each stripe is discretized into equally spaced points and is modeled as a thin, flexible beam with a small inherent resistance to stretching and bending. Stripes are connected at the intersection points and the entire mesh deforms to track the corresponding intensity values in the image. Fig. 4.3 [courtesy of Dr. Alistair Young at the University of Auckland in Auckland, New Zealand] shows an instance of tracking the tagging grid. Bilinear interpolation of image intensity between pixels enables sub-pixel resolution in stripe tracking. Only those points between the inner and outer boundaries were influenced by the image, and the remaining inactive points of the grid were maintained to provide a weak continuity for the structure and allowed points to move onto/off the image plane. Those active points are marked with a square and a dot in Fig. 4.3. For each time frame, the 2-D locations of the intersection points where the stripes are connected (i.e.,

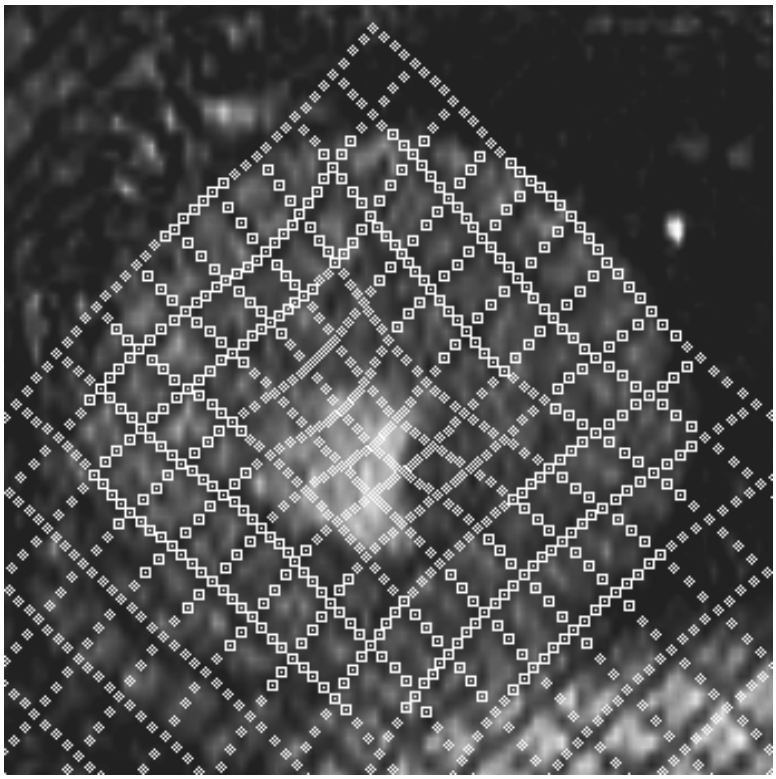

Figure 4.3: Tracking SPAMM tag stripes

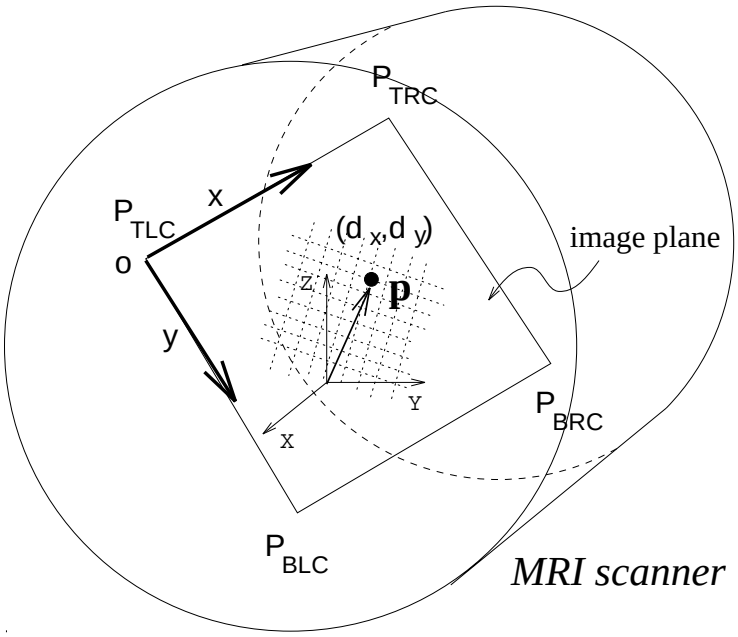

Figure 4.4: 3-D location of a data point on an image plane with respect to the scanner

SPAMM data points) are saved for further motion analyses. This semi-automatic tracking algorithm is incorporated into a software package SPAMMVU [5, 114], which is developed at the Radiology Department of the University of Pennsylvania.

4.3 Image Space to Object Space

During the SPAMM acquisition process, the spatial location of each image plane is evaluated based on the acquired spatial locations of the corners of each image plane so that we can convert the 2-D coordinates of each data point in image space into 3-D data points in object space as follows:

Given 4 corners of the image plane $\mathsf{P}_{\mathsf{TLC}}$, $\mathsf{P}_{\mathsf{TRC}}$, $\mathsf{P}_{\mathsf{BLC}}$ and $\mathsf{P}_{\mathsf{BRC}}$ in mm, we define x, y and $\mathbf{o}$ as follows.

$$\mathsf{x} = \frac{(\mathsf{P}_{\mathsf{TRC}} - \mathsf{P}_{\mathsf{TLC}})}{\mathrm{PSIZE}}; \tag{4.1}$$

$$\mathsf{y} = \frac{(\mathsf{P}_{\mathsf{BLC}} - \mathsf{P}_{\mathsf{TLC}})}{\mathrm{PSIZE}}; \tag{4.2}$$

$$\mathsf{o} = \frac{\mathsf{P}_{\mathsf{TLC}}}{\mathrm{PSIZE}}, \tag{4.3}$$

where PSIZE is the pixel size of the image. Then the 2-D points $\mathbf{d} = (d_x, d_y)$ in image

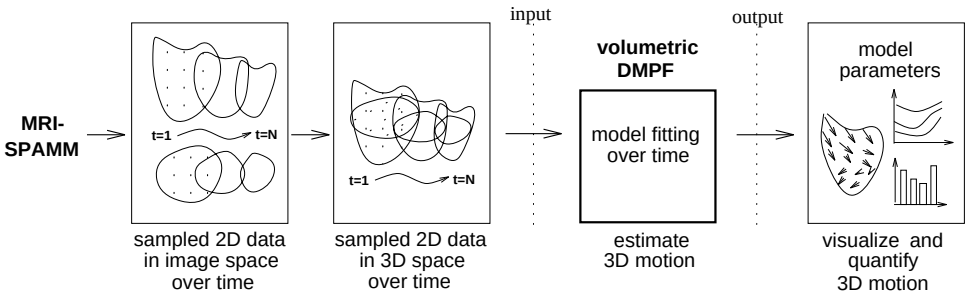

Figure 4.5: Input and output of the proposed method

plane coordinates can be expressed as 3-D points $\mathbf{p}$ with respect to the center of the MRI scanner where the image data are obtained.

$$\mathbf{p} = (\mathsf{o} + (\frac{d_x}{\mathrm{XDIM}}) * \mathsf{x} + (\frac{d_y}{\mathrm{YDIM}}) * \mathsf{y}) \times \mathrm{PSIZE} \tag{4.4}$$

where XDIM and YDIM are the dimensions of the image. Since the 3-D coordinates of the data points are expressed in mm, we may obtain measurements like length or volume in physical dimensions.

4.4 Data Flow

These 3-D data points will be used as an input to the proposed apparatus for the left ventricular wall motion studies as shown in Fig. 4.5. In addition to the SPAMM data points, boundary data points from the inner and outer LV walls are also extracted using active contour models and manual initialization, and converted into 3-D data points using the same formula given in (4.4). To summarize the preparation steps:

1. acquire MRI-SPAMM images

2. extract SPAMM data points and boundary data points from the images (2-D data points)

3. convert the 2-D data in image space into 3-D data based on the locations of the image plane with respect to the center of the scanner.

For a close-to-real time analysis of the LV motion, it would be desirable if we can minimize the preparation steps, and automate the process as much as possible[2]. However, the fully automatic extraction of both the SPAMM and the boundary data is beyond the scope of the present thesis. This thesis develops a systematic method in retrieving the 3-D motion based on the time-varying 2-D data sets. Part II of the thesis discusses the volumetric DMPF, the main block in Fig. 4.5, in full detail. The output of the main block is the *parameter functions* which abstract the motion of the LV. Part III illustrates the experimental results as well as some visualization techniques.

[2] An alternative method is to use image potential information directly without extracting data points. It is left as future work.

Part II

Volumetric Deformable Models with Parameter Functions

Part Overview

The second part of the thesis develops a new class of physics-based volumetric **d**eformable **m**odels whose global **p**arameters are **f**unctions (DMPF) which allows the definition of new parameterized primitives and parameterized global deformations. While these new shape primitives can be used in many applications, the technique for shape and motion estimation of the left ventricle (LV) of a heart is demonstrated.

We first review, in Chapter 5, related LV modeling work by other researchers to understand what the main limitations of existing models are, and show how we overcome the limitations in our new framework DMPF. Chapter 6 describes the geometry of DMPF for LV wall motion studies and Chapter 7 develops the adapted physics-based framework applied to MRI-SPAMM data.

Through the proposed technique we can estimate the deformation of an LV during systole in terms of a few global *parameter functions* [76]. The complex motion of the heart is thus characterized by the same small number of parameters, which vary from region to region. We can, therefore, capture the shape and motion of the LV walls (endocardium, epicardium and anywhere in between) based on the parameters of the DMPF. Furthermore, these parameters are intuitive and can be readily used by a physician without further complex processing. In Chapter 8, we study the parameter functions of the proposed LV model in detail.

Chapter 5

Related Work on Heart Modeling

> "Very little is currently known about the change in constitutive law parameters in the diseased heart. Since a major reason for developing continuum models of the heart is the potential clinical application, the problems of extracting quantitative information from clinically available diagnostic tools such as X-ray, NMR or other imaging techniques is another very important and challenging task. Moreover, the enormous potential of theses highly sophisticated (and expensive devices will only be realized by their use in conjunction with continuum models." ([48]: p. 159)

The common method in Medical Imaging for visualizing an organ or a structure is to perform either surface or volume renderings of segmented image data represented as voxels [46, 85]. It is not surprising that it is also the case in cardiac imaging. The most common practice for viewing the motion of a heart in its cycle is to display a series of 2-D slices in a cine mode. Surface and volume rendering techniques have also been utilized in an attempt to view the 3-D motion of a pumping heart. Although the renderings of voxel-based image data throughout the cardiac cycle would give a good qualitative visualization of the LV, it does not provide any means for a quantitative analysis of the motion. In order to quantify the complicated motion of a left ventricle (LV) and to interpret its measured deformation, it is necessary to represent the LV by constructing some kind of geometric model.

Simple analytical shapes like spheres, ellipsoids or cylinders are often used to approximate the shape and motion of an LV. For example, Beyar and Sideman [15] constructed a mechanical model where the LV is viewed as a nested-shell spheroidal geometry to explain the effect of twisting motion; Arts *et al.* [4] used a thick-walled cylinder composed of eight concentric cylinder shells to describe LV deformation; Kim *et al.* [53] used a thick-walled ellipsoidal model for computation of the wall stress, and a truncated ellipsoidal model for simulation of regional stress; Azhari *et al.* [8] used a hollow conical shell (with a constant shear modulus) to characterize transmural twist motion; and Arts *et al.* [2, 3] developed a kinematic model combining the modes from spherical, prolate ellipsoidal and cylindrical models.

However, the shape of an LV is neither spherical nor cylindrical. Even a prolate ellipsoid is a gross simplification of the shape of an LV. Therefore, as Guccione and McCulloch [44] pointed out, the analyses made by these models are based on simplifying assumptions about the material behavior of the heart muscle and the governing equations of motion. With deformable 3-D models, one can improve the shape representing an LV more closely at any phase during its cycle. But it is important to keep in mind that our purpose of constructing a heart model is not to create only a visually appealing model but a clinically useful one which allows us to perform quantitative motion analyses.

5.1 Surface Models

Recently, 3-D *surface* models and associated computer vision or graphics techniques have been developed to capture the shape and motion of the inner or outer walls of an LV from medical image data. These models are constructed with finite element meshes derived from polyhedron surface reconstruction from a stack of cross sections [26, 36], physics-based elastic models [27, 58, 47, 81, 67], bending and stretching models [1, 90], or augmenting local details to an axisymmetrical geometric model [11, 64]. The techniques are briefly described below:

- McInerney and Terzopoulos [58] developed the 3-D deformable balloon model [27] composed of triangular C^1 finite elements based on the framework developed by

Metaxas and Terzopoulos [60]. They applied it to CT data consisting of 16 volume images of a canine heart during one cardiac cycle. The reconstruction of the LV shape at each time frame looks realistic, but it seems that the motion tracking is possible only from observation of the fitted models. No explicit motion parameters are provided from the model.

- Pentland *et al.* [79, 80, 87] developed a model, based on the modal analysis, which can decompose the motion into deformable modes, and applied the technique to recovering the non-rigid motion of a heart from 2-D X-ray images. Their LV model was defined using 30 deformable modes. Following their work, Nastar and Ayache [67] performed spectrum analysis in modal space for various LVs from Nuclear Medicine to classify non-rigid motion from 51 modes. Although the technique might provide a means for discriminating abnormal hearts from normal hearts based on the modal parameter spectrums, those parameters do not have any anatomical significance and localization properties (because they are based on vibration of a mesh model); therefore, the modal analysis technique does not provide an intuitive parameterization for a better understanding of the heart wall motion.

- Amini and Duncan [1] developed bending and stretching thin-plate models which allow point matching based on bending energy for motion tracking of the left ventricle wall, and Shi *et al.* [90] presented results of the shape-based technique applied to MRI data showing motion trajectories of selected endocardial points.

- Friboulet *et al.* [36] constructed a polyhedral model from the set of cross sections in slices of a volume of MRI data. The motion of the model was approximated by an affine transformation with translation, rotation, and dilation motion parameters.

- Huang and Goldgof [47] developed a spring-mass, adaptive-size mesh model and applied it to CT data of a canine heart during one cardiac cycle to track the node correspondence in a cardiac cycle. No explicit motion parameters are provided except local displacement trajectories of the nodes.

- Bardinet *et al.* [11] refined the shape of a model applying the technique of free-form deformations [88] to underlying global shape defined by superquadrics [12]. The

fitting results are very impressive. However, since it is hard to correlate the control nodes with anatomical parts of the LV, the technique is no more clinically useful than simple geometric models.

The main limitation of these techniques is that they do not provide intuitive motion parameters to describe the rigid and non-rigid motion of the LV. Most of the techniques [27, 26, 1, 64, 58, 47, 90] provide only local displacement vectors so that either they require non-trivial post-processing to be useful to a physician or they are good only for qualitative visualization. On the other hand, models like [36, 11] are formulated in terms of very few parameters that can offer only a gross approximation to the motion of the LV. There are some attempts to characterize the motion with a fair number of parameters [80, 67], but their parameterizations cannot provide anatomical or intuitive meanings for a better understanding of LV motion. Moreover, most techniques [1, 64, 58, 47, 36, 11, 80, 67] ignore the twisting or wringing motion of the LV known to occur during systole.

To overcome the problems of the above techniques in terms of accurately estimating the LV surface shape and motion and in order to extract parameters that can be easily interpreted by physicians, we previously developed a new class of deformable primitives whose global parameters are functions (DMPF) [76, 77]. This new DMPF can capture and quantify the axial twisting, bending, and contraction of the LV surface. The input to these models were data points sampled from the mid-wall of the 3-D finite element model of Young and Axel [109] (discussed in the following section), which estimates the LV shape and motion from MRI-SPAMM[1].

5.2 Volumetric Models

The LV motion cannot be captured entirely with surface models alone because the endocardial and epicardial motions are sufficiently different. To be able to capture the LV shape and motion throughout the volume, we need a *volumetric* model. Recently, techniques for analyzing the motion from a volumetric representation of the LV have also been developed by coupling epicardial and endocardial surfaces [54, 109, 65, 71, 32].

[1] The experimental results from the surface DMPF are discussed in Chapter 9.

Unlike the techniques used for surface models that are discussed in the previous section, the techniques for recovering 3-D LV motion using volumetric models are motivated to overcome the limitation of current medical imaging modalities where true time-varying 3-D data points useful for motion studies cannot be provided explicitly due to "through-plane" motion. The translation of the deforming heart *through* the fixed image *planes* puts a different cross section of myocardium into the image plane at each time point. Therefore the imaging techniques provide only time-varying 2-D data at best.

Volumetric models used for LV wall motion analysis are mostly reconstructed from tagged MR data which provides temporal correspondences of individual data points. The models constructed from other medical image data provide only global measures like ejection-fraction and wall-thickening (e.g., [54]). The following describes how other researchers tracked the 3-D motion with volumetric model-based approach:

- Young and Axel [109, 108] developed a finite element based method for reconstructing the three-dimensional motion and deformation from MRI-SPAMM images in two orthogonal views during systole. The data points are collected from 5 parallel short-axis image planes along the *long axis*[2] of an LV, and 5 parallel evenly spaced long-axis image planes.

  Initially, the finite element models are created by fitting to contours defining inner and outer walls of the LV at each time frame from end-diastole (t=1) to end-systole one by one. Since the SPAMM data points at $t > 1$ provide displacement information (because the projections of their initial positions on the image planes are known), those models fitted to data at $t > 1$ are deformed to t=1 state based on the displacement information provided by SPAMM data recovering the through-plane motion. The deformation was found with a linear least squares fit. This results in a number of models representing the LV at t=1. To compute the strain from end-diastole to end-systole, the initial model at t=1 is now deformed to all states at $t > 1$ using the through-plane motion estimated in the previous stage together with in-plane motion. The model has 16 bicubic Hermite finite elements.

[2]Long axis of an LV is its base-apex line.

- To solve the through-plane motion problem, Moore *et al.* [65] developed a 3-D material point-tracking algorithm from biplanar tagged MR images. Data were taken from 5 evenly spaced short-axis image planes perpendicular to the long axis of an LV, and 6 radial planes intersecting with the short-axis image stack along the long axis of the LV. Data used in the tracking algorithm are the endocardial and epicardial endpoints of the tag segments (or tag points). Their algorithm works as follows:

  First, locate (x, y, z) coordinates from a short-axis image tag point. Second, use appropriate long-axis tag points to find z motion in region of heart defined by (x, y) by locating the tag points on long axis tag surface and fitting their z coordinate with a smooth periodic cubic spline as a function of the angle about their common centroid (x, y). Then calculate the angle of the previous (x, y) position of the material point. The angle is used to find its revised z position from the spline. And interpolate x and y with those on the short-axis image planes at the level of the new z value of the material point. Repeat the second step procedure until the changed in z position is negligible. In their model, 48 volume elements were defined for strain analysis.

- O'Dell *et al.* [71] proposed a method that uses parallel planar tags to image the 3-D displacement field of the myocardium. The data is composed of two sets of short-axis images along the long axis of an LV, and one consists of long-axis images taken radially. In oder to compute strain, dense displacement measurements were achieved by Denney and Prince [32] who developed a multidimensional stochastic model under Fisher estimate frame work to reconstruct the displacement field on a regular 3-D lattice.

Finite element modeling [49, 40, 48, 44, 43, 54, 109, 65] is a typical choice for volumetric motion analysis since it provides strain analysis throughout the ventricular wall. Most finite element models are, unfortunately, prone to an incorrect analysis due to the inappropriate assumption of homogeneous material properties of myocardium. Recently, Guccione *et al.* [43] developed the finite element model for continuum analysis by incorporating muscle fiber orientation.

Although finite element modeling promises extensive strain and stress analysis [37], its

representation does not directly lend itself to an understanding of the underlying kinematics in an intuitive way. The parameters of the model are nodal displacements, resulting in a relatively large number of parameters, the physical interpretation of which can be difficult. The three-dimensional strain tensor, for example, has three normal components and three shear components, each of which may vary with position in the wall. In order to understand the complex relationship between these components and other motion parameters, it is desirable to characterize the motion in terms of a few physical parameters that offer sufficient accuracy. In the rest of the thesis, we will demonstrate how it is achieved by the proposed volumetric DMPF.

5.3 Summary

In this chapter, we reviewed various models for a left ventricle (LV) utilized and developed by other researchers to study the complex motion of a heart. The results of motion analyses from traditional approaches are grossly simplified because the shape of an LV was approximated using simple analytical shapes like spheres, ellipsoids or cylinders. Recently, 3-D models and associated computer vision or graphics techniques have been developed to capture the shape and motion of the inner or outer walls of an LV from medical image data. However, the main limitation of these techniques is that they do not provide intuitive motion parameters to describe the rigid and non-rigid motion of the LV. Moreover, most of them furnish only a surface model. Finite element models are most common for volumetric 3-D LV motion studies since they provide a good local strain analysis. However, the parameters of the finite element model are nodal displacements, resulting in a relatively large number of parameters which require non-trivial post-processing, and therefore the physical interpretation of which can be difficult.

Chapter 6

Model Geometry

In Section 3.3, we have briefly introduced the geometry of the new class of deformable models whose global parameters are functions (DMPF). In this chapter, we extend the definition for an application to modeling the left ventricle (LV) of a heart.

Fig. 6.1 demonstrates how the non-uniform shape detail can be captured by utilizing the global parameter functions without any local parameters. Fig. 6.1(a) is an example of the volumetric model with constant parameters, and Fig. 6.1(b) are two examples of a volumetric model whose parameters are functions.

(a) with constant parameters (b) with parameter functions

Figure 6.1: Volumetric deformable models

6.1 Reference Shape

The technique for creating primitives with parameter functions can be applied to any parametric primitive, *by replacing its constant parameters with differentiable parameter*

functions. For example, to create a volumetric model for the LV, a generalized primitive $\mathbf{e} = (e_1, e_2, e_3)^\top$ is defined as follows:

$$\mathbf{e} = \mathbf{e}(\mathbf{u}; a_0, a_1(\mathbf{u}), a_2(\mathbf{u}), a_3(\mathbf{u})) \tag{6.1}$$

$$= a_0 w \begin{pmatrix} a_1(\mathbf{u}) \ \cos u \ \cos v \\ a_2(\mathbf{u}) \ \cos u \ \sin v \\ a_3(\mathbf{u}) \ \sin u \end{pmatrix}, \tag{6.2}$$

where $\mathbf{u}$=(u, v, w) are the material coordinates with $-\pi/2 \leq u \leq \pi/4$, $-\pi \leq v < \pi$, $w > 0$; $a_0 > 0$, and $0 \leq a_1(\mathbf{u}), a_2(\mathbf{u}), a_3(\mathbf{u}) \leq 1$. This primitive is created from an ellipsoid primitive $\mathbf{e}_e$

$$\mathbf{e}_e = a_0 w \begin{pmatrix} a_1 \ \cos u \ \cos v \\ a_2 \ \cos u \ \sin v \\ a_3 \ \sin u \end{pmatrix}, \tag{6.3}$$

where $-\pi/2 \leq u \leq \pi/2$, $-\pi \leq v < \pi$, $w > 0$, $a_0 > 0$, and $0 \leq a_1, a_2, a_3 \leq 1$, by replacing its constant parameters with parameter functions. a_0 is a scale parameter and a_1, a_2 and a_3 are the aspect ratio parameters along the x-, y- and z-axis, respectively. Note that the ranges of the u and v parameters for the generalized primitive (6.2) are restricted to a subset of those for an ellipsoid primitive defined by (6.3), in order to construct an open[1] parameterized primitive.

6.2 Deformation

The shape represented by $\mathbf{e}$ is subject to the *deformation* $\mathbf{T}$ which depends on the deformation parameter functions. While we can apply many deformation operations, we found that the parameterized twisting and axis offset deformations are suitable for the LV motion capturing.

[1] not closed, but more like a cup

6.2.1 Twisting

Given the above defined primitive $\mathbf{e} = (e_1, e_2, e_3)^\top$, the parameterized twisting is defined along the model axis z, which results in the global shape $\mathbf{s}_t = (s_{t_1}, s_{t_2}, s_{t_3})^\top$:

$$\begin{aligned} \mathbf{s}_t &= \mathbf{T}_t(\mathbf{e}; \tau(\mathbf{u})) && (6.4) \\ &= \begin{pmatrix} e_1 \cos(\tau(\mathbf{u})) - e_2 \sin(\tau(\mathbf{u})) \\ e_1 \sin(\tau(\mathbf{u})) + e_2 \cos(\tau(\mathbf{u})) \\ e_3 \end{pmatrix}, && (6.5) \end{aligned}$$

where $\tau(\mathbf{u})$ is the twisting parameter function along the axis z.

6.2.2 Axis Offset Deformation

Through the use of appropriate parameterization the axes of our new deformable primitives can be curved. This is a major generalization compared to parameterized primitives such as superquadrics, cylinders and cubes, commonly used in the vision literature. Furthermore, generalized cylinders [16, 56, 68], even though they allow shapes with curved axes, do not offer shape representation in terms of a few parameters.

The offset deformations are defined to allow the axis to be non-straight in the x and y directions. In this way the LV shape can be recovered more accurately. The resulting reference shape $\mathbf{s} = \mathbf{s}_o = (s_{o_1}, s_{o_2}, s_{o_3})^\top$ is expressed as follows:

$$\begin{aligned} \mathbf{s} &= \mathbf{T}_o(\mathbf{T}_t(\mathbf{e}; \tau(\mathbf{u})); e_{1_o}(\mathbf{u}), e_{2_o}(\mathbf{u})) && (6.6) \\ &= \mathbf{T}_o(\mathbf{s}_t; e_{1_o}(\mathbf{u}), e_{2_o}(\mathbf{u})) && (6.7) \\ &= \begin{pmatrix} s_{t_1} + e_{1_o}(\mathbf{u}) \\ s_{t_2} + e_{2_o}(\mathbf{u}) \\ s_{t_3} \end{pmatrix}, && (6.8) \end{aligned}$$

where $e_{1_o}(\mathbf{u})$ and $e_{2_o}(\mathbf{u})$ are axis-offset parameter functions in the x and y directions, respectively.

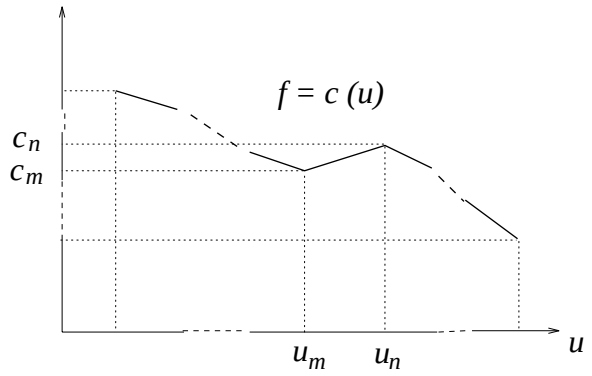

Figure 6.2: Piecewise linear function

6.3 Model Parameters

By putting all deformation parameters together, the vector $\mathbf{q}_s$, which refers to the degrees of freedom of the model with respect to the deformation parameters, is created for the LV model as follows:

$$\mathbf{q}_s = (a_0, a_1(\mathbf{u}), a_2(\mathbf{u}), a_3(\mathbf{u}), \tau(\mathbf{u}), e_{1_o}(\mathbf{u}), e_{2_o}(\mathbf{u}))^\top. \tag{6.9}$$

Note that the scaling parameter a_0 remains as a constant parameter. Fig. 6.3 demonstrates the effect of changing the value of each parameter function at a particular point u_i along u. $+\Delta$ and $-\Delta$ denote an increase or a decrease, respectively, in the value of the relevant parameter function at u_i. The dotted lines denote the initial shape of the deformable model at u_i, while the solid line denotes its shape after the value of the relevant parameter function is changed.

For our applications we assume that the parameter functions are piecewise linear along $\mathbf{u}$, so we do not impose any shape continuity constraints on the LV shape and motion. In other words, the model will deform based on the motion dictated by the dataset and not on the imposition of constraints such as artificial elastic properties. Fig. 6.2 shows an example of a piecewise linear function of u, where it has the following form:

$$f = \frac{c_n - c_m}{u_n - u_m}(u - u_n) + c_n; \qquad u_m < u \leq u_n. \tag{6.10}$$

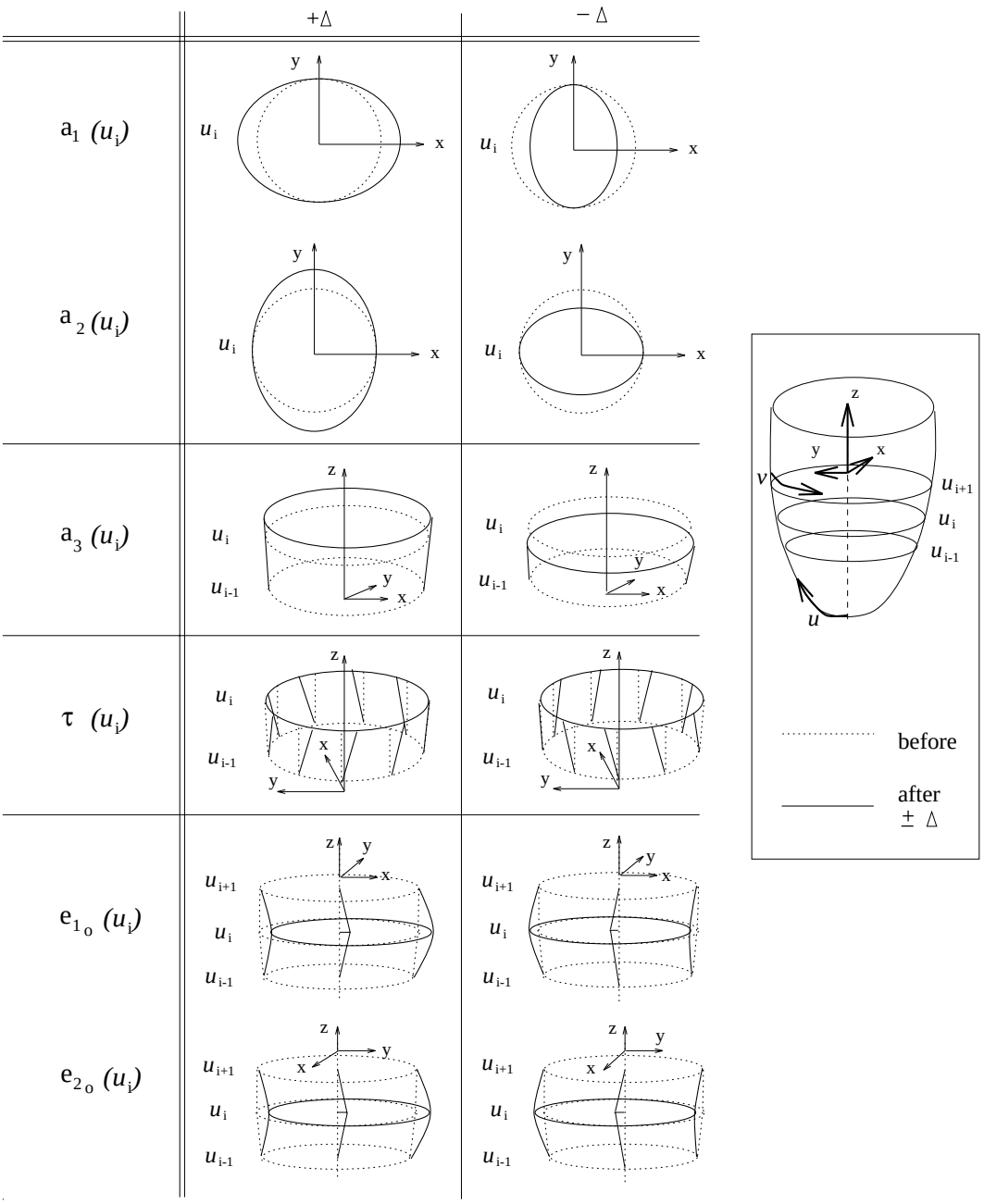

Figure 6.3: Effect of changing the value of each parameter function

6.4 Jacobians

The Jacobian of the shape primitive $\mathbf{s}$ can be computed in a modular way using a chain rule as given in equations (3.9)–(3.11), where $\mathbf{s}_1 = \mathbf{s}_t$ and $\mathbf{s}_2 = \mathbf{s}_n = \mathbf{s}_o$. From the equations (6.2), (6.5) and (6.8), we may compute the following directly.

$$\mathbf{J}_0 = \mathbf{J}_e = \frac{\partial \mathbf{e}}{\partial \mathbf{q}_\alpha} = \begin{bmatrix} \frac{\partial e_1}{\partial a_0} & \frac{\partial e_1}{\partial a_1} & \frac{\partial e_1}{\partial a_2} & \frac{\partial e_1}{\partial a_3} \\ \frac{\partial e_2}{\partial a_0} & \frac{\partial e_2}{\partial a_1} & \frac{\partial e_2}{\partial a_2} & \frac{\partial e_2}{\partial a_3} \\ \frac{\partial e_3}{\partial a_0} & \frac{\partial e_3}{\partial a_1} & \frac{\partial e_3}{\partial a_2} & \frac{\partial e_3}{\partial a_3} \end{bmatrix} \tag{6.11}$$

$$\frac{\partial \mathbf{s}_1}{\partial \mathbf{s}_0} = \frac{\partial \mathbf{s}_t}{\partial \mathbf{e}} = \begin{bmatrix} \frac{\partial s_{t_1}}{\partial e_1} & \frac{\partial s_{t_1}}{\partial e_2} & \frac{\partial s_{t_1}}{\partial e_3} \\ \frac{\partial s_{t_2}}{\partial e_1} & \frac{\partial s_{t_2}}{\partial e_2} & \frac{\partial s_{t_2}}{\partial e_3} \\ \frac{\partial s_{t_3}}{\partial e_1} & \frac{\partial s_{t_3}}{\partial e_2} & \frac{\partial s_{t_3}}{\partial e_3} \end{bmatrix}; \quad \frac{\partial \mathbf{s}_t}{\partial \mathbf{q}_{T_t}} = \begin{bmatrix} \frac{\partial s_{t_1}}{\partial \tau} \\ \frac{\partial s_{t_2}}{\partial \tau} \\ \frac{\partial s_{t_3}}{\partial \tau} \end{bmatrix} \tag{6.12}$$

$$\frac{\partial \mathbf{s}_2}{\partial \mathbf{s}_1} = \frac{\partial \mathbf{s}_o}{\partial \mathbf{s}_t} = \begin{bmatrix} \frac{\partial s_{o_1}}{\partial s_{t_1}} & \frac{\partial s_{o_1}}{\partial s_{t_2}} & \frac{\partial s_{o_1}}{\partial s_{t_3}} \\ \frac{\partial s_{o_2}}{\partial s_{t_1}} & \frac{\partial s_{o_2}}{\partial s_{t_2}} & \frac{\partial s_{o_2}}{\partial s_{t_3}} \\ \frac{\partial s_{o_3}}{\partial s_{t_1}} & \frac{\partial s_{o_3}}{\partial s_{t_2}} & \frac{\partial s_{o_3}}{\partial s_{t_3}} \end{bmatrix}; \quad \frac{\partial \mathbf{s}_o}{\partial \mathbf{q}_{T_o}} = \begin{bmatrix} \frac{\partial s_{o_1}}{\partial e_{1_o}} & \frac{\partial s_{o_1}}{\partial e_{2_o}} \\ \frac{\partial s_{o_2}}{\partial e_{1_o}} & \frac{\partial s_{o_2}}{\partial e_{2_o}} \\ \frac{\partial s_{o_3}}{\partial e_{1_o}} & \frac{\partial s_{o_3}}{\partial e_{2_o}} \end{bmatrix} \tag{6.13}$$

$$\frac{\partial \mathbf{s}_t}{\partial \mathbf{q}_\alpha} = \frac{\partial \mathbf{s}_o}{\partial \mathbf{q}_\alpha} = \mathbf{0}. \tag{6.14}$$

Non-zero terms in (6.11)-(6.13) are:

$$\frac{\partial e_1}{\partial a_0} = w\ a_1(\mathbf{u}) \cos u \cos v \tag{6.15}$$

$$\frac{\partial e_1}{\partial a_1} = w\ a_0 \cos u \cos v \tag{6.16}$$

$$\frac{\partial e_2}{\partial a_0} = w\ a_2(\mathbf{u}) \cos u \sin v \tag{6.17}$$

$$\frac{\partial e_2}{\partial a_2} = w\ a_0 \cos u \sin v \tag{6.18}$$

$$\frac{\partial e_3}{\partial a_0} = w\ a_3(\mathbf{u}) \sin u \tag{6.19}$$

$$\frac{\partial e_3}{\partial a_3} = w\ a_0 \sin u \tag{6.20}$$

$$\frac{\partial s_{t_1}}{\partial e_1} = \cos \tau(\mathbf{u}) \tag{6.21}$$

$$\frac{\partial s_{t_1}}{\partial e_2} = -\sin \tau(\mathbf{u}) \tag{6.22}$$

$$\frac{\partial s_{t_2}}{\partial e_1} = \sin\tau(\mathbf{u}) \tag{6.23}$$

$$\frac{\partial s_{t_2}}{\partial e_2} = \cos\tau(\mathbf{u}) \tag{6.24}$$

$$\frac{\partial s_{t_3}}{\partial e_3} = 1 \tag{6.25}$$

$$\frac{\partial s_{t_1}}{\partial \tau} = -e_1 \sin\tau(\mathbf{u}) - e_2 \cos\tau(\mathbf{u}) \tag{6.26}$$

$$\frac{\partial s_{t_2}}{\partial \tau} = e_1 \cos\tau(\mathbf{u}) - e_2 \sin\tau(\mathbf{u}) \tag{6.27}$$

$$\frac{\partial s_{o_1}}{\partial s_{t_1}} = 1 \tag{6.28}$$

$$\frac{\partial s_{o_2}}{\partial s_{t_2}} = 1 \tag{6.29}$$

$$\frac{\partial s_{o_3}}{\partial s_{t_3}} = 1 \tag{6.30}$$

$$\frac{\partial s_{o_1}}{\partial e_{1_o}} = 1 \tag{6.31}$$

$$\frac{\partial s_{o_2}}{\partial e_{2_o}} = 1 \tag{6.32}$$

Then, we apply chain rule to compute, for example, $\frac{\partial \mathbf{s}_t}{\partial a_0}$ as follows:

$$\frac{\partial \mathbf{s}_t}{\partial a_0} = \frac{\partial \mathbf{s}_t}{\partial e_1} \times \frac{\partial e_1}{\partial a_0} + \frac{\partial \mathbf{s}_t}{\partial e_2} \times \frac{\partial e_2}{\partial a_0} + \frac{\partial \mathbf{s}_t}{\partial e_3} \times \frac{\partial e_3}{\partial a_0}. \tag{6.33}$$

6.5 Volumetric Model Assembly

In order to create the volumetric model, we first create volumetric meshes in the material coordinate space Ω where $u_{min} \leq u \leq u_{max}$, $-\pi \leq v \leq \pi$ and $0 < w_{min} \leq w \leq w_{max}$. The meshes are uniformly tessellated based on the dimensions (usize, vsize, wsize) which are specified by a user. u_{min} is set to $-\frac{\pi}{2} + \frac{(u_{max} - u_{min})}{\text{usize}}$ and u_{max} is set to $\frac{\pi}{4}$. Ω is "folded up" [31] in such a way that the node at $(u_i, -\pi, w_k)$ meets with the node at (u_i, π, w_k), where $1 < i \leq$ usize and $1 \leq k \leq$ wsize. Then wsize number of "south" poles are created at $u_{pole} = -\frac{\pi}{2}$ so that those nodes at (u_{min}, v_j, w_k), where $1 \leq j \leq$ vsize and $1 \leq k \leq$ wsize, are merged into the pole at w_k. This folding operation Π will produce an open ellipsoidal model as shown in Fig. 6.5. The rectangular face on w-iso-surface is also triangulated so that the model is discretized based on prismatic volume elements as shown in Fig. 6.5.

As defined in (3.3), the positions of nodes on the model $\mathbf{s}$ in model frame ϕ is given by

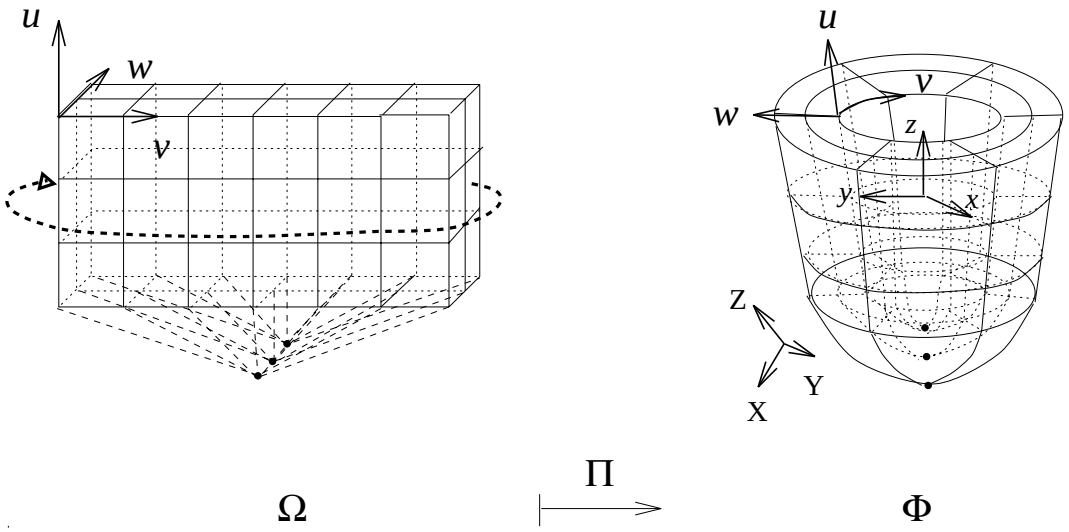

Figure 6.4: Volume parameterization

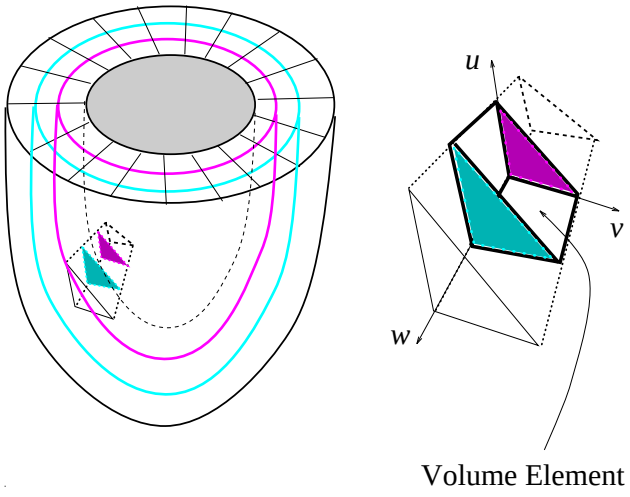

Figure 6.5: Discretization of the LV model based on volume elements.

$\mathbf{x}$ which is expressed with respect to the inertial frame Φ as follows:

$$\mathbf{x}(\mathbf{u},t) = \begin{bmatrix} x(u,v,w,t) \\ y(u,v,w,t) \\ z(u,v,w,t) \end{bmatrix}. \tag{6.34}$$

This representation reveals the dynamic behavior of the model. Each node is free to move in 3-D space within the shape constraints [105] – e.g., the inner layer of the model is always inside of the outer layer.

6.6 Summary

The primitives with parameter functions can be created by replacing its constant parameters with differentiable parameter functions. For the application to LV modeling, we have defined the volumetric primitive with parameter functions from a generalized ellipsoid, with a parameterized twisting and axis-offset deformations. The parameter functions are assumed to be piecewise linear functions. The model degrees of freedom vector $\mathbf{q}_s$ as a part of the generalized coordinates and the Jacobians of the shape primitive are derived. The dynamics of the model involving $\mathbf{q}_s$ will be discussed in the following chapter.

Chapter 7

Model Dynamics

7.1 Adaptation of the Framework

The proposed model is based on extensions to the framework developed by Metaxas and Terzopoulos [60, 63] which provides deformable models along with robust techniques for modeling and estimating the shape, material properties and motion of non-rigid objects. The modeling primitives are provided through a mathematical approach that allows the combination of global and local deformations. The salient shape features of natural parts (e.g., gross length and width, whether the model is bent, tapered, twisted, etc.) are represented by global deformation parameters, while shape details are captured by local deformation parameters. Their physics-based framework provides a systematic approach based on Lagrangian dynamics to converting the geometric parameters of the primitives to dynamic degrees of freedom [89]. We will be using and further developing the physics-based framework of Metaxas [60] in order to achieve a real time performance for the application to heart wall motion analysis.

As defined in the previous chapter, the new class of proposed deformable models is unique in the sense that the modeling primitives are defined with only *global* parameters that are capable of capturing *local* deformation.[1] Therefore, it allows not only compact

[1] See Fig. 6.1(c) which shows an example of the new family of volumetric deformable primitives with parameter functions, used in estimating the volumetric shape of the LV.

but also accurate representation and description of the shape and deformation. By incorporating the geometric definition of the models into the physics-based framework, we create dynamic models that deform due to forces exerted from MRI-SPAMM data points and conform to the given dataset.

7.2 Simplified Lagrange Equations

We have defined the Lagrangian equations of motion in Section 3.5, where we make the model dynamic in $\mathbf{q}$ by introducing mass, damping, and a deformation strain energy. The governing Lagrange equations of motion are second order differential equations given in (3.24). In applications to shape recovery problems, it makes sense to simplify the motion equations while preserving useful dynamics by setting the mass density to zero so that the resulting equations yield a model that has no inertia and comes to rest as soon as all the applied forces equilibrate. These equations, which are given in (3.29), have damping and stiffness matrices.

Given that the localization and tracking of SPAMM data points is relatively accurate, and in order to avoid undesired smoothness in the solution caused by the incorporation of incorrect elasticity in the model, we assume a zero stiffness matrix[2] so that there is no resistance to deformation. The resulting equation of motion is:

$$\mathbf{D}\dot{\mathbf{q}} = \mathbf{f}_q. \tag{7.1}$$

where $\mathbf{q}$ is the vector of the model's degrees of freedom, $\mathbf{D}$ is the damping matrix used as a stabilizing factor, and $\mathbf{f}_q$ are the associated generalized forces.

In most cases, $\mathbf{D}$ is diagonal and constant over time. Therefore, we can simply write the governing equations of motion for our system as:

$$\dot{\mathbf{q}} = \mathbf{f}_q. \tag{7.2}$$

[2]While we use the above defined deformations, finite elements are often used as an alternative, to model deformations. Possible errors from using finite elements to model the heart wall elasticity arise due to the incorrect computation of the material stiffness matrix when the elasticity of the myocardium which varies spatially is not known. Simplifying assumptions for the elasticity of the myocardium have been attempted. For example, in the work of Janz and Waldron [49], the myocardium was approximated with a homogeneous, isotropic and incompressible material, and in the work of Ghista and Hamid [40], the isoparametric elements are utilized.

For fast interactive response, a first-order Euler's method[3] is employed to integrate equation (7.2).

7.3 Model Force Computation

The generalized forces $\mathbf{f}_q$ are computed from the 3D force distribution, $\mathbf{f}$, applied to the model based on the equation (3.25). In computing the correct forces from the data the algorithm exploits the geometry of the motion of the SPAMM data points over time. Once these forces are computed, we use a Lagrangian dynamics formulation to estimate the model parameters.

As briefly introduced in Section 4.4, we utilize two kinds of data sets – SPAMM data points and boundary data points – extracted from MRI images. From these data, we compute the corresponding forces on the model depending on their type. Boundary data provide forces for the estimation of the LV shape, while SPAMM data points provide forces for the estimation of the volumetric motion of the LV. The following subsections describe the algorithms for extracting and distributing forces from the given data set. Note that the model is discretized based on prismatic volume elements as shown in Fig. 6.5 with its triangular faces at each layers[4] of the LV model[5].

7.3.1 Force Computation from Boundary Data

Boundary data simply constrain the shape of the inner and outer walls of the LV and provide no correspondence of points over time. There are two kinds of boundary data – inner boundary data for endocardium and outer boundary data for epicardium. Each set of boundary data exerts forces only to its corresponding layer of the model. The forces from each boundary data point $\mathbf{z}$ to the corresponding model wall (inner or outer) are

[3]The formula for the Euler's method is

$$y_{n+1} = y_n + h\ f'(x_n, y_n) \tag{7.3}$$

which advances a solution from x_n to $x_{n+1} = x_n + h$. Practical interpretation of the Euler's method is to add small increments to the functions corresponding to derivatives multiplied by a small step-size [83].

[4]The term **layer** refers to w-iso-surface of the model. For example the inner-most layer is the endocardium and the outer-most layer is the epicardium.

[5]The resolution of discretization of the volume of the myocardium depends on how dense the SPAMM data points are distributed throughout the volume.

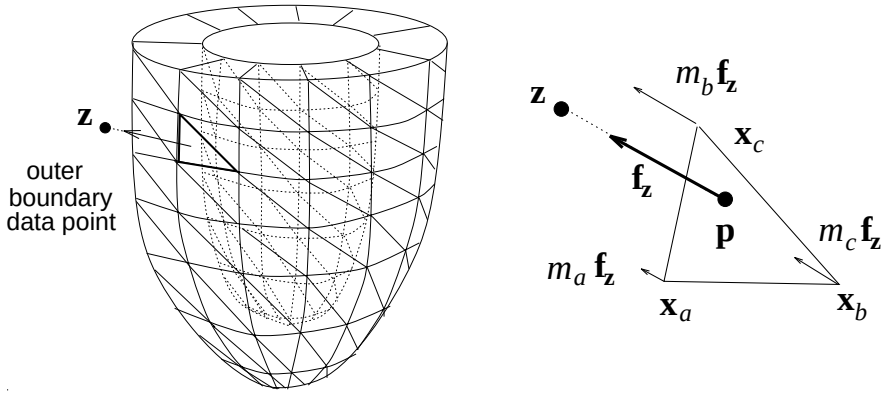

Figure 7.1: Forces from boundary data points

computed as follows:

First, the closest point from $\mathbf{z}$ to the corresponding layer of the model is computed based on the algorithm given in Table 7.1. Let $\mathbf{p}$ be the closest point, and $\mathbf{x}_a$, $\mathbf{x}_b$ and $\mathbf{x}_c$ be the nodes of the triangular face where $\mathbf{p}$ belongs. In the process of finding $\mathbf{p}$, the barycentric coordinates [33] $\mathbf{m} = (m_a, m_b, m_c)$ of $\mathbf{p}$ with respect to the nodes of the triangle $\mathbf{x}_a\mathbf{x}_b\mathbf{x}_c$ are also computed:

$$m_a\mathbf{x}_a + m_b\mathbf{x}_b + m_c\mathbf{x}_c = \mathbf{p}; \qquad m_a + m_b + m_c = 1. \tag{7.4}$$

Then the force that $\mathbf{z}$ exerts on the model is computed from

$$\mathbf{f}_z = \gamma_1(\mathbf{z} - \mathbf{p}), \tag{7.5}$$

where γ_1 is the strength of the force. The force $\mathbf{f}_z$ is linearly distributed to the nodes $\mathbf{x}_a$, $\mathbf{x}_b$, and $\mathbf{x}_c$ of the associated triangular face based on the values of $\mathbf{m} = (m_a, m_b, m_c)$:

$$\mathbf{f}_{\mathbf{x}_i} = m_i\ \mathbf{f}_z; \qquad i = \{a, b, c\}. \tag{7.6}$$

Since m_i's are computed from the solution of the linear system in (7.4)[6] (see Appendix C), the following equation is also true:

$$\sum_i m_i\mathbf{f}_z = \mathbf{f}_z. \tag{7.7}$$

Intuitively, each of the m_i's is a weight given to each node of the triangular face and the vector $\mathbf{p}$ is the location of the center of mass of the face.

[6]If all three $\mathbf{x}_i$'s lie on a straight line, or any $\mathbf{x}_i$ is (0,0,0), the linear system does not have a unique solution. But we do not encounter either situation in our case, since $\mathbf{x}_i$'s are the positions of nodes of a triangle, and they are all located away from the origin (0,0,0).

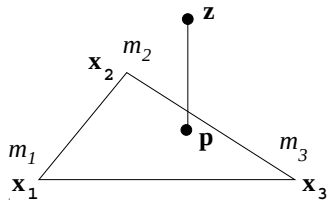

Let $\mathbf{x}_i$ $(i = 1 \cdots 3)$ be position vectors for the nodes of a triangular face of a volume element. To find the closest triangular face on a respective layer of the model from a data point $\mathbf{z}$:

1. Find the triangular face on the respective layer which gives the smallest sum of distances from each node of the triangular face to the data point $\mathbf{z}$.

$$\min \sum_{i=1}^{3} (\mathbf{x}_i - \mathbf{z})^2$$

   The triangle satisfying the above equation is the initial guess.
2. Mark the triangle.
3. Project $\mathbf{z}$ onto the plane defined by the triangle. Let $\mathbf{p}$ be the projected point on the plane.
4. Test if $\mathbf{p}$ falls inside of the triangle:

   Solve for barycentric coordinates m_i's of $\mathbf{p}$ with respect to the triangle (see Appendix C). If all three m_i are non-negative, $\mathbf{p}$ falls inside of the triangle.
5. If $\mathbf{p}$ is not inside the triangle, look for the nearby triangle, which is not marked, based on the values of m_i's and repeat step 2. (Note: If there is no more eligible triangle, compute and return the nearest node instead of closest triangle.)
6. If $\mathbf{p}$ falls inside of the triangle, the triangle is the closest one from the data point $\mathbf{z}$.

Table 7.1: Algorithm: Find the closest triangular face from a point $\mathbf{z}$

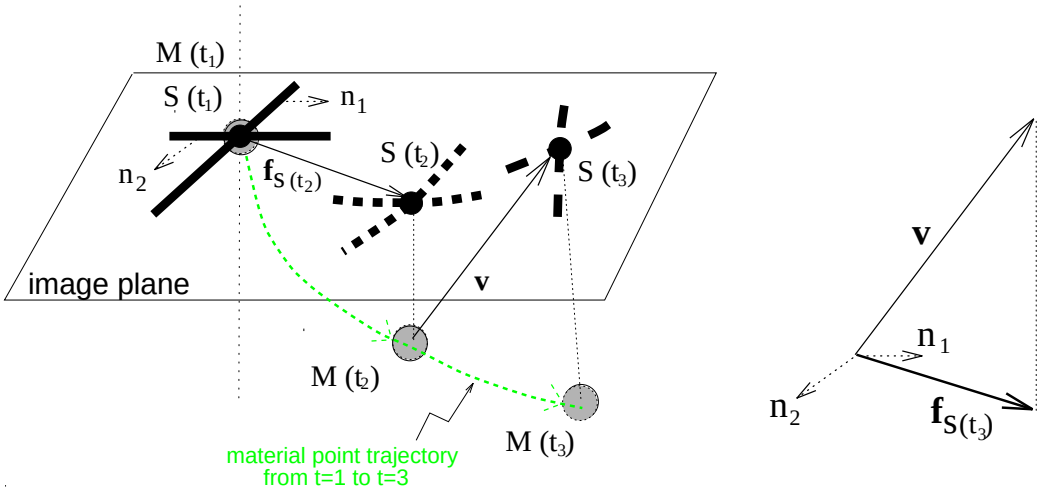

Forces $\mathbf{f}_s(t_2)$, $\mathbf{f}_s(t_3)$ from SPAMM points $\mathbf{S}(t_2)$ and $\mathbf{S}(t_3)$, respectively.

Figure 7.2: Forces from SPAMM data points

7.3.2 Force Computation from SPAMM Data

As opposed to the boundary data, SPAMM data provide correspondence over time of the associated SPAMM points. Initially we assume that the SPAMM data points and the model material points coincide. Let $\mathbf{M}(t_1)$ be the material point which initially coincides with a SPAMM data point $\mathbf{S}(t_1)$ at time t_1 (see Fig. 7.2). Let also $\mathbf{S}(t_2)$ and $\mathbf{S}(t_3)$ be the corresponding SPAMM data points to the point $\mathbf{S}(t_1)$ at the next two time frames. Then the force on $\mathbf{M}(t_1)$ from $\mathbf{S}(t_2)$ is computed as

$$\mathbf{f}_{S(t_2)} = \gamma_2 \, [([\mathbf{S}(t_2) - \mathbf{M}(t_1)] \cdot \mathbf{n}_1) \, \mathbf{n}_1 + ([\mathbf{S}(t_2) - \mathbf{M}(t_1)] \cdot \mathbf{n}_2) \, \mathbf{n}_2], \tag{7.8}$$

where γ_2 is the strength of the force and $\mathbf{n}_1, \mathbf{n}_2$ are the unit normals of the corresponding initial (i.e., at time t_1) tagging planes as shown in Fig. 4.2. The force $\mathbf{f}_{S(t_2)}$ from $\mathbf{S}(t_2)$ to $\mathbf{M}(t_1)$ will cause the material point at $\mathbf{M}(t_1)$ to move to a new position $\mathbf{M}(t_2)$. Subsequently, the force $\mathbf{f}_{S(t_3)}$ on $\mathbf{M}(t_2)$ from $\mathbf{S}(t_3)$ will be computed in a similar fashion and it is shown in Fig. 7.2.

The SPAMM forces $\mathbf{f}_{S(t_i)}$ or $\mathbf{f}_S$ are always parallel to the corresponding image plane and orthogonal to the initial tagging plane of the SPAMM data point. These forces are spring-like forces and are not computed as a result of imposing hard-constraints on the projected motion of a material point. Therefore, when the through-plane motion of a material point is large, the projection of the material point's location on the image plane

1. Find the nearest node of the model from the data point $\mathbf{M}$:

$$\min(\mathbf{x}_i - \mathbf{M})^2.$$

   Let the node $\mathbf{x}_i$ satisfying the above equation be $\mathbf{x}_{near}$.
2. Select one volume element whose node is the nearest node $\mathbf{x}_{near}$.
3. Perform which-side-of-plane tests with the triangular faces along w to determine where in w range $\mathbf{M}$ lies as shown in Fig. 7.3(a).
4. Perform which-side-of-plane tests with the bottom rectangular faces of the volume elements along u to determine where in u range $\mathbf{M}$ lies as shown in Fig. 7.3(b).
5. Perform which-side-of-plane tests with the side rectangular faces of the volume elements along v to determine where in v range $\mathbf{M}$ lies as shown in Fig. 7.3(c).
6. Perform a which-side-of-plane test with the slant rectangular face of the volume elements to determine in which of two volume elements $\mathbf{M}$ lies as shown in Fig. 7.3(d). Now we have found the volume element which encloses the SPAMM data point $\mathbf{M}$.

Table 7.2: Algorithm: Find the enclosed volume element for $\mathbf{M}$

may not exactly coincide with the location of the corresponding SPAMM data point. This is desirable, since in such a case this type of location correspondence is not necessarily valid.

Once we compute the SPAMM forces from each SPAMM data point $\mathbf{S}$, we distribute each force $\mathbf{f}_S$ to the nodes of the prism (i.e., the volume element) within which the corresponding material point $\mathbf{M}$ lies. These nodal forces of the model will cause the dynamic model to deform by estimating the model parameters in Lagrangian dynamics formulation defined in (7.2).

In order to distribute, at any time frame t_i, the computed force $\mathbf{f}_S$ to the nodes of the deformable model, we first determine the enclosed volume element $\mathbf{n}_{A1}\mathbf{n}_{B1}\mathbf{n}_{C1}\mathbf{n}_{A2}\mathbf{n}_{B2}\mathbf{n}_{C2}$ for each SPAMM data point at initial time (which coincides with the corresponding material point $\mathbf{M}$) by performing a series of which-side-of-plane-test to determine which side of a given plane the point lies (see Appendix D). If two adjacent planes give the answers with opposite signs to each other, we know that the point is in-between these two planes.

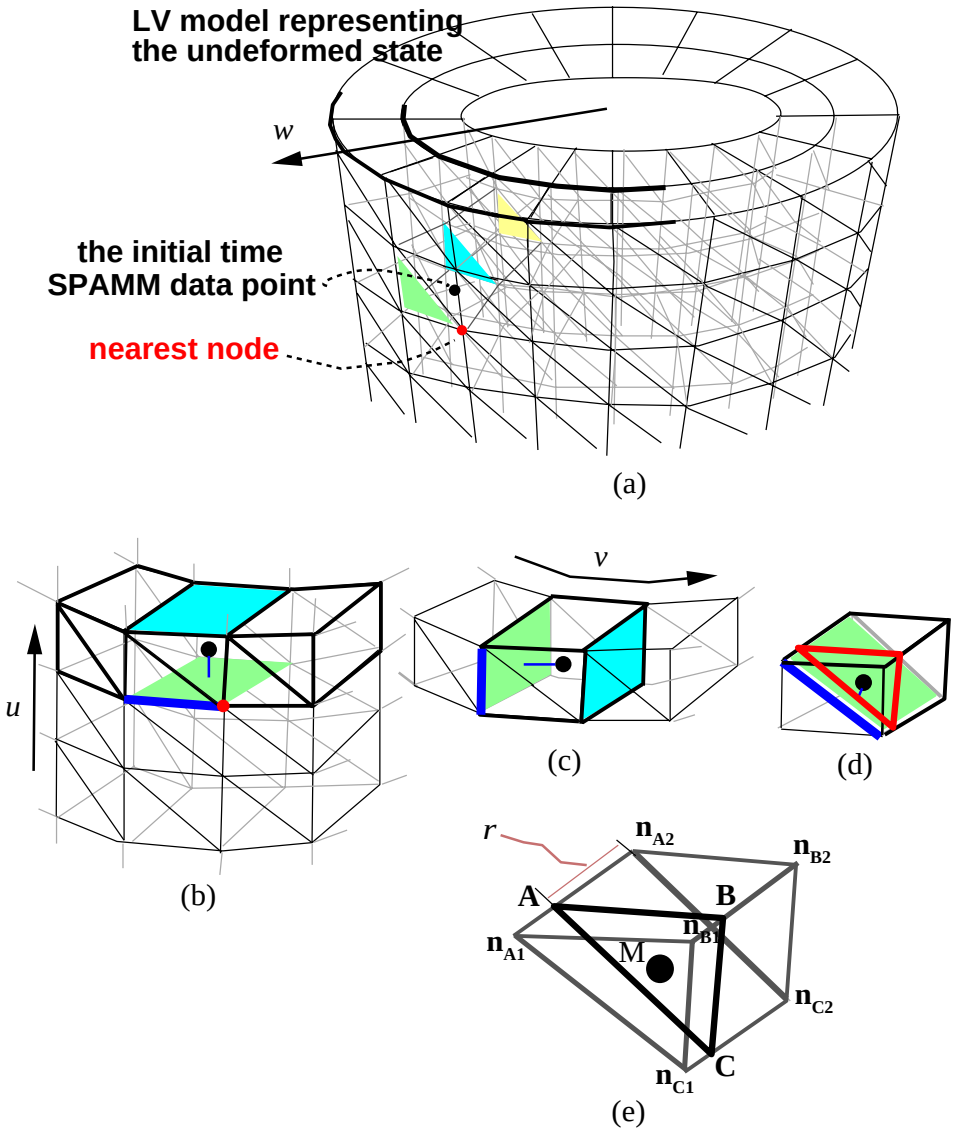

Figure 7.3: Locating the enclosed volume element for a initial time SPAMM data point

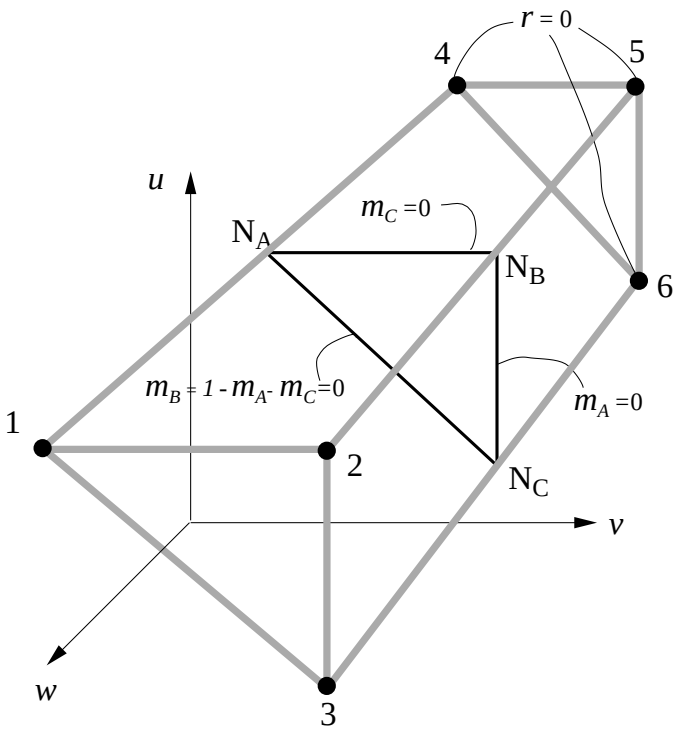

Figure 7.4: Finite volume element

The algorithm is given in Table 7.2.

Based on the finite element theory, we compute a triangle $\mathbf{ABC}$ (see Fig. 7.3(e)) in which $\mathbf{M}$ lies such that

$$r = \frac{\mathbf{A} - \mathbf{n}_{A2}}{\mathbf{n}_{A1} - \mathbf{n}_{A2}} = \frac{\mathbf{B} - \mathbf{n}_{B2}}{\mathbf{n}_{B1} - \mathbf{n}_{B2}} = \frac{\mathbf{C} - \mathbf{n}_{C2}}{\mathbf{n}_{C1} - \mathbf{n}_{C2}}, \tag{7.9}$$

where r is a scalar. To compute r, we solve the following cubic scalar equation using the Newton-Raphson method

$$(\mathbf{M} - \mathbf{A}) \cdot ((\mathbf{C} - \mathbf{A}) \times (\mathbf{B} - \mathbf{A})) = 0, \tag{7.10}$$

where $\mathbf{A}, \mathbf{B}, \mathbf{C}$ are computed with respect to r from equation (7.9).

The force $\mathbf{f}_S$ is then extrapolated to the nodes of triangle $\mathbf{ABC}$ based on the same algorithm we used for the force computation from boundary data. The scalars m_A, m_B and m_C correspond to the barycentric coordinates of $\mathbf{M}$ with respect to the nodes $\mathbf{A}$, $\mathbf{B}$ and $\mathbf{C}$. Then the nodal shape functions for the volume element $\mathbf{n}_{A1}\mathbf{n}_{B1}\mathbf{n}_{C1}\mathbf{n}_{A2}\mathbf{n}_{B2}\mathbf{n}_{C2}$ or $\mathbf{n}_1\mathbf{n}_2\mathbf{n}_3\mathbf{n}_4\mathbf{n}_5\mathbf{n}_6$ as in Fig. 7.4 become

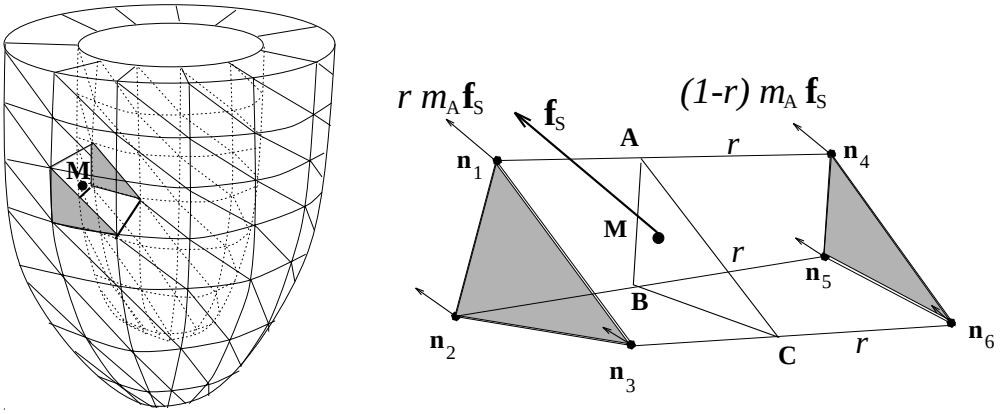

Figure 7.5: Distributing force from a SPAMM data point

$$N_1 = r\ m_A \tag{7.11}$$

$$N_2 = r\ m_B \tag{7.12}$$

$$N_3 = r\ m_C \tag{7.13}$$

$$N_4 = (1-r)\ m_A \tag{7.14}$$

$$N_5 = (1-r)\ m_B \tag{7.15}$$

$$N_6 = (1-r)\ m_C\,. \tag{7.16}$$

Then the forces on the nodes of the volume element $\mathbf{n}_1\mathbf{n}_2\mathbf{n}_3\mathbf{n}_4\mathbf{n}_5\mathbf{n}_6$ are computed based on the nodal shape functions as follows:

$$\mathbf{f}_{S_n} = N_n \mathbf{f}_S \tag{7.17}$$

where $n = 1 \cdots 6$ (see Fig. 7.5).

The computation of r and $\mathbf{m} = (m_A, m_B, m_C)$, which determine the location of the corresponding material point to a SPAMM data point, is only done once at the beginning of the LV motion estimation. It is the correspondence of SPAMM data points over time that allows us to estimate the twisting motion of the LV. In addition, by combining forces from two orthogonal sets of SPAMM data points we estimate the full 3D shape and motion of the LV.

```
make model ()              % assemble meshes
compute model ()           % compute node position

while (!done) {
    clear forces ()
    compute forces from datapoints ()
    compute net applied force and torque ()
    compute translation and rotation ()
    compute deformation ()
    compute model ()
    display model ()
}
```

Figure 7.6: Algorithm: in main() function

7.4 Rigid Motion Recovery

In order to decouple the rigid motion of the deformable model from the non-rigid motion, we compute translational and rotational motion before we recover non-rigid motion (i.e. deformation). After we compute the forces from all data points as described in Section 7.3, we sum up the nodal forces as well as the nodal torque to compute the translation and rotation of the model frame with respect to the inertial frame as follows:

$$\mathbf{f}_{translate} = \sum_l \mathbf{f}_l \ ; \tag{7.18}$$

$$\mathbf{f}_{rotate} = \sum_l \mathbf{s}_l \times \mathbf{f}_l, \tag{7.19}$$

where $\mathbf{f}_{translate}$ is the net applied force, $\mathbf{f}_{rotate}$ is the net applied torque, $\mathbf{f}_l$ is the nodal force where l is the index for a node of the model, and $\mathbf{s}_l$ is the position vector of the node expressed in model frame.

7.5 Implementation

Fig. 7.6 summarizes the overall steps for the shape recovery from the data points. We first construct volumetric meshes and compute the node positions of undeformed LV model based on the definition of the geometry defined in the previous chapter. In order to

recover the shape and motion of the LV model from the data points, we implement first-order Euler's method[7] (Section 7.2) to differentiate the governing dynamics equations: From (7.2) and (3.25) we can write

$$\dot{\mathbf{q}} = \int \mathbf{L}^{\top}\mathbf{f}\, d\mathrm{u}. \tag{7.20}$$

The forces from data points are computed as described in Section 7.3. We then compute the net applied force and torque to compute the rigid motion. The model Jacobians allow us to "distribute" the appropriate forces to the model parameter space. With a new set of parameter values, we compute the updated position of the nodes of the model.

[7] It is the while-loop in Fig. 7.6.

Chapter 8

Model Parameters

The parameters of the LV model that are estimated during the fitting process reflect the shape changes during systole. The deformable model has six parameter functions in $\mathbf{q}_s$ as defined in (6.9)[1], which can be interpreted intuitively without complex post-processing as summarized in Table 8.1. In addition, the model has global translation $\mathbf{q}_c$ and global rotation $\mathbf{q}_\theta$ parameters (see (3.22)).

Parameters	Representation
a_1, a_2	Radial contractions
a_3	Longitudinal contraction
τ	Twisting about the long axis
e_{1_o}, e_{2_o}	Long axis deformation

Table 8.1: Model parameters

8.1 Orientation of Model

The initial orientation of the model is important in order to understand the role of each parameter. As depicted in Fig. 8.1, the short and long axis views initially coincide with the xy- and yz- planes in the model frame of reference. The center of the model is chosen at the centroid of the LV with the y-axis pointing towards the right ventricle (RV). The

[1]There are seven model parameters altogether in $\mathbf{q}_s$. However, the scaling parameter a_0 is used only at the initial shape recovery and remains constant during motion estimation. Therefore, the remaining six parameters will provide the degrees of freedom of the model with respect to the deformation parameters.

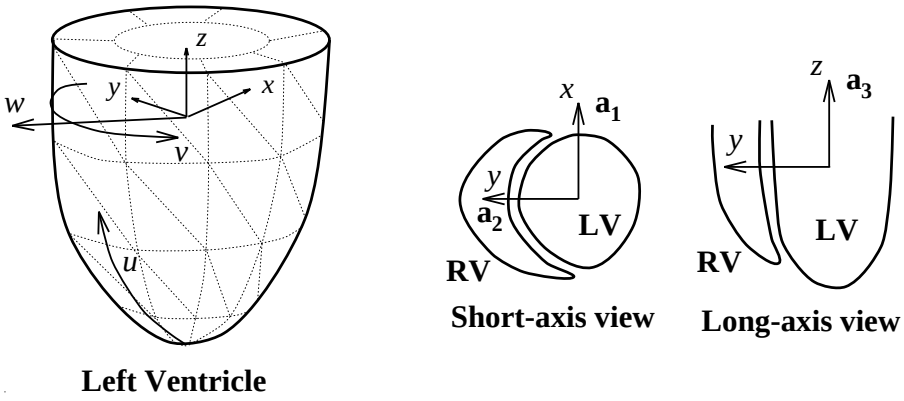

Figure 8.1: Definition of model's coordinate system

material coordinates are $\mathbf{u} = (u, v, w)$, where u runs from the apex to the base of the LV, v starts and ends at the point where the septum is located, and w is used for the definition of model points between the inner and outer walls of the deformable model. The parameter functions we use are functions of $\mathbf{u}$, so that we can model accurately the local variation throughout the LV. As we demonstrate in the following sections, the variation of those parameters with respect to u, v, and w is chosen so that they are mutually independent.

In the following section, we present in detail the interpretation and use of each of the model's parameters. Table 8.1 summarizes what each parameter function captures during the 3D shape and wall motion estimation of the LV.

8.2 Deformation Parameters

8.2.1 Radial Contraction

Since the short axis views coincide initially with the xy-plane[2], the parameter functions a_1 and a_2 (which are the aspect ratios along the x- and y-axes of the LV model, respectively) will capture the radial contraction motion. Since the y-axis points towards the septum of the heart, the a_2 parameter captures the motion of the constrained wall, while the a_1 parameter captures the motion of the free wall as shown in Figs. 8.2(a-b). For each time frame t, we estimate the values of $a_1(u, w)$ and $a_2(u, w)$, and compute the percentage of the

[2]The xy-plane does deviate over time from the short axis view due to the global rotation of the LV, but not significantly.

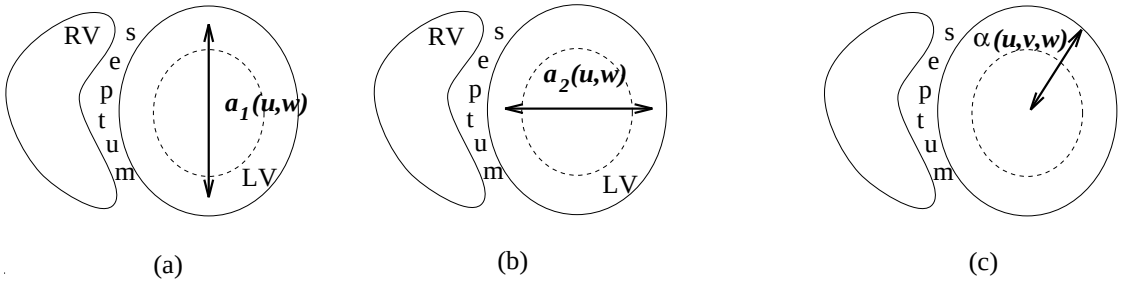

Figure 8.2: Parameters for radial contraction

change with respect to their values at end-diastole (ED) which corresponds to the initial time frame (or t_{ED}). For example, the graphs shown in Fig. 10.13(a) are the plot of a_1 computed as follows:

$$\frac{a_1(t) - a_1(t_{ED})}{a_1(t_{ED})} \times 100.$$

We may combine parameters $a_1(u, w)$ and $a_2(u, w)$, as one parameter $\alpha(u, v, w)$ to model the radial contraction of the LV (see Fig. 8.2(c)). In this way we can also capture the circumferential variation (i.e., along v) of the radial contraction. In this case, the generalized primitive $\mathbf{e}' = (e'_1, e'_2, e'_3)^\top$, which is previously given as $\mathbf{e}$ in (6.2), will become

$$\begin{aligned} \mathbf{e}' &= \mathbf{e}'(\mathbf{u}; a_0, \alpha(\mathbf{u}), a_3(\mathbf{u})) && (8.1) \\ &= a_0 w \begin{pmatrix} \alpha(\mathbf{u}) \ \cos u \ \cos v \\ \alpha(\mathbf{u}) \ \cos u \ \sin v \\ a_3(\mathbf{u}) \ \sin u \end{pmatrix}, && (8.2) \end{aligned}$$

and the final geometric definition of the reference shape $\mathbf{s}'$ will become

$$\begin{aligned} \mathbf{s}' &= \mathbf{T}_t(\mathbf{e}'; \tau(\mathbf{u})) && (8.3) \\ &= \begin{pmatrix} e'_1 \cos(\tau(\mathbf{u})) - e'_2 \sin(\tau(\mathbf{u})) \\ e'_1 \sin(\tau(\mathbf{u})) + e'_2 \cos(\tau(\mathbf{u})) \\ e'_3 \end{pmatrix}. && (8.4) \end{aligned}$$

Note that in this case the axis offset deformation $\mathbf{T}_o$, given in (6.8), will not be applied in order to maintain the parameter independence.

8.2.2 Longitudinal Contraction and Global Translation

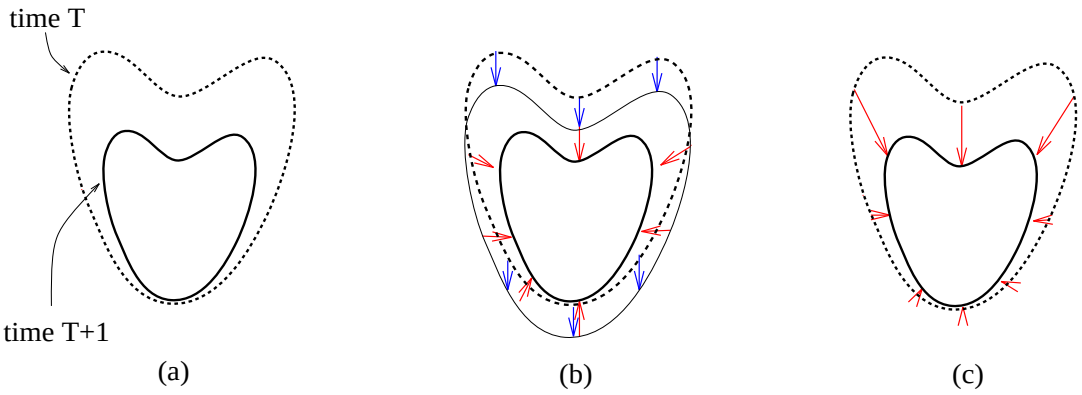

Figure 8.3: Parameters for longitudinal contraction and global translation

Since the long axis views coincide with the yz-plane, the parameter function a_3 (which is the aspect ratio along z-axis) will capture the longitudinal contraction motion. However, since we do not have enough time frames over the heart cycle, the estimation of the global translation in the z direction of the model frame can be arbitrary (the two parameters can't be independently estimated) and may result in the false estimation of the longitudinal deformation parameters (the global translation in the x and the y directions of the model frame is negligible). Consider the case shown in Fig. 8.3(a). It is a typical motion of the LV observed at two subsequent time instances (T and $T+1$), which shows that the motion at the apex of the LV is relatively small. Suppose that the length of the LV is $10cm$ and $8cm$, at times T and $T+1$, respectively. If the origin of the model frame at time T is at the half way along the LV, the origin would globally translate $1cm$ at time $T+1$. Yet this amount of translation is arbitrary because it depends on where the origin is. Moreover, in this case we would capture a relatively uniform longitudinal contraction from apex to base as shown in Fig. 8.3(b). This has the result that, even though the combination of translation and longitudinal contraction would give the correct 3D motion of the LV, the longitudinal contraction would lose its intuitive meaning. However, as mentioned above this is an artifact of the sparse sampling over time.

Due to the above sparse sampling, and the fact that we could not observe a significant overall translation of the model in all our datasets, we kept the global translation constant during the fitting process for the subsequent time frames. We therefore capture the LV

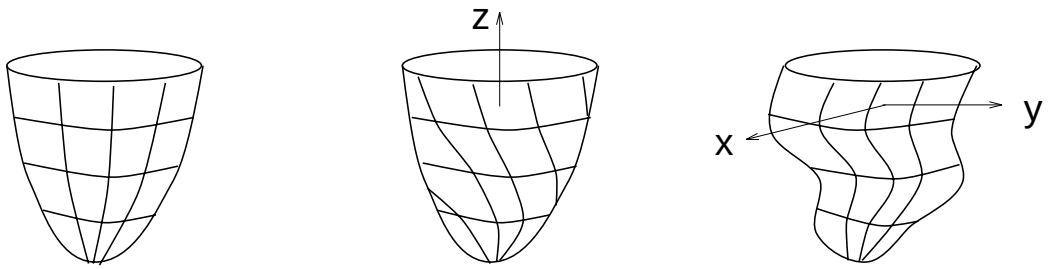

(a) undeformed (b) twisted (c) with axis offsets

Figure 8.4: Twisting and long axis deformations

longitudinal motion as a deformation based on a_3 (see Fig. 8.3(c)). In our experiments, we compute the actual displacement based on the a_3 parameter as follows:

$$a_{3_d} = a_3(t)\sin(u) - a_3(t_{ED})\sin(u).$$

We plot the percentage of the changes with respect to the initial length of the LV in order to compare the amount among different LVs. For example, the graphs shown in Fig. 10.13(c) are the plot of a_3 computed as follows:

$$\frac{a_{3_d}}{\text{length of the LV}} \times 100.$$

In a pathological case where the LV translates (globally) significantly along the z axis in addition to contracting, we can very easily estimate this global translation by simply subtracting from a_{3_d} the common least amount of deformation from apex to base. However, it is not clear that such knowledge of the global translation is clinically useful.

8.2.3 Twisting and Global Rotation

The twisting parameter function $\tau(u, v, w)$ captures the twisting about the long axis of the LV as shown in Fig. 8.4(b). For each location w, and for each location u, we allow the parameter to vary along v in order to obtain the variation of twisting as a function of circumferential position as well. The average of the twisting values at all the circumferential positions for each location u is plotted in Fig. 10.13 and Fig. 10.14. In this way we quantify the twisting motion from the apex to the base of each LV.

At each subsequent time frame, we first estimate the global rotation of the model before

estimating the deformation parameters. This allows us to subtract the global rotation from the twisting deformation, and therefore estimate the overall tilting of the LV.

The global rotation of our model is expressed as a quaternion. This results in a numerically more robust estimation of global rotation during model fitting to the data [60]. In addition, from the quaternion we can compute very efficiently the corresponding rotation matrix $\mathbf{R}$ (see Appendix B) that is used to compute the nodal positions $\mathbf{x}$ from equation (3.3).

8.2.4 Long Axis Deformation

By having the axis-offset parameters $e_{1_o}(u, w)$ and $e_{2_o}(u, w)$, we allow the centroid of each cross section at a different location along the long-axis of the LV to displace globally in the xy-plane (see Fig. 8.4(c)). In this way we can capture the shape of the LV accurately, and at the same time observe the bending of the LV, if any, without using any special function for the bending.

8.3 Global Measures and Other Parameters

8.3.1 Ejection Fraction

By adapting Gauss's theorem [72] we can accurately calculate over time the volume of the blood pool, and therefore compute ejection fraction. In order to compute the volume of the cavity, we first find the centroid of the base of LV and close the cavity with triangular faces whose common node is the centroid as shown in Fig. 8.5. Then the blood pool can be represented by a closed polyhedron of k triangular faces. Let $F_1 \cdots F_n$ be the triangular faces of the polyhedron, and $\mathbf{N}_i$ be the unit normal vector of F_i $(i = 1 \ldots n)$. Furthermore, let $\mathbf{P}_{i_1}$, $\mathbf{P}_{i_2}$ and $\mathbf{P}_{i_3}$ be the position vectors for the nodes of face F_i in counter-clockwise order. According to Gauss's theorem, the volume of the polyhedron is computed as follows:

$$\text{Volume(polyhedron)} = \frac{1}{3}\left|\sum_i (\mathbf{P}_{i_1} \cdot \mathbf{N}_i)\ \text{Area}(F_i)\right|, \tag{8.5}$$

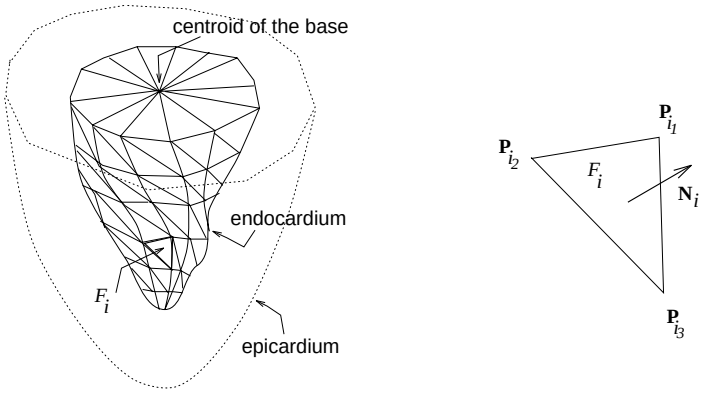

Figure 8.5: Blood pool volume

where the area of each face is

$$\text{Area}(\text{S}_\text{i}) = \frac{1}{2}\left|\mathbf{N}_i \cdot (\sum_{k=1..2} \mathbf{P}_{i_k} \times \mathbf{P}_{i_{k+1}})\right|. \tag{8.6}$$

The ejection fraction (EF) is then the ratio of the volume at end-systole to the volume at end-diastole:

$$\text{EF} = \frac{\text{Volume(blood pool at } t_{ES})}{\text{Volume(blood pool at } t_{ED})} \times 100. \tag{8.7}$$

8.3.2 Wall Thickening

We can also compute the change in thickness of the ventricular wall which is extensively used by clinicians from α parameter (see equation (8.2)). The thickness of a wall at a particular cross-sectional location u_o and v_o is

$$\text{wall thickness at } (u_o, v_o) = w_{max}\alpha(u_o, v_o, w_{max}) - w_{min}\alpha(u_o, v_o, w_{min}), \tag{8.8}$$

where w_{max} and w_{min} refer to the w coordinates of outer most layer and the inner most layer, respectively, of the model. Then the wall thickening (WT) at any cross-sectional location can be computed as follows:

$$\text{WT}(u, v) = \frac{\text{wall thickness at } (u_o, v_o) \text{ at } t_{ES}}{\text{wall thickness at } (u_o, v_o) \text{ at } t_{ED}}. \tag{8.9}$$

8.3.3 Other Parameters

It is also very important to note that our technique for constructing these deformable models is general and we can therefore add other global deformations such as bending

and shearing. However, for the experiments we have conducted, the parameters that were described above were adequate. If needed, it is also possible to do strain analysis based on the extracted model parameters. Once we recover the model parameters, we can always go back and compute the nodal positions, $\mathbf{x}_i$, of the volume elements from equation (3.3). Then we may apply the standard strain computation procedure as in [113].

Part III

Experiments, Visualization, and Validation

Part Overview

The third part of the thesis focuses the experiments with the proposed technique. We have first conducted feasibility studies by defining the *surface* deformable model with parameter functions and applying it to the 3-D tagged data sets, which are sampled at the LV mid-wall from already constructed finite element models. The results are provided in Chapter 9. In Chapters 10 and 11, we provide the implementation of the proposed *volumetric* models as well as the experiments with MRI-SPAMM data from normal and abnormal heart. We describe the error analyses and validation studies in Chapter 12.

Chapter 9

Feasibility Study

9.1 3-D Tagged Data

Before we develop the apparatus for cardiac motion studies based on MRI-SPAMM, we have tested the modeling paradigm with parameter functions using processed 3-D tagged data points (courtesy of Dr. Alistair Young who was with the Radiology Department at the University of Pennsylvania, and currently with the University of Auckland in New Zealand). The main goal was to test the **hypothesis** that *there are a small number of geometrically meaningful parameters which can describe the left ventricular wall motion in an intuitive way.* We have verified the hypothesis based on the surface DMPF, which is briefly described in Section 9.2 and was presented in [76, 78]. The present thesis is the extension of the technique which also works on the "raw" MRI-SPAMM data themselves [74, 75].

The most popular LV models are the finite element model (see Section 5.2). However, the finite element model results in a large number of model parameters which must be post-processed to provide meaningful geometric information on the nature of the deformation. For the studies in this chapter, the finite element model was used simply to provide a set of material points over time. The set of 3-D tagged material points from the finite element model was then used as an input to our technique.

In the following sections, we first define of the surface model utilized in this feasibility study, explain how the data points are obtained, and finally present the experimental results

from LV data sets of healthy volunteers and patients with hypertrophic cardiomyopathy.

9.2 Surface Model Definition

The class of DMPF allows the use of global parameters that can characterize an object's shape in terms of a few parameter functions. The LV model utilized for the feasibility study is a 3D surface, whose material coordinates $\mathbf{u} = (u, v)$, and the reference shape is defined by seven model parameters (a_0, a_1, a_2, a_3, τ, e_{1_o}, e_{2_o}) as follows:

$$\mathbf{s} = \begin{pmatrix} e_1 \cos(\tau(u)) - e_2 \sin(\tau(u)) \ + \ e_{1_o}(u) \\ e_1 \sin(\tau(u)) + e_2 \cos(\tau(u)) \ + \ e_{2_o}(u) \\ e_3 \end{pmatrix} \tag{9.1}$$

$$\begin{aligned} \text{where} \quad & e_1 = a_0\, a_1(u)\, \cos u\, \cos v, \\ & e_2 = a_0\, a_2(u)\, \cos u\, \sin v \\ \text{and} \quad & e_3 = a_0\, a_3(u)\, \sin u. \end{aligned}$$

The model parameters have the same meanings as described in Table 8. We have also experimented with deformations such as oblique (non-planar) bending (see [76]), but did not find them clinically relevant. Note that the above defined parameters are carefully chosen so that they represent independent degrees of freedom.

By incorporating the geometric definition of the models into the physics-based framework (see Chapter 7), we create dynamic models that deform due to forces exerted from data points and conform to the given data set. The forces are computed based on the similar algorithm given in Section 7.3.1 for the shape recovery from the data representing the undeformed LV (i.e., at end diastole). During the fitting of subsequent time frames, the forces are computed based on the displacements between the current position of a material point and the position of the corresponding data point at the immediately following time phase. Since the tagged dataset provides correspondence over time of individual 3-D material points, we apply the force distribution algorithm (see (7.6)) only once for the initial frame. In subsequent frames, the corresponding points will exert a force to the same point on the model as computed in the first time frame. Once these forces are computed we use

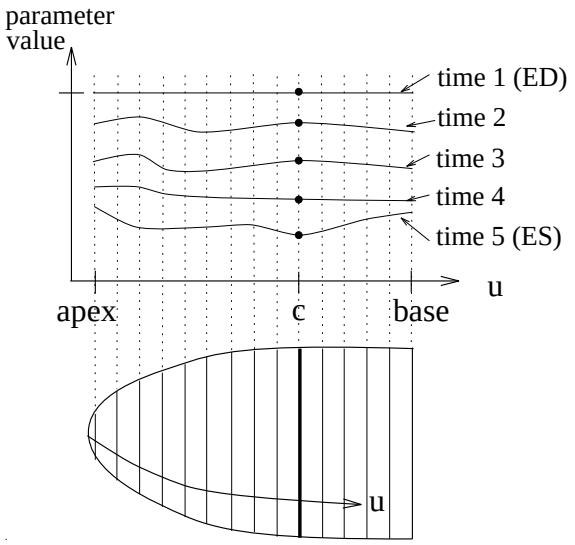

Figure 9.1: Interpretation of parameter graphs

a Lagrangian dynamics formulation to estimate the model parameters. The parameters of the LV model that are estimated during the fitting process directly reflect the shape changes during systole.

As we can see from the definition in (9.1), the parameter functions for the LV model are functions of u – i.e., varying along the long axis of the LV[1]. Fig. 9.1 depicts how we plot the parameter functions in the graphs shown in Fig. 9.4 and Fig. 9.6. The parameter values are plotted as a function of u, which varies from the apex to the base of an LV, for each time frame t ($t = 1 \cdots 5$). In this way, we can observe their variation along the long axis of the LV (u) for each time frame. As an example, in Fig. 9.1 we show how to observe the parameter value changes during systole at the long axis location $u = c$.

9.3 Experimental Results

The datasets used in the current study comprised 400 material points each, whose position described the geometry and motion of the mid-wall surface of the LV during systole. The mid-wall data was obtained from 3D reconstructions of the geometry and motion of the LV from a high-order finite-element model, based on a least-squares based approach [performed

[1] The model coordinate systems are the same as shown in Fig. 8.1 except that the surface model has one layer of w.

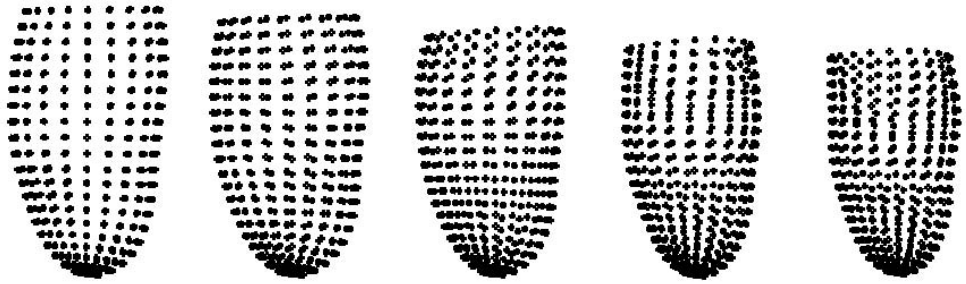

Figure 9.2: 3-D tagged data sampled at the mid-wall of FEM

by Young *et al.* [109, 108, 114] (see Section 5.2)]. The mid-wall surface of the model was sampled to provide a set of material points equally spaced around the surface. This data set (see Fig. 9.2) was then used as input for the experiments presented below.

The proposed technique was applied to the LV mid-wall data sets from two healthy volunteers (V1, V2) and two patients with hypertrophic cardiomyopathy (P1, P2).

9.3.1 Normal LVs in Systole

Fig. 9.3 shows two different views of the model fitting results to data from a normal heart taken over 5 time sequences during systole (from end-diastole ($t = 1$) to end-systole ($t = 5$)). We can easily observe the contraction as well as twisting of the model. The non-rigid motion of the LV are fully described by the set of model the parameter functions. Futhermore, based on the model parameter functions without any complex post-processing, we can quantify the observed variations along the long axis of the LV over time.

In Fig. 9.4 we plot some of the extracted model parameter functions over the five time frames for the normal heart. Figs. 9.4(a) and (b) show the plots of the model's parameter functions $a_1(u)$ and $a_2(u)$, which are associated with its length in the x and y directions, respectively. For each frame we plot the percentage of change in each parameter function during frame $t = 2...5$, with respect to its value at the initial frame ($t = 1$). Fig. 9.4(c) shows plots of the displacement of the length along the z direction computed from the parameter function $a_3(u)$. Fig. 9.4(d) shows plots of the model's twisting parameter function $\tau(u)$. Finally, Figs. 9.4(e) and (f) show plots of the model's long axis deformation

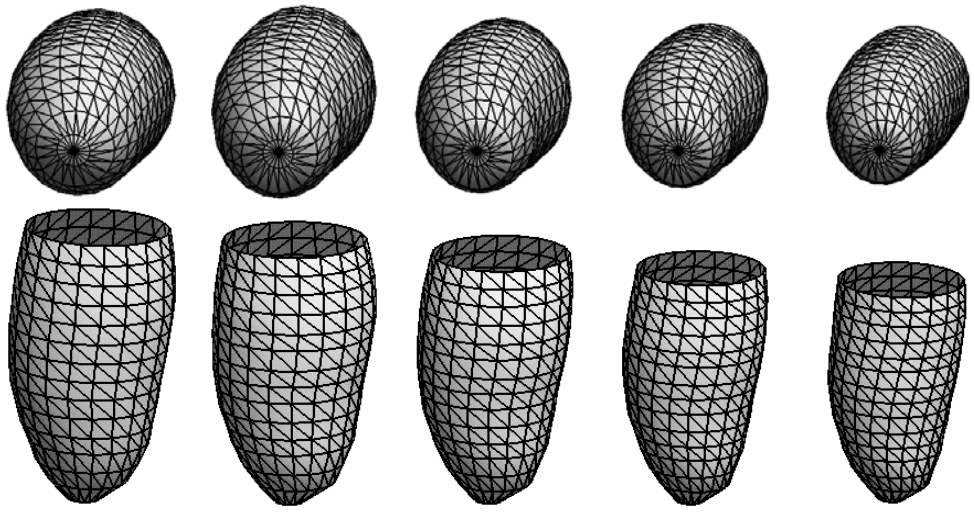

(a) time 1 (ED) (b) time 2 (c) time 3 (d) time 4 (e) time 5 (ES)

Figure 9.3: Model fitted to SPAMM data (LV mid-wall) from a normal heart during systole

parameters $e_{1_o}(u)$ and $e_{2_o}(u)$, respectively.

From these graphs, we can quantify the shape and motion of the LV during its systole. For example, by studying the graphs of $a_1(u)$ and $a_2(u)$ (Figs. 9.4(a,b)), we can conclude that the magnitude of contraction in the radial direction (i.e., along the x- and y-axes) during systole is approximately $20-25\%$. While the graph of a_1 shows uniform contraction along the long axis of the LV, the graph of a_2 shows less contraction towards the base of the LV making the base look more elliptical. This result supports clinical study findings where more stress is exerted at the apex during the LV motion, and also there is an increased similarity of the LV base shape to an ellipse, during systole. We measure from the graph shown in Fig. 9.4(c), that the total displacement along the z-axis, which corresponds to contraction along the z-axis, is approximately 18 mm, where the length of the LV is approximately 75 mm. Therefore, the contraction along the z-axis known as longitudinal contraction is approximately 24% for this LV. From the graph in Fig. 9.4(d), we can quantify the twisting motion of the LV during systole to approximately 18 degrees. The graph shows that there is a small amount of twisting in early systole with gradual increases towards end-systole. Finally, from the long axis deformation parameters (or axis offset parameters) shown in Figs. 9.4(e-f), we observe that there are only slight deformations and most of the deformation appears towards its apex and base, capturing a bending

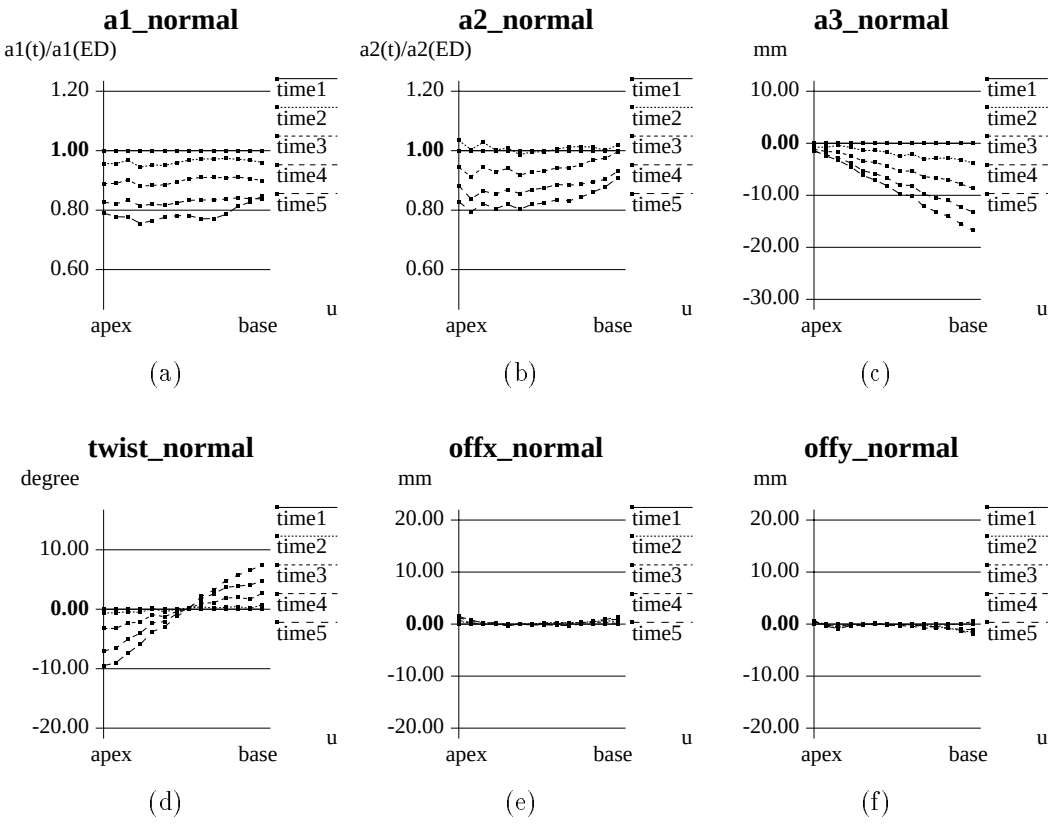

Figure 9.4: Extracted model parameters as functions of u for the normal heart

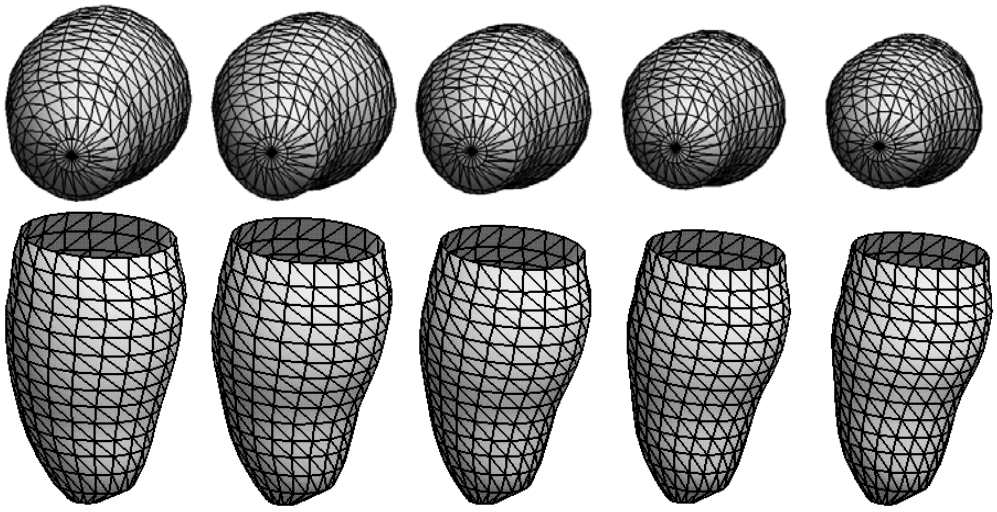

(a) time 1 (ED) (b) time 2 (c) time 3 (d) time 4 (e) time 5 (ES)

Figure 9.5: Model fitted to SPAMM data from an abnormal heart during systole

motion of the long axis. By having the graphs of the parameter functions plotted next to the animation, we can quantify and easily characterize a detailed motion of the deforming model along its long-axis and over time.

We applied our technique to another normal LV to verify the result and we found that the extracted parameter functions were very similar to those shown in Fig. 9.4. The overall contraction was approximately 25%. Like in the other normal LV, there was less contraction (defined by a_2) along the y-axis towards the base of the LV compared with the contraction towards the apex. The second normal heart was known to have greater twisting motion during systole. Surprisingly, we found that the LV underwent greater global rotational motion initially, before twisting. Fig. 9.9(a) shows the twisting parameters at the end-systole for both normal LVs. The twisting angle during systole was quantified to be approximately 20 degrees.

9.3.2 Abnormal LVs in Systole

To further evaluate our model fitting technique, we also fit our model to abnormal heart data from two patients with hypertrophic cardiomyopathy. Abnormal hearts with hypertrophic cardiomyopathy are generally bigger in size, but do not pump as well as normal hearts do. While the results were similar for these two abnormal hearts, they were different

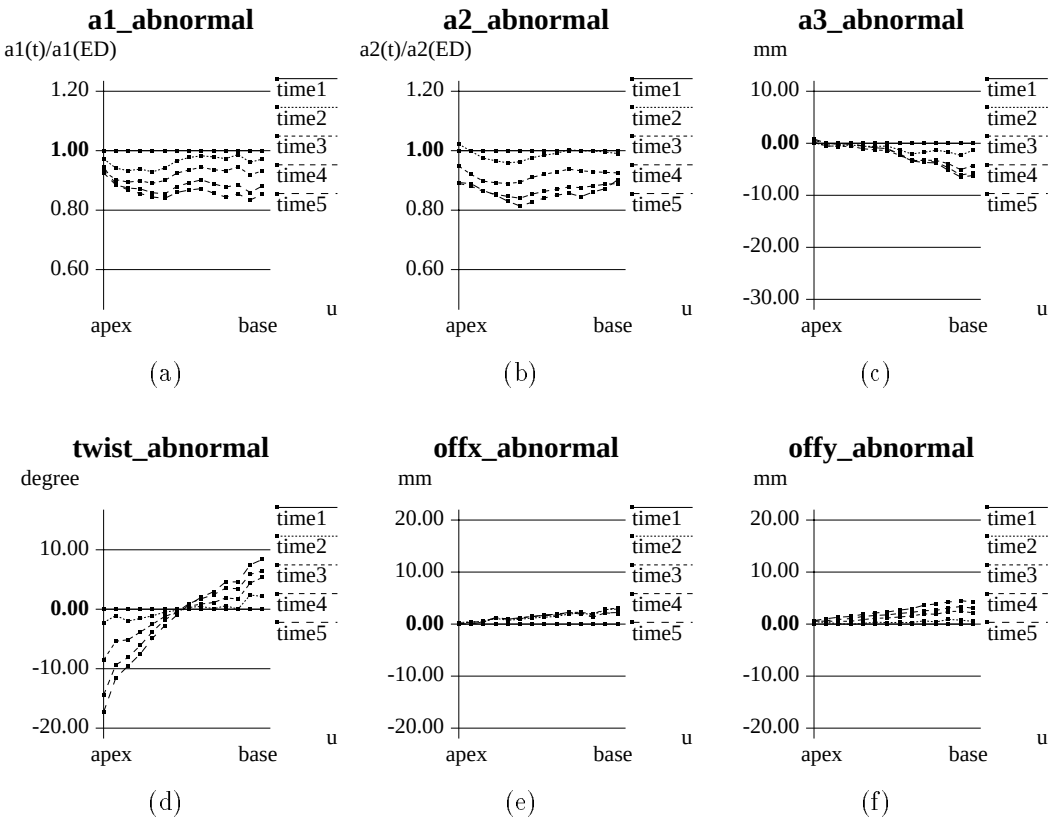

Figure 9.6: Extracted model parameters as functions of u for the abnormal heart

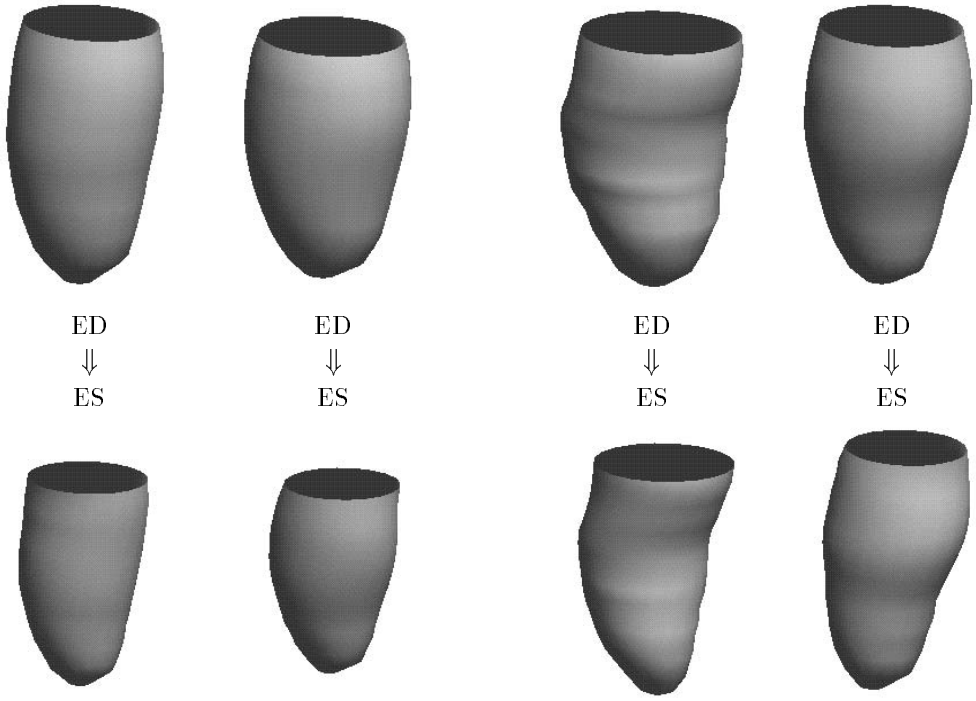

(a) Volunteer 1 (b) Volunteer 2 (c) Patient 1 (d) Patient 2

Figure 9.7: Models fitted to four subjects

from those we obtained for the normal hearts. Fig. 9.5 shows the fitted models to one of the abnormal heart data, while Fig. 9.6 shows graphs of the model's parameter functions which may be compared with the normal heart's model parameter functions, shown in Fig. 9.4. The radial contraction of the abnormal heart is approximately $15-20\%$, and the longitudinal contraction is approximately 7%[2]. Note that the overall contraction decreases significantly towards the apex. The twisting motion during its systole is approximately 27 degrees. Finally, from the graphs shown in Figs. 9.6(e,f), we observe that there is greater long axis deformation compared with the normal LVs.

9.3.3 Comparing Normal and Abnormal LV Parameters

The top row of Fig. 9.7 shows 4 fitted models[3] at the end-diastole: the first two are of healthy volunteers (V1 and V2), and the other two are of patients with hypertrophic

[2]Total displacement along the z-axis is approximately 7 mm where the normalized length of the LV is 107 mm.

[3]Note that all the model fitting results are within an acceptable error bound, since RMS errors are less than 0.5 mm, where the length of the hearts is approximately 100 mm.

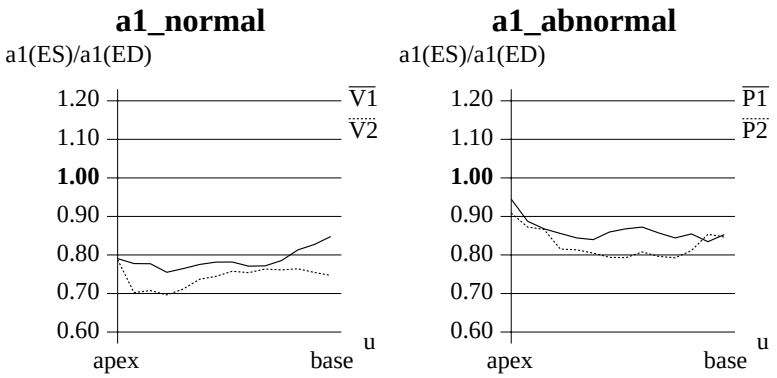

(a) Normal hearts (b) Abnormal hearts

Figure 9.8: Extracted LV parameter $a_1(u)$ at end-systole (mid-wall)

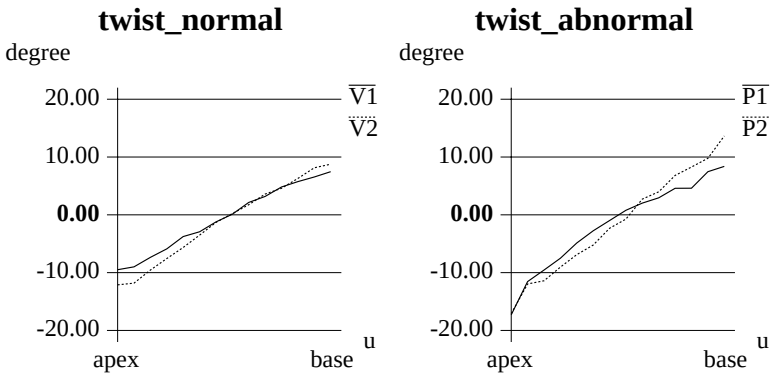

(a) Normal hearts (b) Abnormal hearts

Figure 9.9: Extracted LV parameter $\tau(u)$ at end-systole (mid-wall)

cardiomyopathy (P1 and P2). The second row of Fig. 9.7 shows the corresponding LV at the end-systole. As shown in the figure, the LVs with hypertrophic cardiomyopathy are bigger in size than the normal LVs. Fig. 9.8 and Fig. 9.9 show plots of extracted parameters at end-systole for two normal, and two abnormal LVs. The extracted parameter functions $a_1(u)$ (shown in Fig. 9.8), where the radial contraction of a heart is captured, show that the abnormal hearts contract much less than the normal hearts, especially towards the apex. The extracted twisting parameter functions (shown in Fig. 9.9), however, show that the abnormal hearts twist more than the normal hearts. It seems that the abnormal hearts twist more, perhaps to compensate for their inability to contract as much as a normal heart. As we plotted the graphs of extracted parameters from the fitting process, not only can we observe the results qualitatively, but also we can measure the changes quantitatively. Therefore, we are able to quantitatively verify a result about the above abnormal hearts that was qualitatively evident to physicians.

9.4 Summary

The significant aspect of DMPF is that their global parameters are functions allowing the representation of complex shapes with a few intuitive parameters. In this feasibility study, we were able to eliminate the need for calculation of local deformation parameters that require nontrivial processing to provide a compact and intuitive representation of shape. Using this new family of primitives which are defined based on parameter functions, we were able to capture and quantify the LV motion and shape changes in an *intuitive* way. In particular, the applicability of the technique was demonstrated to the shape and motion analysis of the mid-wall of the LV for normal and abnormal hearts during systole, from 3-D tagged data. In the following chapter, the experimental results with **volumetric** DMPF applied to MRI-SPAMM data is presented.

Chapter 10

Experiments

10.1 MRI-SPAMM Imaging Protocol

We present experiments where we used magnetic tagging (MRI-SPAMM) to acquire data points from the LV during systole. As discussed in Chapter 4, we can obtain only the in-plane motion from MRI-SPAMM images acquired over time. In order to assess the 3-D motion of material points of the LV from the set of such 2-D time-varying data, we need to combine, through a model-based approach, two sets of data obtained from mutually orthogonal image planes.

We have applied the proposed approach to MRI-SPAMM image data pre-acquired at the Hospital of University of Pennsylvania under the supervision of Dr. Leon Axel. The spin-echo techniques, which averages 128 beats per image, were utilized in acquiring the

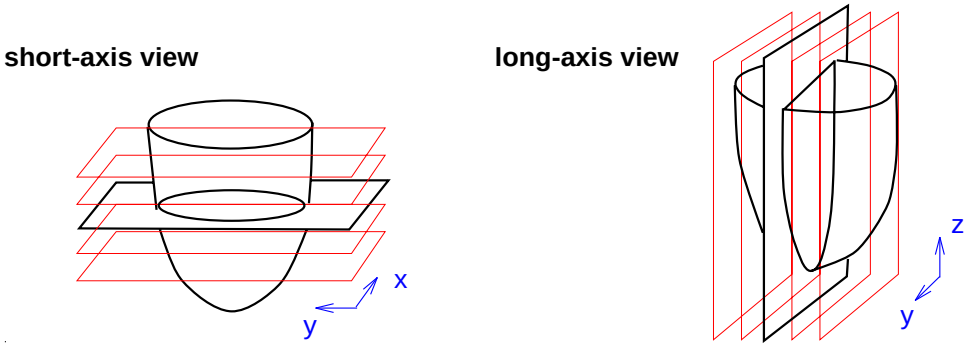

Figure 10.1: Imaging protocol

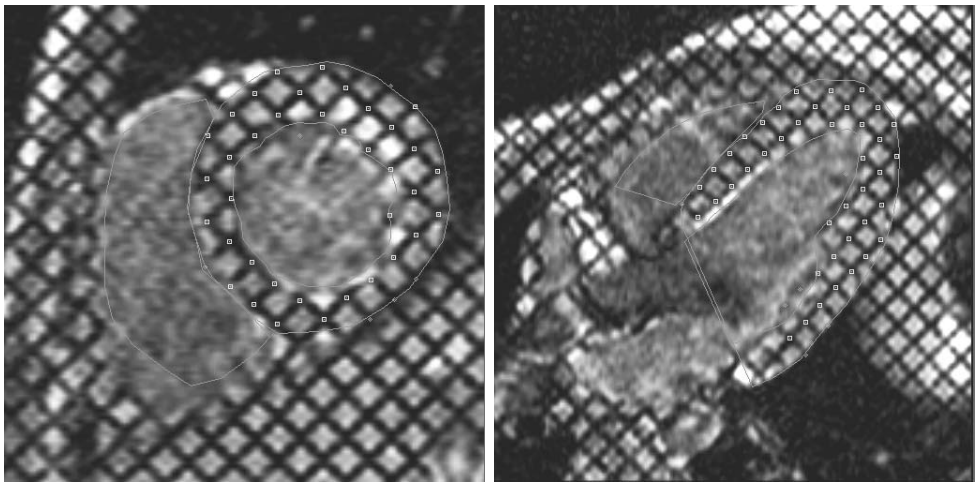

(a) Short-axis (SA) view (b) Long-axis (LA) view

Figure 10.2: Two orthogonal image planes

images[1]. The images are obtained in a series of five parallel short-axis (SA) slices and an orthogonal series of five long-axis (LA) slices, with 10-15 mm spacing (see Fig. 10.1). The thickness of each slice was 5 mm. As described in [112], the long axis of the LV was chosen to pass through a point at the left of the aortic root and the most anterior left point on the LV apex as seen in an initial scout series of coronal images. The short-axis view was taken to be perpendicular to the long axis of the LV. The centers of SA and LV slices are approximately at mid-ventricle. 5 images were acquired at each location at different phases of systole from end-diastole (ED) to end-systole (ES). End-diastole was determined by detecting the rising R wave of the electrocardiogram, and end-systole was defined as the instant when the the cavity area in the mid-ventricle is the smallest. The SPAMM tagging pulse sequences was applied at end-diastole, which last during systole, having 7 mm stripe spacing with approximately 2 mm stripe width.

As described in Chapter 4, SPAMM data points, which are defined as the intersection of the grids, are extracted semi-automatically using active-contours (see Section 4.2.3) from each 50 image planes[2] which span the spatial extent of an LV. Fig. 10.2 shows two orthogonal images (SA and LA) where the extracted SPAMM data points within the LV

[1] In this thesis, we have not used the recently acquired data with the "breath-hold" technique.

[2] We have five short-axis view planes, and another five long-axis view planes. For each image plane, we have datasets over five time sequences during systole. Therefore, we have $(5 + 5) \times 5 = 50$ data sets altogether.

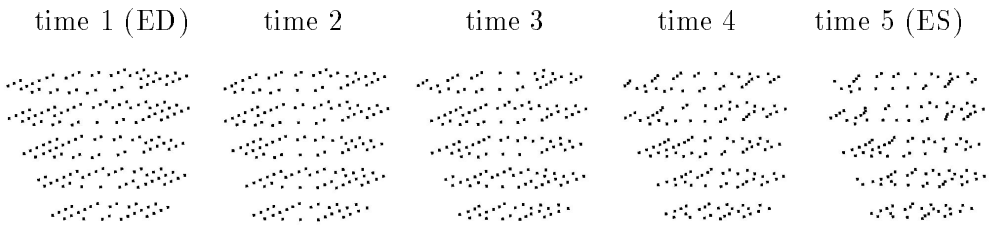

(a) SPAMM data points from short-axis view image planes

(b) SPAMM data points from long-axis view image planes

Figure 10.3: SPAMM data sets

myocardium are marked with white square dots. It is important to mention that the SPAMM data points in the two orthogonal sets of image planes do not correspond to the same material points, but to different material points. In addition to the SPAMM data points, boundary data points from the inner and outer LV walls are also extracted using active contour models and manual initialization (from a custom-made software SPAM-MVU [5, 114]).

Fig. 10.3 and Fig. 10.4 show a set of SPAMM data points for 5 time phases during systole and a set of boundary data points at end-diastole, respectively. Since some of the SPAMM data points on the image plane disappear and/or reappear at subsequent times, we use at every time frame only those points which have a corresponding point at the previous time frame.

10.2 Implementation

The implementation dmpf of the present thesis is written in the C programming language, utilizing the OpenGL^{TM} graphics system and the OSF/Motif^{TM} user interface. The initial model is created by inputting to the computer program dmpf a configuration file where the number of volume elements and initial parameter values are specified by a user. A sample

(a) Outer wall (a) Inner wall

Figure 10.4: Boundary data sets

configuration file is shown in Table 10.1[3]. The simple volumetric model (e.g., a volumetric ellipsoid) is assembled as described in Section 6.5 and then placed at the center of inertial frame.

10.2.1 Fitting Procedure

Once the boundary and SPAMM data at end diastole (this is the undeformed state of the LV) are loaded, we may proceed with the fitting process. For efficient and effective model fitting, we come up with the following fitting schedule:

1. Estimate the orientation of the model frame based on the boundary data at the initial time, i. e., end-diastole. The model frame is first translated to the center of mass of the data points. The forces from the data points acting on the model will cause it to translate and to rotate to find a suitable position and orientation. Since the initial model is symmetric about its long axis, sometimes the final orientation is not suitable. The model has markers to indicate where the septum should be, as shown in red dots in Fig. 10.5[4], so that we can adjust the orientation by rotating the model about its long axis, for correct interpretation of the parameter variations. The initial model has constant parameter functions; in particular, $a_1(\mathbf{u}) = c_1$, $a_2(\mathbf{u}) = c_2$,

[3]Note that the initial values for the deformation parameters (e.g., τ) which are not shown in the configuration file are initially set to 0.

[4]The inertial frame of reference and the model frame are displayed on the left and at the center of the canvas, respectively. White dot markers are places on the model in order to locate the septum area of the heart in image data, and therefore aid in placing the model in a suitable orientation.

```
% Model type (ellipsoid 0, superquadric 1, cylinder 2)
0

% Dimension (usize, vsize, wsize, uportion, vdivision, num of poles)
10    16    3    0.75    4    1

% Initial w (inner outer)
1.0    1.5

% Initial parameter values (a1, a2, a3)
0.5    0.5    0.5

% Squareness parameters for a superquadric (e1, e2)
1.0    1.0

% Euler step
0.00001

% Translation (x, y, z)
0.0    0.0    0.0

% Orientation (flag=0, q.w, q.x, q.y, q.z; flag=1 angle, axis x,y,z)
1    90.0    1.0    0.0    0.0

% Boundary and SPAMM data filenames (number of time, normalizing factor)
5    50.0
data/lv1/boundary1.pts    data/lv1/tagged-1
data/lv1/boundary2.pts    data/lv1/tagged-2
data/lv1/boundary3.pts    data/lv1/tagged-3
data/lv1/boundary4.pts    data/lv1/tagged-4
data/lv1/boundary5.pts    data/lv1/tagged-5
```

Table 10.1: A sample configuration file : lv.config

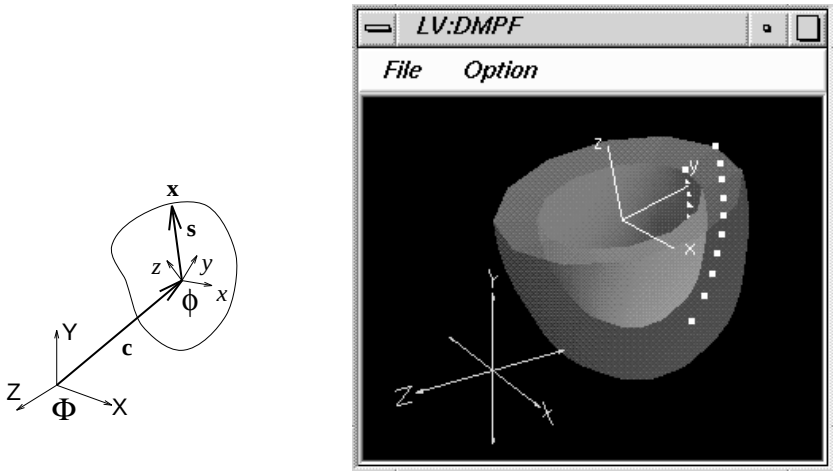

(a) (b)

Figure 10.5: Computer implementation (program main panel)

$a_3(\mathbf{u}) = c_3$ and $\tau(\mathbf{u}) = 0$, where $0 < c_1, c_2, c_3 < 1$, for all $\mathbf{u} = (u, v, w)$. While finding its optimal location for the model center in the reference frame, c_1, c_2 and c_3 are also estimated. Fig. 10.6(a) shows that the model which is shown in white mesh is pulled at the centroid of inner and outer boundary data points (darker gray dots are the outer boundary data).

2. Then based on the computation of boundary forces (as described in Section 7.3.1) the nodes on the inner and outer walls of the model are pulled towards the inner and outer boundary data points, respectively. We first estimate the value of the material coordinate w for the inner (w_{in}) and outer (w_{out}) walls at this stage. Fig. 10.6(b) shows the model at the end of this step.

   If the volumetric model is tessellated across the walls as well (i.e., wsize$>$ 2), as shown in Fig. 6.5), the material coordinate w_i for each layer is computed from the values of w_{in} and w_{out}. For example, w value of mid-wall is computed as follows:

$$w_{mid} = \frac{w_{out} - w_{in}}{2}.$$

3. Once the fitting of the model in the first step is completed and we have estimated w for the inner and outer walls, the a_1, a_2 and a_3 parameters are allowed to vary with respect to w only, so that we can recover the wall thickness more accurately. See Fig. 10.6(c).

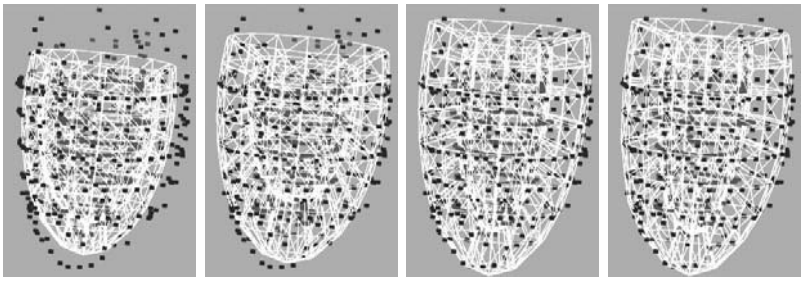

(a) (b) (c) (d)

Figure 10.6: Initial shape recovery

4. Finally, the parameters are allowed to vary also in u to estimate the non-symmetrical shape of the LV. We first estimate the parameter functions $a_1(u, w)$, $a_2(u, w)$ and $a_3(u, w)$. Note that the twist parameter τ is activated when the data points from next time frame (time 2) are loaded. See Fig. 10.6(d).

5. After the model fits the initial boundary data at end-diastole (ED), we use it to fit data from subsequent time frames till end-systole (ES). We first read in the SPAMM data points at ED in order to register the locations of SPAMM data points which coincide with material points. For each SPAMM data point, we find the volume element which encloses the data point (as described in Table 7.2), and compute its relative location on the model with respect to the enclosed volume element (as described in Section 7.3.2). The purpose of this step to "mark" the material points, which corresponds to the SPAMM data points, on the model. Note that once we compute r and $\mathbf{m}$ as previously described, we can always locate the material point regardless of how the volume element is deformed.

6. The boundary and SPAMM data points at the next time frame (e.g., $t = 2$) are loaded onto the previously fitted model (e.g., $t = 1$). Based on the distance between these data points and the mode we compute a new set of forces. Based on these forces we first estimate the rigid motion using boundary data points before estimating the deformation of the model.

7. The model deforms due to the SPAMM data forces computed within the volume element as described in Section 7.3.2. The combination of forces from the SPAMM data points in two orthogonal sets allow us to recover the deformation of the model

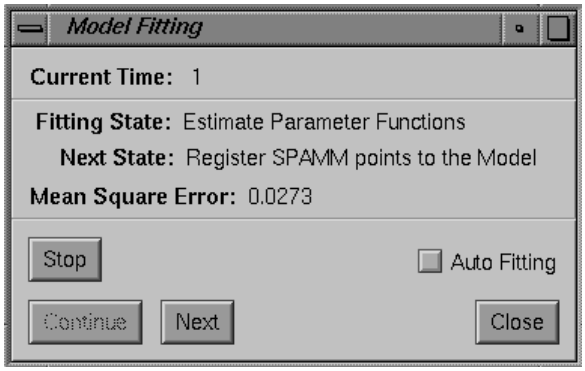

Figure 10.7: Fitting scheduler

in all three components, effectively recovering the missing through-plane motion.

8. When all applied forces equilibrate or vanish, the model comes to rest. Then, the SPAMM data points at $t = 3$ are loaded onto the fitted model of $t = 2$. And we repeat steps 6 and 7 for up to end-systole. The deformation from ED to ES is captured in the parameter functions.

The fitting stage is displayed on and controlled from the <Model Fitting> panel of the computer program as shown in Fig. 10.7. By simply clicking on <Next> button, one can walk through each fitting process. The <Auto Fitting> check-box allows to automate the fitting process, so that when the error of fit (the distance between a data point and the model surface) falls within an acceptable tolerance specified by the user, each fitting step will roll over to the following fitting step based on the scheduler. Note that the fitting process for each time frame takes approximately 45 seconds on a Silicon Graphics R4400 Indigo workstation.

10.2.2 Flow Chart

Going back to the diagram in Section 4.4, the fitting procedure in previous section covers the main block in Fig. 4.5. The Fig. 10.8 shows the overall flow chart of the proposed method for LV motion analysis. The blocks B1 and B2 in Fig. 10.8 correspond to the preparation steps (the first two blocks in Fig. 4.5). The initial shape recovery steps (Steps #1–#4 from the previous section) is the block b31. The blocks b32, b41 and b42 correspond to Step #5, #6 and #7, respectively. The block B5 will be discussed in the next chapter.

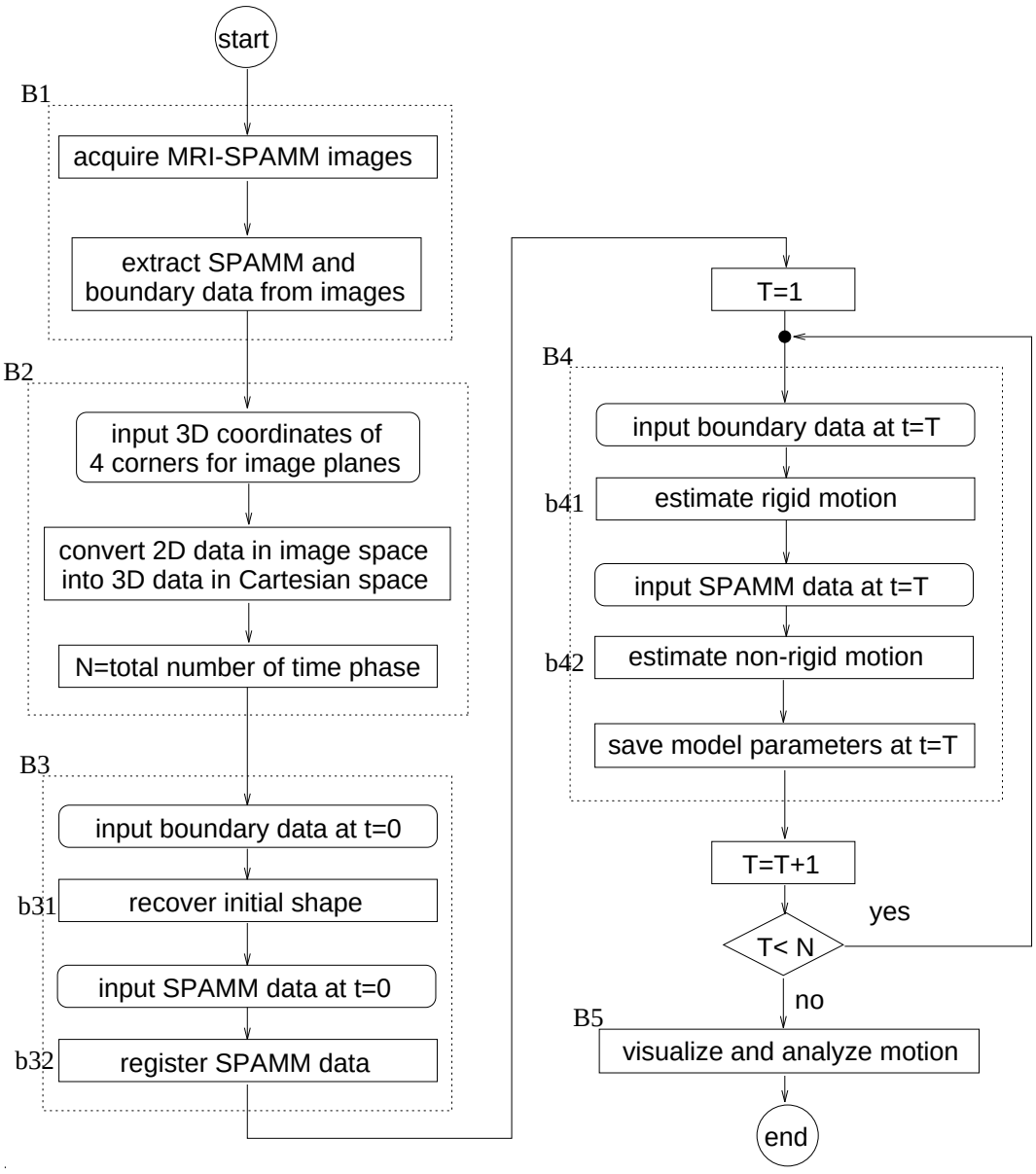

Figure 10.8: Flow chart of the proposed apparatus for LV motion studies

10.3 Experimental Results (Normal LV)

The combination of computed forces from the SPAMM data points from two orthogonal planes allows us to recover the deformation of the model in 3D. Fig. 10.9 shows model fitting results for a normal LV over 5 time frames from end-diastole (ED) to end-systole (ES). The top row shows a view from the base of the LV of the fitted model. The twisting of the inner wall (shown in white) is obvious. The middle row shows a side view of the model, while the last row is similar to the first row and shows a view of the model from the apex. We can easily observe the longitudinal contraction as well as the radial contraction.

Fig. 10.10 shows the fitted model superimposed to the SPAMM data points over 5 time frames. SPAMM data points are denoted with black dots, while the corresponding model material points are denoted with white dots. Initially, the SPAMM data points coincide with the material points on the model (therefore, only black dots are shown in the Fig. 10.10(a)). The first two rows show the model with superimposed short-axis SPAMM data points (Fig. 10.3(a)), and long-axis SPAMM data points (Fig. 10.3(b)), respectively. The last row shows both sets of SPAMM data points. We can observe that the material points move in 3D space, thus recovering the through-plane motion, while the image planes (where black dots are located in Fig. 10.10) are stationary.

10.4 Recovery of Through-Plane Motion

Fig. 10.11 shows a top portion of the model from end diastole (ED) to end systole (ES). The red dots (darker gray dots in non-color print) on the model at ED indicate the SPAMM data points[5] at end-diastole, which coincide with the corresponding material points. The yellow dots (lighter gray dots on the same image plane) on the model in subsequent time are the SPAMM data points. The motion paths of SPAMM points over time are shown in green (darker gray lines). The light blue dots (gray dots off the image plane) are the corresponding material points at each time. The motion paths of the material points during systole are shown in white. Notice that at every instant the projection of the material point location on the image plane approximately coincides with the location of the SPAMM data

[5]It is a subset of SPAMM data points from a short-axis view image plane.

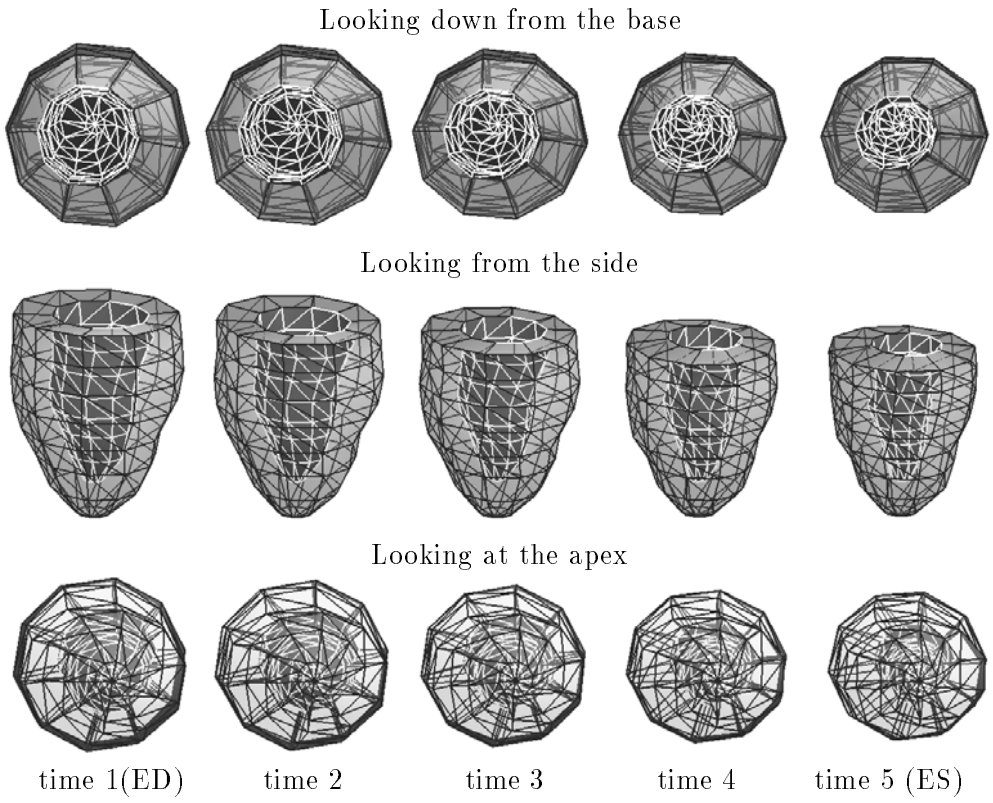

Figure 10.9: Fitted models during systole

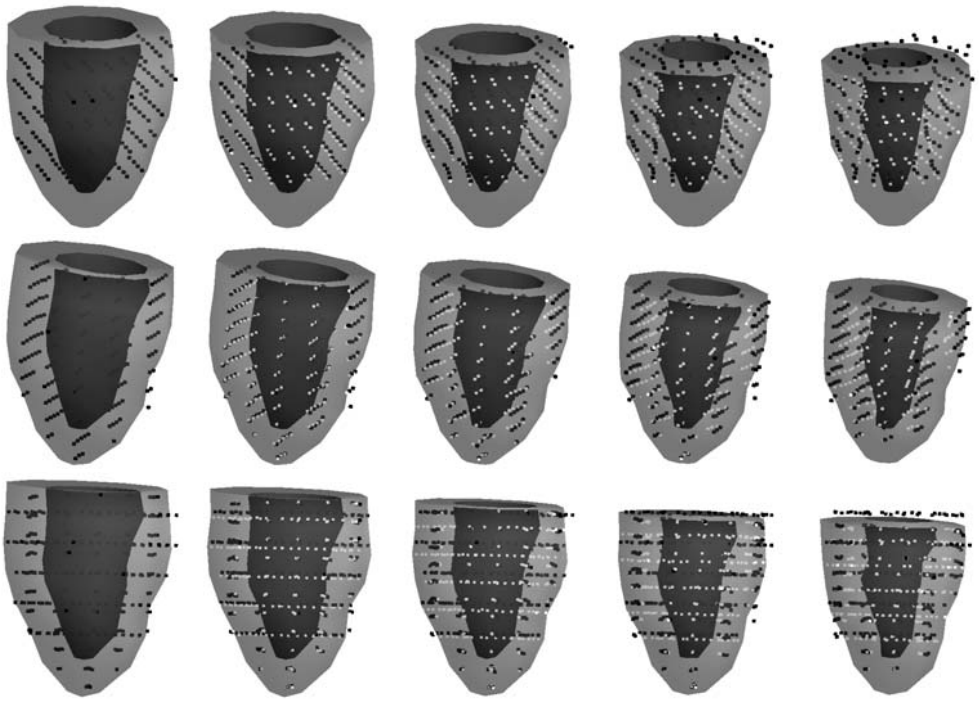

(a) time 1 (ED) (b) time 2 (c) time 3 (d) time 4 (d) time 5 (ES)

Figure 10.10: Fitted models during systole with SPAMM data points and material points

point. We can clearly see that the material points are moved in 3D, while the SPAMM data points provide only in-plane motion.

10.5 Normal vs. Abnormal

In the following experiments we present our LV shape and motion analysis results from MRI-SPAMM for normal and abnormal LVs with hypertrophic cardiomyopathy (**htcm**).

Fig. 10.12 shows two fitted models to LV data sets from (a) a healthy volunteer and (b) a patient with hypertrophic cardiomyopathy. We can observe 3D deformation – radial contraction, longitudinal contraction, twisting and bending – of each LV during systole. We have found that the abnormal heart does not contract as much as the normal heart (especially towards the apex), but twists more, and has a bigger long axis deformation[75, 78].

The advantage of having our model is that these deformations can be described with

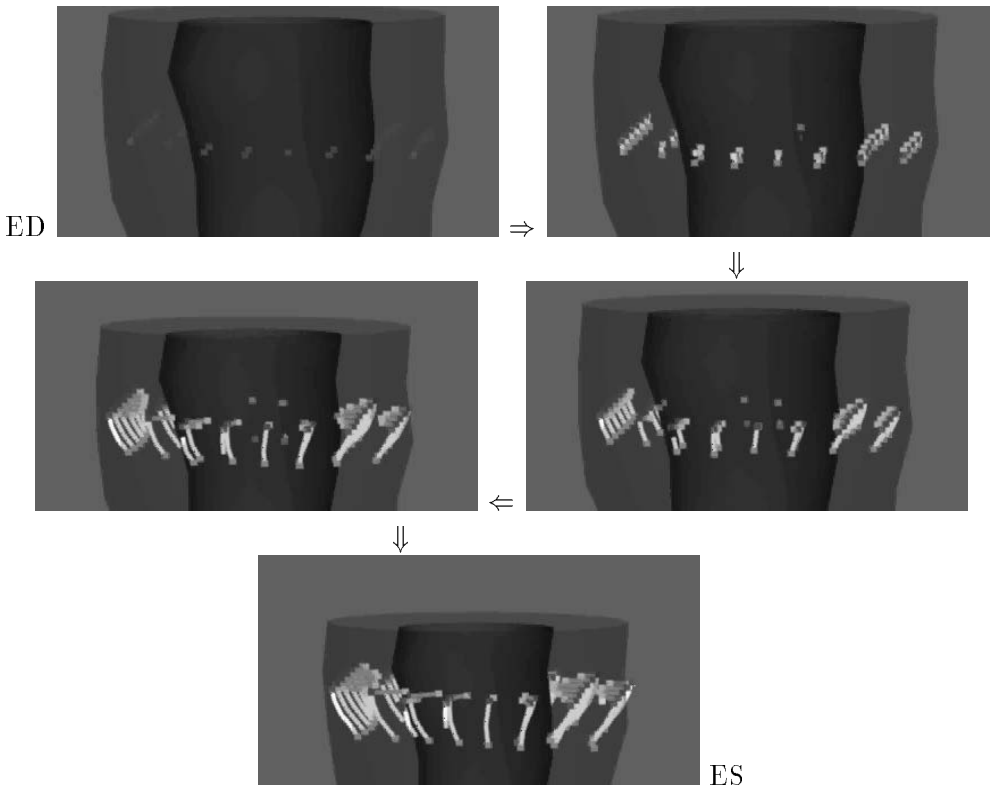

Figure 10.11: Motion paths of SPAMM points and corresponding material points during systole

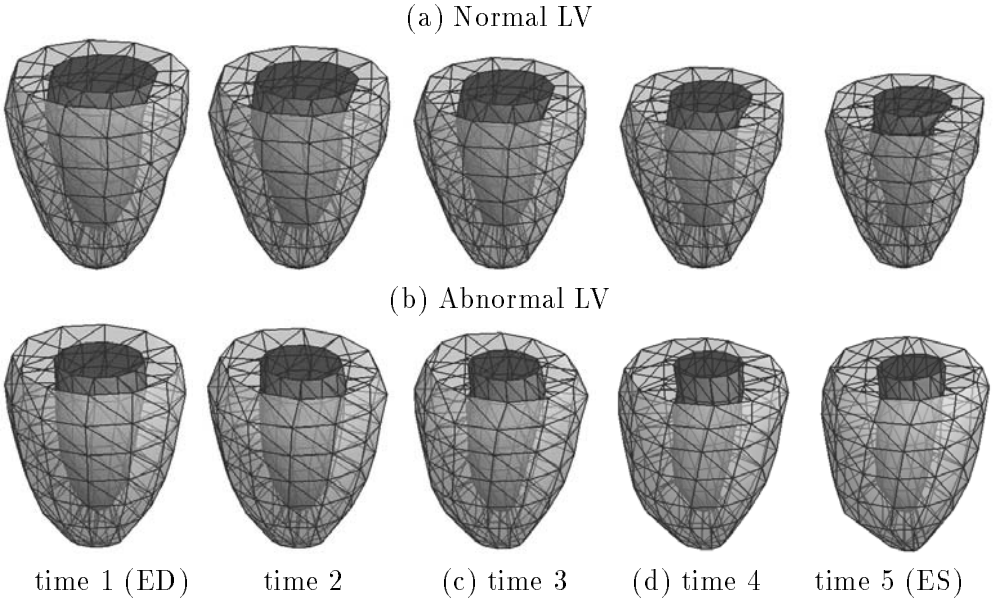

Figure 10.12: Fitted models during systole

the model parameter functions which comprise an intelligent grouping of the many local parameters that are necessary to analyze the LV motion into a small number of sets. Based on these parameter functions, we can perform a quantitative analysis of the motion.

Fig. 10.13 shows graphs of the extracted model parameters as functions of u (i.e., varying along the long axis of the LV) at the inner and outer walls. In general, the contraction and the twisting deformation are more significant on the inner LV wall (Figs. 10.13(g-j)) compared to the outer wall (Figs. 10.13(a-d)). The difference in the corresponding parameter values is obvious. The graphs allow us to quantify the motion and shape changes of the LV during systole. For example, by studying the graphs in Figs. 10.13(a,b), we can conclude that the overall percent changes of the magnitude of radial contraction of the outer wall during systole is approximately $15 - 20\%$. However, towards the base of the LV the contraction along the y axis (it is approximately 10% from Fig. 10.13(b)) is less than the contraction along the x axis (it is approximately 17% from Fig. 10.13(a)) making the base look more elliptical. From Fig. 10.13(d) we can quantify the twisting motion of the outer wall during systole to approximately 14 degrees total from base to apex. The graph shows a small amount of global rotation before the twisting occurs.[6] It is not easy

[6]Compare the changes in the parameter values in Figs. 10.13(d,j) from time 1 to time 2 with the changes from time 2 to time 3.

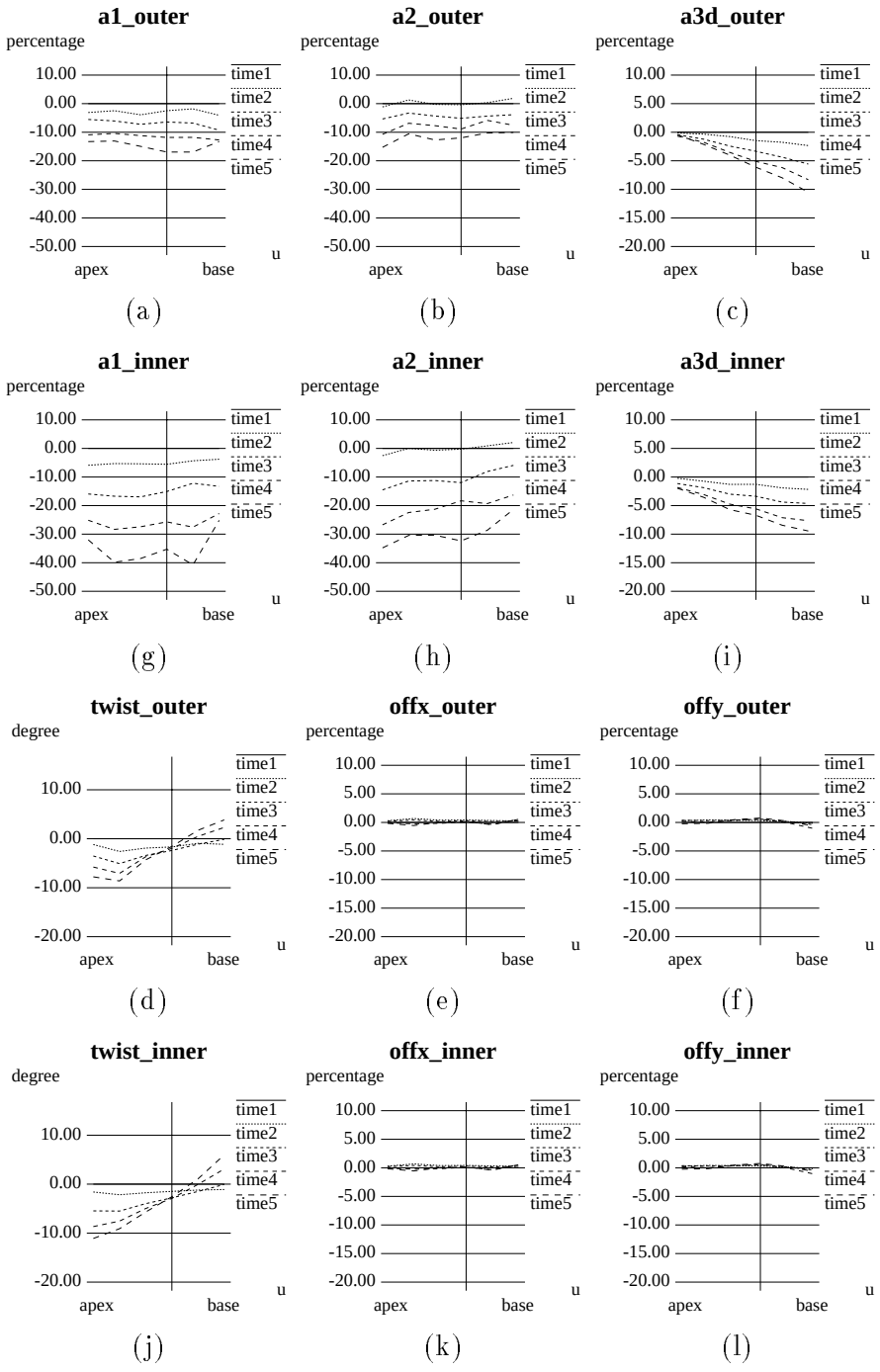

Figure 10.13: Extracted model parameters as functions of u (normal LV)

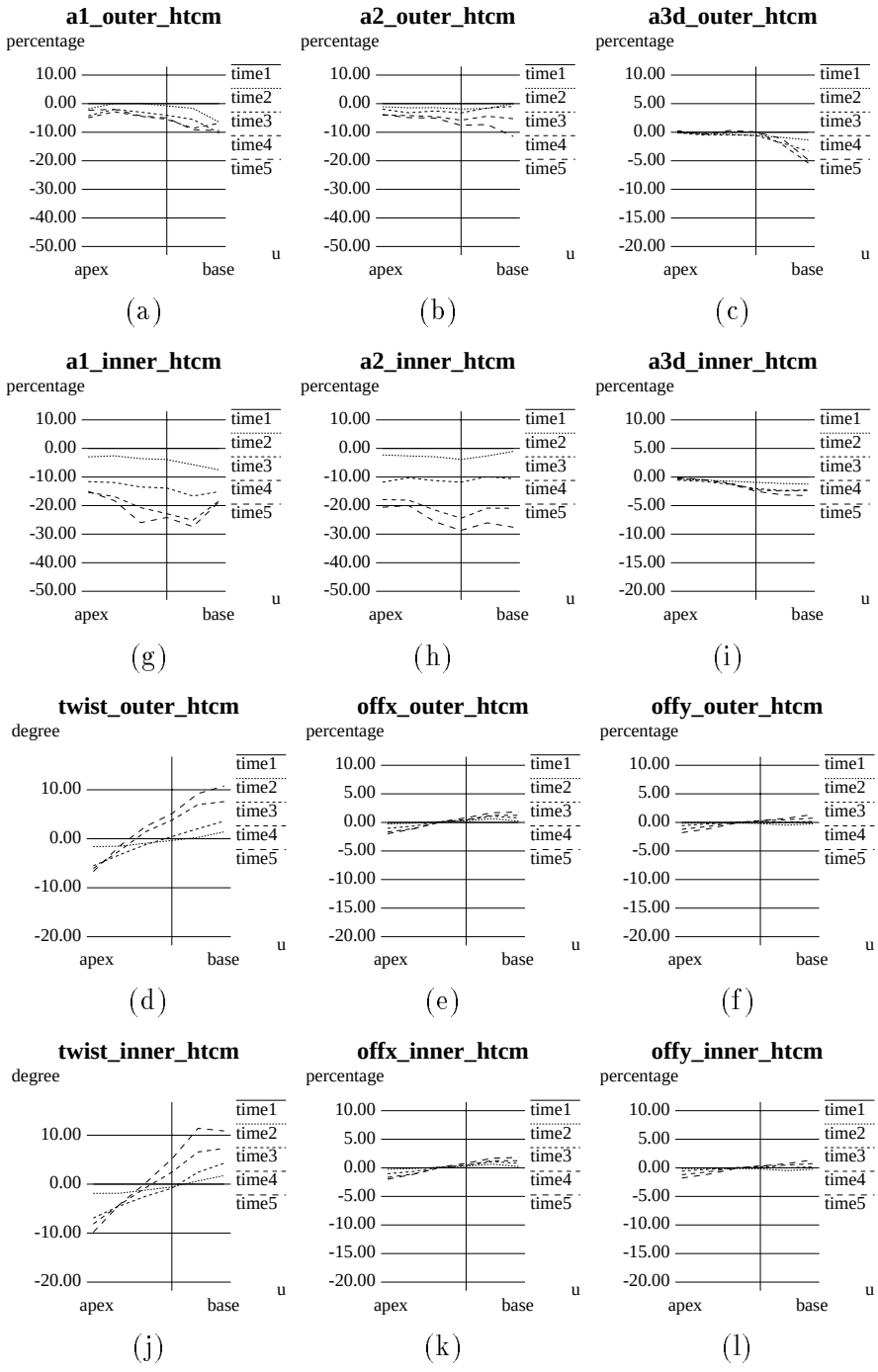

Figure 10.14: Extracted model parameters as functions of u (abnormal LV)

to see this kind of subtle motion when one watches the model contract and twist on the monitor. Figs. 10.13(e, f, k, l) show the estimation results for the long axis deformation, which represent small changes and are not significant. By having the graphs of the parameter functions plotted in conjunction with the animation, we can quantify and easily characterize the detailed motion of the deforming model over time.

In Fig. 10.14 we show fitting results to SPAMM data from an abnormal LV with hypertrophic cardiomyopathy (**htcm**). By comparing the corresponding graphs we can observe that the abnormal heart does not contract as much as the normal heart (especially towards the apex), but twists more, and has a bigger long axis deformation. This latter deformation corresponds to a spatial bending of the LV.

Based on Gauss's theorem (see Section 8.3.1), we also calculated the volume of the blood pool over time to compute ejection-fraction. The ejection-fraction of the normal LV was $61 \pm 5\%$, while for the abnormal it was $52 \pm 8\%$.

10.6 Comparisons with Clinical Data

We have compiled from literatures the clinical findings regarding the left ventricular wall motion. Palmon *et al.* [73] reported the results on intramural myocardial shortening and the mid-wall long-axis shortening from 2D analyses based on tagged MR images. They compared the data from normal subjects with the data from the patients of hypertensive left ventricular hypertrophy. Young *et al.* [115] also reported extensive strain analyses, based on 3D finite element models, where the data from normal subjects and the data from patients with hypertrophic cardiomyopathy. In their studies, the measure of torsion was reported as well as the radial and longitudinal contractions.

The comparisons between their findings and our results in Fig. 10.13 and Fig. 10.14 are summarized in Table 10.2, Table 10.3, and Table 10.4. It is very encouraging that the results obtained from the proposed models agree with the clinical findings previously reported. One limitation with our model is that we were not able to capture the regional differences between anterior, lateral, septal and posterior sites due to the fact that the parameters for radial contraction do not vary circumferentially. (We marked a question

mark (?) at the respective entries in the tables.) In the future studies, we plan to allow such variations by combing $a_1(u, w)$ and $a_2(u, w)$ parameters into one parameter, namely $\alpha(u, v, w)$, as defined in equation (8.2) and described in Section 8.2.1. There were no clinical data available for us to compare our regional twist variations at the fine level.

Short-Axis Deformation :

source	Results reported in the literature	Our Results	Agreed?
[73]	The average circumferential shortening (CS) in the normal subjects at the endocardium was $44 \pm 6\%$.	Fig. 10.13(g)	$\surd$
[73]	The average CS in the normal subjects at the epicardium was $21 \pm 5\%$.	Fig. 10.13(a)	$\surd$
[73]	The average CS in the hypertensive subjects (**htcm** patients) at the endocardium was $29 \pm 6\%$.	Fig. 10.14(g)	$\surd$
[73]	The average CS in **htcm** patients at the epicardium was $13 \pm 5\%$.	Fig. 10.14(a)	$\surd$
[73]	The transmural gradient in percent shortening from endocardium to epicardium in both normal subjects and **htcm** patients were the same: The endocardial shortening exceeds the epicardial shortening by 2:1 ratio.	Fig. 10.13(a),(g), Fig. 10.14(a),(g)	$\surd$
[73]	In normal subjects, no regional differences in the CS were observed between anterior, lateral, septal, and inferoposterior sites. But in **htcm** patients, the CS were not uniform (significantly higher at the lateral wall sites).	?	?
[73]	In normal subjects, a base-to-apex gradient in the CS was observed (with greater apical shortening).	Fig. 10.13(h)	$\surd$
[73]	No significant base-to-apex gradient was found in **htcm** patients.	Fig. 10.14(h)	$*$

$*$ We see a reverse base-to-apex gradient in **htcm** patients.

Table 10.2: Comparisons with clinical data: Circumferential shortening

Long-Axis Deformation :

source	Results reported in the literature	Our Results	Agreed?
[73]	The longtudinal shortening (LS) was uniformly depressed in **htcm** patients compare to that in normal subjects.	Fig. 10.13(c),(i), Fig. 10.14(c),(i)	$\surd$
[73]	The septal LS across the wall showed no difference at the endocardium, midwall and epicardium for both groups.	Fig. 10.13(c),(i), Fig. 10.14(c),(i)	$\surd ?\star$
[73]	In the free wall, LS was higher at the endocardial sites for both groups.	?	?
[115]	The logitudinal displacement (LD) of the base toward the apex was markedly reduced in **htcm** patients.	Fig. 10.13(c),(i), Fig. 10.14(c),(i)	$\surd$
[115]	The LDs in normal subjects were $1.8 \pm 0.8mm$ at the apex, $7.0 \pm 1.1mm$ at the mid-ventricle and $12.5 \pm 2.0mm$ at the base.	Fig. 10.13(c),(i)	$\surd$
[115]	The LDs in **htcm** patients were $1.2 \pm 0.5mm$ at the apex, $4.0 \pm 0.6mm$ at the mid-ventricle and $7.5 \pm 2.5mm$ at the base.	Fig. 10.14(i)	$\surd$

$\star$ We see no difference in normal subjects, but some differences in **htcm** patients.

Table 10.3: Comparisons with clinical data: Longitudinal displacement

Twist (Torsion) :

source	Results reported in the literature	Our Results	Agreed?
[115]	The LV torsion (twist of the apex about long axis relative to the base) was increased in **htcm** patients.	Fig. 10.13(d),(j), Fig. 10.14(d),(j)	√
[115]	The torsion in normal subjects was $14.6 \pm 2.7°$ at the mid-wall.	Fig. 10.13(d),(j)	√
[115]	The torsion in **htcm** patients was $19.9 \pm 2.4°$ at the mid-wall.	Fig. 10.14(d),(j)	√
[115]	The angle of rotation about the central axis was greatest at the apex for both groups.	Fig. 10.13(d),(j)	√ ×
[115]	The angle of rotation was counter-clockwise at the apex, and clockwise at the base for both groups.	Fig. 10.13(d),(j), Fig. 10.14(d),(j)	√ √
[115]	The rotation magnitude was higher at the endocardium than that at the epicardium for both groups.	Fig. 10.13(d),(j), Fig. 10.14(d),(j)	√ √
[115]	In normal subjects, the apical and basal rotations at epicardium were $10 \pm 4°$ and $1 \pm 1°$, respectively; and at endocardium were $14 \pm 3°$ and $2 \pm 2°$, respectively.	Fig. 10.13(d),(j)	√
[115]	In **htcm** patients, the apical and basal rotations at epicardium were $14 \pm 4°$ and $3 \pm 3°$, respectively; and at endocardium were $16 \pm 6°$ and $4 \pm 4°$ in **htcm** patients.	Fig. 10.14(d),(j)	×

× The greater rotation in **htcm** patients was at the base, not at the apex.

Table 10.4: Comparisons with clinical data: Twist

Chapter 11

Visualization

In this chapter, we emphasize the visualization techniques based on the implementation of dmpf which utilizes the OpenGL^{TM} graphics library and the OSF/Motif^{TM} user interface in order to create a user-friendly and interactive program for visualizing and manipulating three-dimensional objects. Note that a virtual track ball or an arc-ball [93] is implemented for a convenient viewing manipulation. Furthermore, utilizing alpha source blending functions in GL, a user may make certain layers of the model transparent for an easier observation.

11.1 Parameter Value

The program allows to view (and to adjust if necessary) values of each individual parameter function at any location of the model through the <Parameter Functions> panel as shown in Fig. 11.1. When the <show nodes> check-box is checked, the selected location of the model will be highlighted for easier referencing.

11.2 Parameter Graphs

As demonstrated in Section 10.5, the main advantage of the proposed technique over other techniques for modeling LV is that the shape and motion of the model can be completely described by the global parameter functions which do not require a complex post-processing.

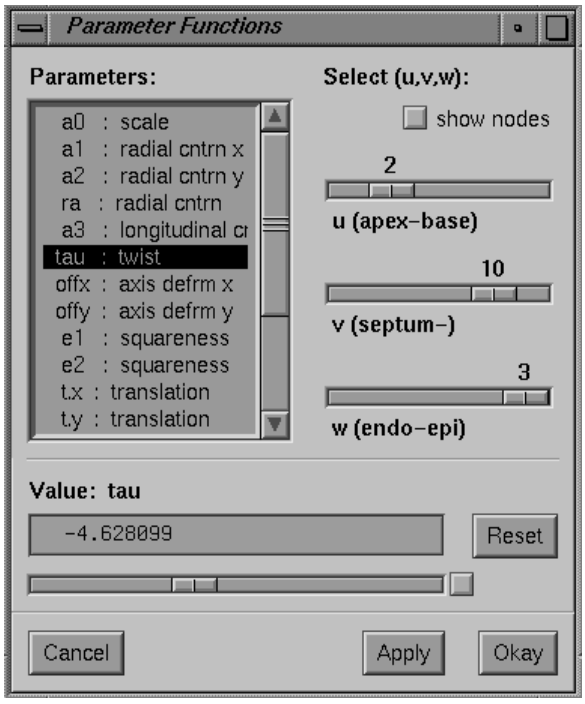

Figure 11.1: Panel: parameter functions

Since the semantics of each of the model parameters are intuitive, we can directly plot each parameter function for comparison purposes and visualization. For example, since u varies from the apex to the base of an LV (Fig. 8.1(b)), by plotting extracted parameters as functions of u we can compare and quantify the motion variation from the apex to the base. Fig. 11.2(a) shows plots of a_2 parameter (which captures radial contraction along the constrained direction) at the endocardium (w_{in}) for each time phase ($t = 1 \cdots 5$) where "time5" refers to end-systole. We can quantify that the overall percent changes of the magnitude of radial contraction of the inner wall during systole is approximately 30%, and the contractions at the apex and at the base are approximately 35% and 22%, respectively. By plotting the parameter for each time phase, we can observe the progression of the deformation during systole. Fig. 11.2(b) shows parameter τ (which captures twisting about the long axis of the LV) at the endocardium for each time phase as in (a). The graph shows a small amount of global rotation before the twisting occurs. Compare the changes in the parameter values from $t = 1$ to $t = 2$ with the changes from $t = 2$ to $t = 3$. It is not easy to see this kind of subtle motion when one watches the model contract and twist on the monitor, yet we are able to observe it through the use of the parameter graphs.

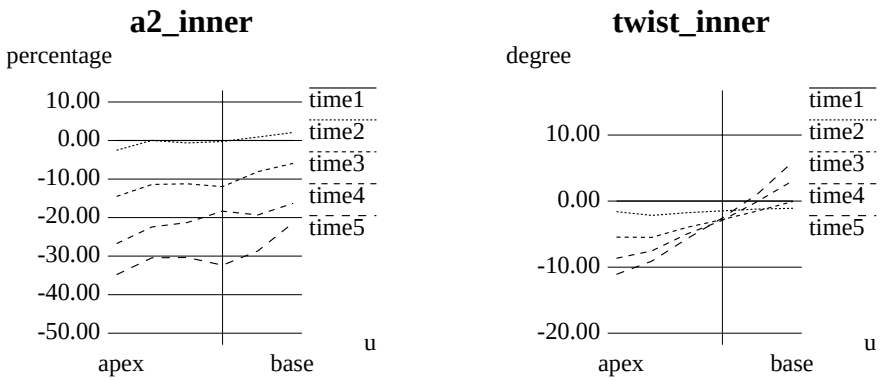

(a) Radial contraction (b) Twisting

Figure 11.2: Extracted model parameters as functions of u (normal LV).

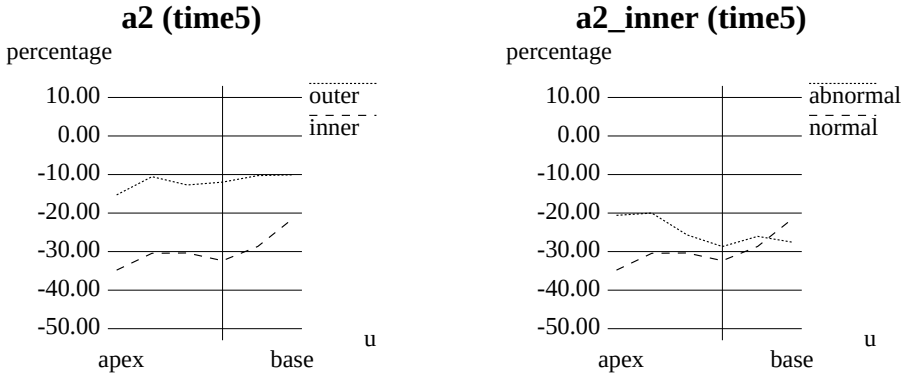

(a) Endocardium vs. Epicardium (Normal)

(b) Normal vs. Abnormal (Endocardium)

Figure 11.3: Radial contraction at end-systole

Fig. 11.3(a) shows parameter a_2 estimated at the inner and outer walls of the normal LV at end-systole. We can observe that the contraction at the endocardium is much greater compared with the contraction at the epicardium (which is approximately 12%). We may also plot the graphs for both the normal and the abnormal heart for comparison purposes. Fig. 11.3(b) shows the same parameter function at the endocardium, at end-systole. We can observe that the abnormal LV does not contract as much as the normal LV does, especially towards the apex. The abnormal LV contracts only approximately 60% of the amount for the normal LV.[1] For a complete list of graphs of other parameters, please refer to [75].

[1] 20/35

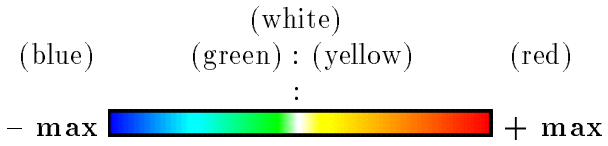

Figure 11.4: Color scales

```
for each node
        evaluate the VALUE for the selected parameter
        initial color triplet is set to (1.0, 1.0, 1.0)
        if VALUE is positive
                RATE = VALUE/MAX
                color triplet is set to (RATE, 1.0–RATE, 0.0)
        if VALUE is negative
                RATE = –VALUE/MAX
                color triplet is set to (0.0, 1.0–RATE, RATE)
```

Figure 11.5: Color mapping algorithm

11.3 Color Mapping

The parameter graphs provide an overall analysis of the LV motion. In order to visualize and localize the behavior of motion, we employ a color-coding scheme where the maximum variations are in red and blue as shown in Fig. 11.4. The undeformed state is depicted in white, positive deformation (e.g., dilation, clockwise twisting, bending in a positive axis direction) varies from yellow to red, and negative deformation (e.g., contraction, counter-clockwise twisting, bending in a negative axis direction) varies from green to blue.

For each parameter function, its value is evaluated at each node of the model. Then the value is used to compute a triplet for the corresponding hue (as given in Fig. 11.5), which is then used to render the model.

Fig. 11.6 shows such renderings of the model for parameter τ estimated for the normal LV during systole. White, red and blue correspond to zero twist, $+10$ degree twist and -10 degree twist, respectively. We can clearly observe that the LV has undergone a wringing motion during systole. While we observe progressive counter-clockwise twist at the apex

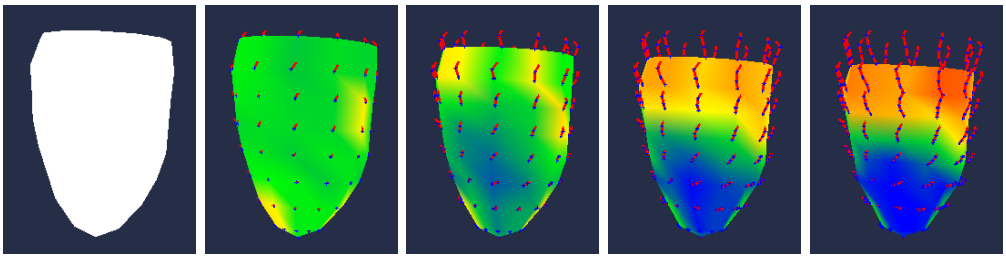

time 1 (ED) time 2 time 3 time 4 time 5 (ES)

Figure 11.6: Twist parameter (normal LV)

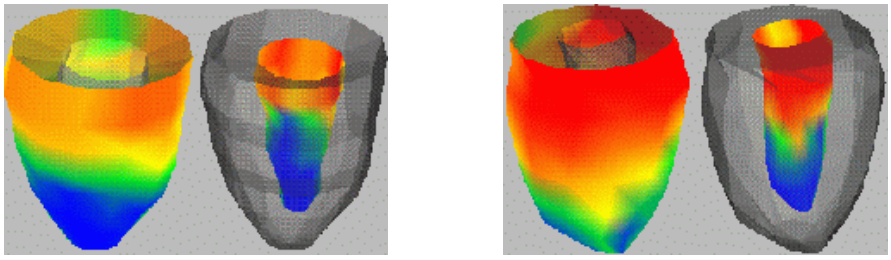

(a) (b)

Figure 11.7: Twist parameter at ED (normal vs. abnormal)

(white → green → light blue → blue), we observe a small amount of counter-clockwise twist initially and then clockwise twist (white → green → yellow → orange) at the base of the LV. The traces of the positions of nodes over time are drawn in red lines and blue dots in the figure as well.

Fig. 11.7 illustrates the twisting motion on the inner and outer walls at end-systole for the normal and the abnormal LVs. For both LVs, we can easily observe that the inner wall twists more than the outer wall does (i.e., we see more red-ness and blue-ness on the inner walls). It also becomes clear that the abnormal LV twists more and its twisting motion is more non-uniform.

The visualization program also allows users to look at the cross sections of the model. Fig. 11.8 shows two short axis views (A and B) and one long axis view (C) of both normal and abnormal LVs at end-systole. Note that we can also observe that both LVs twist more towards the free-wall (negative y direction).

Fig. 11.9(a) shows the loci of the nodes of the model fitted to a normal heart data from ED to ES. The meshes represent the model at ED and the shaded outer surface (according

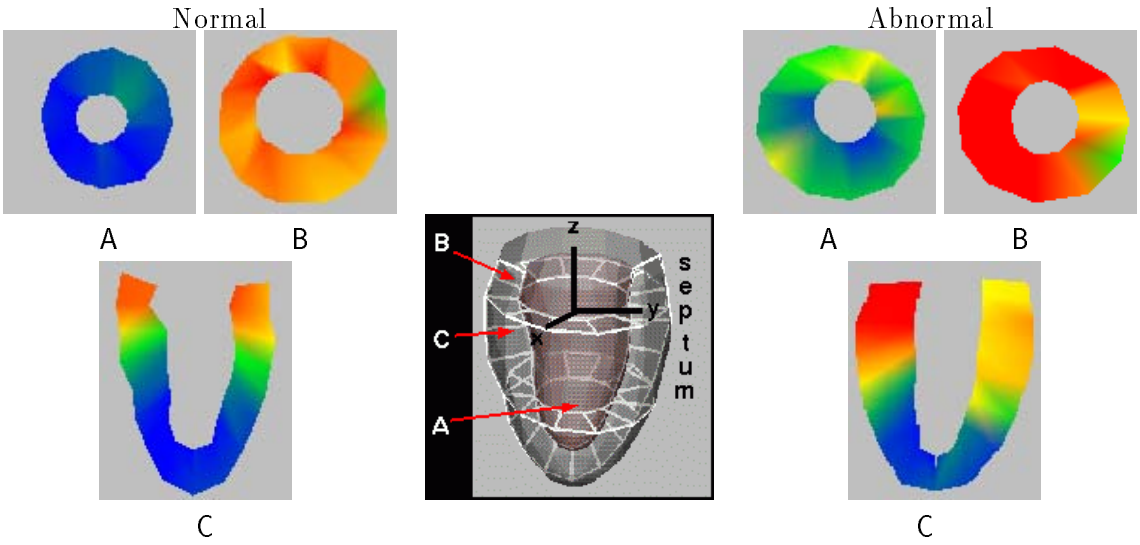

Figure 11.8: Twist parameter (cross sections)

to the twist parameter function) is the model at ES. Fig. 11.9(b) is the same figure as (a) except that the model at ED is not overlaid. The white dots are the node positions at each time frame during systole. Fig. 11.9(c) also shows the loci of the nodes of the outer surface of the model fitted to an abnormal heart data over its systole. The wringing motion of the left ventricles are quite apparent in these figures.

A user can choose any other parameter function for visualization based on the color mapping to the model. If requested, we can also plot and use color mapping techniques to visualize the LV strains, given that we know the 3D location of every point on the model.

11.4 Summary

We have presented a comprehensive model-based approach for visualizing the shape and nonrigid motion of the left ventricle (LV) during systole. Our visualization methods used the set of extracted model parameters and the recovered 3D LV model and its motion during systole. Based on our visualization tools we showed that it is possible to visualize aspects of the complex LV motion that were not possible previously. In addition, we have presented in a clinically useful way our analysis results and were able to compare normal and abnormal hearts.

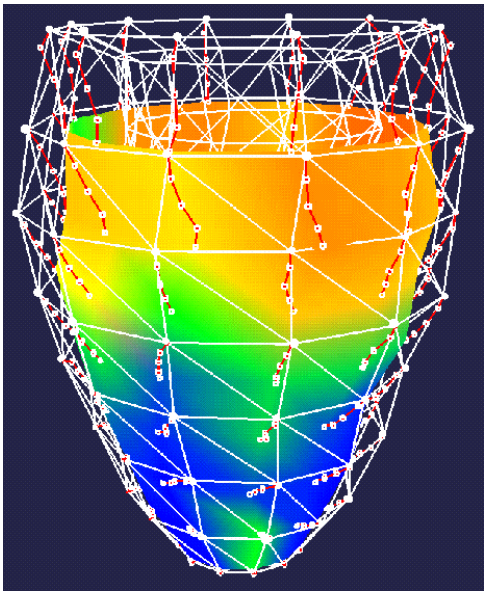

(a) Normal LV (meshes:ED, shaded:ES)

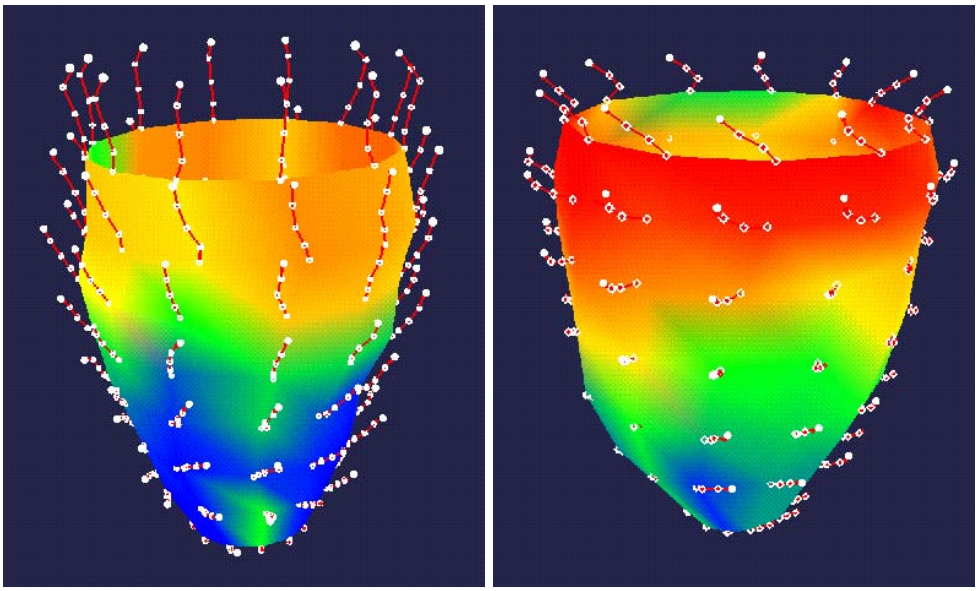

(b) Normal (c) Abnormal

Figure 11.9: Motion paths of nodes

Chapter 12

Validation

We have performed the following experiments with a deformable gel phantom in order to verify the accuracy and reliability of the proposed shape and motion estimation technique:

1. **Reproducibility :** Run several experiments on the same data set to measure the sensitivity of the initial orientation and the dimensions of the model, and the fitting scheduler.

2. **Fitting error measurement :** Project each material point of the model at the deformed state onto the image plane, where its corresponding SPAMM data point is located, in order to get a visual idea of the magnitude of the errors.

3. **Comparison with physical data :** Compare the wall thickening measure from the proposed model to the value obtained from actual measurement.

12.1 Gel Phantom Data

12.1.1 Gel Phantom Description

We have used one of the phantoms created by Daniel Bloomgarden in the Radiology Department at the University of Pennsylvania. The phantoms were built from silicone gel material that was molded into cylinders of varying radii. The silicone gel material has been utilized in phantom studies [24] since; 1) it has high signal intensity and long T1 times

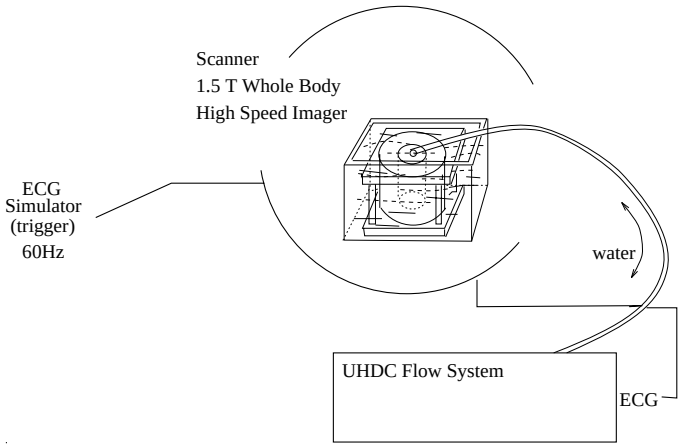

Figure 12.1: Gel experiment setup

in MR imaging, 2) its elastic material properties can be controlled by the mixture of its constituent parts, and 3) it can be molded into any desired shape. There are two liquid components (Dow Corning) – the resin (part A) and the catalyst (part B) – for the gel. When these two components are combined in any ratio A:B ranging from 1:3 to 3:1, they solidify into a homogeneous gel. The ratio determines its elastic properties.[1]

For the study presented in this chapter, we used the thick walled cylindrical gel phantom which was molded from the mixture of part A and part B with the ratio of 1:1.5. Its approximate dimensions are: 20 mm inner diameter, 62 mm outer diameter, and 68 mm height.

12.1.2 Experimental Setup and Imaging Protocols

The gel was placed between two lucite plates (see Fig. 12.1). The top plate had a hole in the center through which we can attach the tube where we can pour water in and out to deform the gel. The tube was attached to a computer driven piston pump (UHDC) which was programmed to pump forward at a specified rate for 800 $msec$, pause during imaging (500 $msec$), then withdraw at a slower rate (2 seconds). The same amount of fluid was pumped out. Prior to the attachment of the tube to the phantom, the phantom cavity was filled with water and the phantom was also immersed in water to eliminate any pressure differences within the cavity due to a hydrostatic pressure.

[1] An increase in the ratio A:B produces a stiffer gel.

The gel was imaged using a single shot gradient-echo pulse sequence with SPAMM MR tagging. Each image slice has 256×256 dimensions with 10 mm thickness. The SPAMM stripes were separated by 6.5 pixels = 4.0625 mm and were angled at 45 degree to the horizontal dimension in order to obtain equivalent stripe resolution in all directions. 2 long axis images (1 axial, 1 sagittal), and for 3 short axis images (coronal) were obtained at 20 ml/sec flow rate for 2 time phases – one at resting (time 1), and the other at the maximum flow rate (time 2). The imaging timing was synchronized with the pumping based on the ECG simulator connected to the setup.

Figs. 12.2(a-b) show long axis and short axis images at two time instances. The SPAMM data points and boundary data points are extracted using SPAMMVU as described in Section 4.2.3. The radial expansion is apparent from Fig. 12.2(c) where the displacements of individual SPAMM data points from time 1 to time 2 are overlaid onto the short axis image at time 2 (square dots are the points at time 2).

12.2 Gel Phantom Model

We define the reference shape $\mathbf{e}_c$ of the cylindrical gel phantom as follows:

$$\mathbf{e}_c = \mathbf{e}_c(\mathbf{u}; a_0, \alpha(\mathbf{u}), a_3(\mathbf{u})) \tag{12.1}$$

$$= a_0 w \begin{pmatrix} \alpha(\mathbf{u}) \cos v \\ \alpha(\mathbf{u}) \sin v \\ a_3(\mathbf{u}) \end{pmatrix}, \tag{12.2}$$

where $-1 \leq u \leq 1$, $-\pi \leq v < \pi$, $w > 0$; $a_0 > 0$, and $0 \leq \alpha(\mathbf{u}), a_3(\mathbf{u}) \leq 1$. We also allow the twisting deformation as defined in equation (6.5). Therefore, the degrees of freedom of the gel model are:

$$\mathbf{q}_s = (a_0, \alpha(\mathbf{u}).a_3(\mathbf{u}), \tau(\mathbf{u})), \tag{12.3}$$

where a_0 is the scaling parameter that remains constant, $\alpha(u, v, w)$ and $a_3(u, w)$ will capture the radial expansion and the longitudinal variation of the gel, respectively, and $\tau(u, v, w)$ will capture twisting motion if there is any.

The fitting procedure described in Section 10.2.1 was adapted for gel shape and motion recovery. From the boundary data at the initial time (time 1), the undeformed shape of the

time 1 time 2

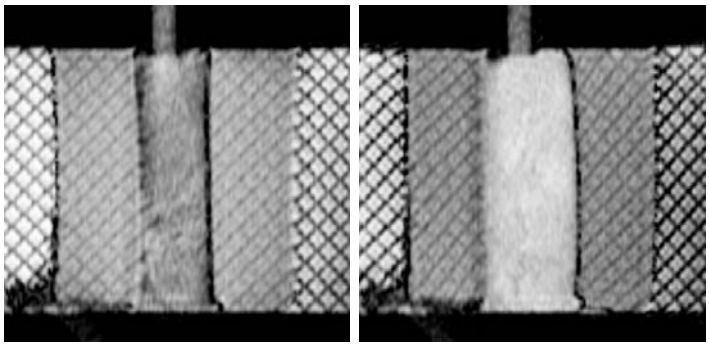

(a) long axis view

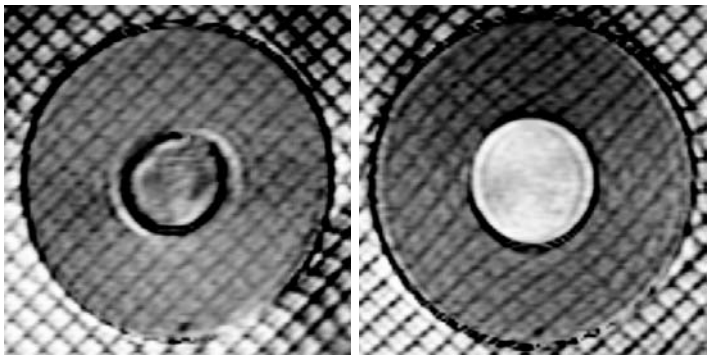

(b) short axis view

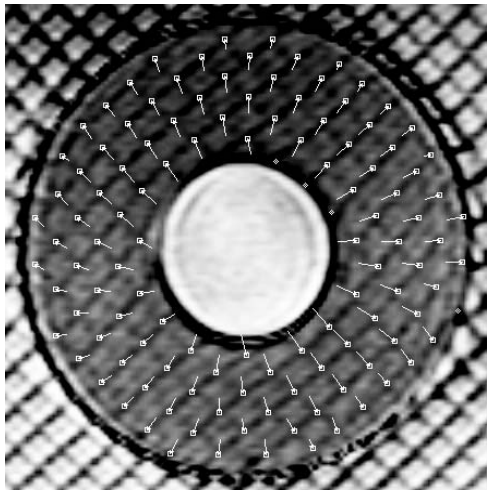

(c) displacements of SPAMM points from time1 to time 2

Figure 12.2: Gel phantom

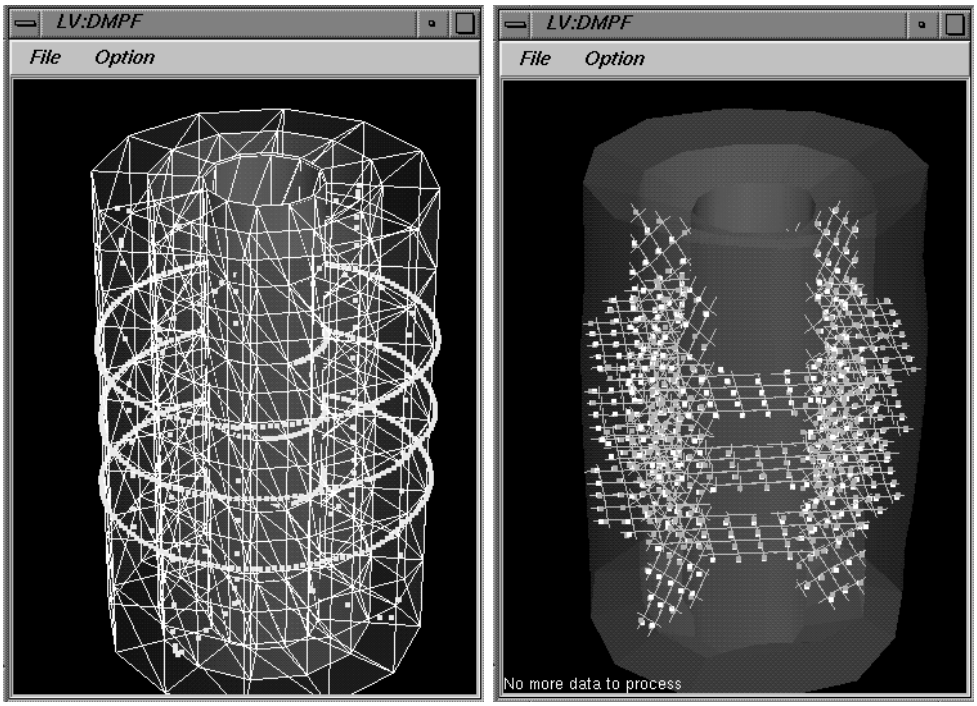

(a) time 1 (b) time 2

Figure 12.3: Gel phantom model

gel was recovered. Then the SPAMM data points at the initial time are registered into the model to identify the corresponding material points on the model. Finally, the SPAMM data points at deformed state (time 2) was read into the system, and the deformation of the gel was estimated based on its model parameter functions in equation (12.3).

The orientation of the gel model is shown at the top of Fig. 12.5, where u coordinate varies along the long axis (or the central axis) of the cylinder, v coordinate varies circularly, and w varies across the wall. The dimensions (usize, vsize, wsize) of the gel model were $7 \times 12 \times 3$. As we can see from the experimental setup described in Section 12.1.2, the top and bottom of the gel was fixed in space. However, we did not impose the constraint in the model during the fitting process. Instead, the usize is selected rather large, and we analyze the data in the mid-portion[2] where the data points are present. Fig. 12.3(a) shows the model fitted to the boundary data (white dots) at time 1, shown with meshes. The mid-wall[3] was created in the half way from both inner and outer walls. Fig. 12.3(b) shows

[2]Let us label the u-layer of the model as $u_1 \cdots u_{\mathsf{usize}}$. Then the mid-portion in this particular experiment refers to $u_3 \leq u \leq u_5$ while u ranges from u_1 to u_7.

[3]The inner-wall, mid-wall and outer-wall are the iso-surface layer of w_1, w_2 and w_3, respectively.

the deformed gel model at time 2 without meshes. The white lines in the figure correspond to initial MR tagging lines of the image. The SPAMM data points at time 1 are located at the cross-sections of the grids. The white and gray dots are the SPAMM data points and the material points at time 2, respectively.

Fig. 12.4 shows the evolution of the model during its fitting process of time 2 from time 1. We are showing only the lower portion of the gel phantom model. Again, the SPAMM data and the material points at time 1 are located at the cross sections of the white lines. The white and black dots are the the SPAMM data points and the material points at time 2, respectively. Fig. 12.4(a) shows the model right after reading the SPAMM data points of time 2. We can observe that the material points (black dots) are moving towards the SPAMM data points (white dots) at time 2, as a result of deforming each volume elements of the model based on the nodal forces computation described in Chapter 7.

12.2.1 Parameter Functions

The resulting parameter functions are plotted in Fig. 12.5. Fig. 12.5(a) shows radial deformation parameter $\alpha(u, v, w)$, at each layer of the wall (inner, mid, outer) at three locations of u where the short-axis image planes located (SA1, SA2, SA3), as a function of v which varies $-\pi$ to π. The numbers on the abscissa refer to the indices of v, where $v_1 = -\pi$ and $v_2 = \pi$. We can see that there is no significant circumferential variation (i.e., along v) of the radial deformation. But we can also see that the inner wall is expanded[4] much more than the outer wall (25% vs. 4%). The radial expansion averaged over v is provided in Fig. 12.6(a).

Fig. 12.5(b) shows plots of $a_3(u, w)$ parameter (for longitudinal contraction) at three locations along the long axis as a function of w. We can observe that there were no longitudinal motion at the central u location (SA2) while there were minor (approximately 5% maximum) longitudinal contraction[5] at the other two u locations (SA1, SA3) and more significantly towards the inner wall (w_1). We plot the averages of the longitudinal

[4]The positive sign of the value indicates a radial expansion, while the negative sign indicates the contraction.

[5]The negative sign indicates the portion of the gell moved towards center, while positive sign indicates the motion away from the center.

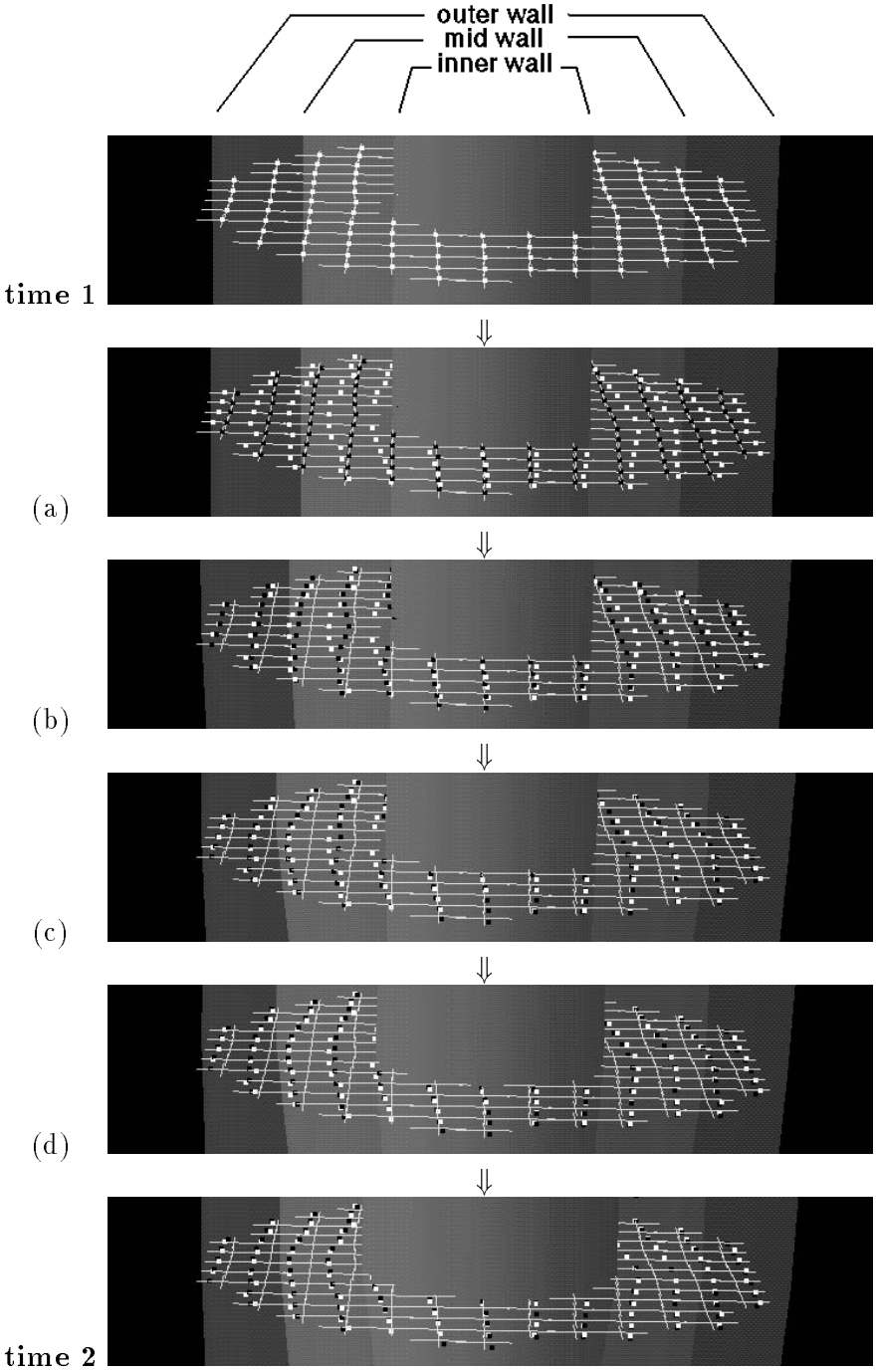

Figure 12.4: Gel model fitting

contraction in Figs. 12.6(b-c).

Fig. 12.5(c), which is the plot of τ parameter as a function of v, shows that there was some regional twist motion (approximately 2 degrees maximum for some area). The average twist plots with error bars in Figs. 12.6(d-e) also reveal that the estimated twist values are not random noise. At first we could not explain why the gel has undergone twist motion while expanding. However, we have realized that the water flow was not centered properly with respect to the gel cavity during our experiments (see Fig. 12.2(a) where we can see the tube). We can also observe from the MRI-SPAMM image in Fig. 12.2(c) that the expanding motion is not solely radial.

12.2.2 Error Analysis

Reproducibility

We ran 10 experiments with the same data set and compared the values of recovered model parameter functions. Table 12.1 shows the inter-experiments variablility is very small. For each parameter, the standard deviation (STDEV) of the estimated value at each location of the model (u, v, w) are computed from 10 experiments. The overall average standard deviation for α parameter is 0.0047 where the value of α is on the order of 10^{-1}, and the overall average standard deviation for τ parameter is 0.1633 where the value of τ is on the order of 10^{0}. Finally, the overall average standard deviation for a_3 parameter is 0.0007 where the value of a_3 is on the order of 10^{-2}.

We ran another 8 experiments with the model having various dimensions: 4 experiments with the model having only inner and outer walls (i.e., wsize = 2 vs. 3), and 4 experiments with the model which is more finely descritized circumferentially (e.g., vsize = 16 vs. 12). The results were still very similiar to the previous 10 experiments.

Discrepancy Error

For all 18 experiments described in the previous section, we projected each material points to the image plane where its corresponding SPAMM data point is located, and computed the distances between the recovered position of a material point at the deformed state and

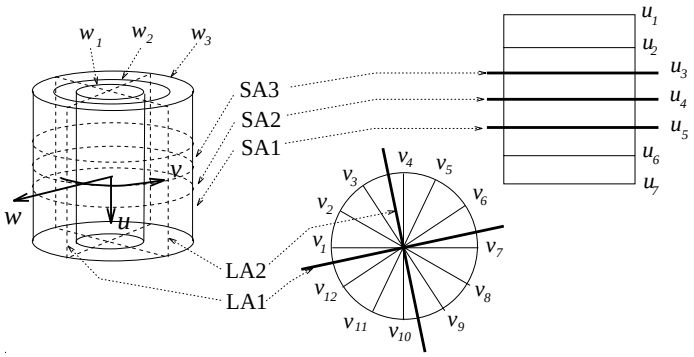

(a) α

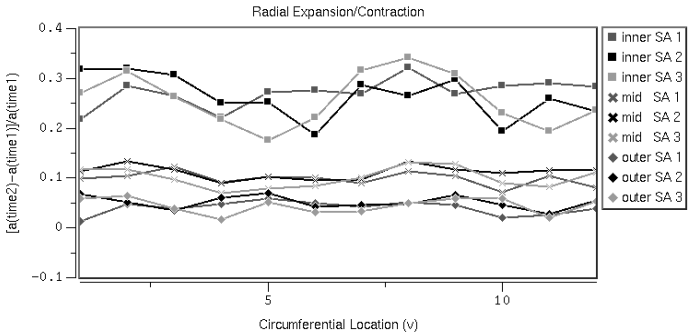

(b) a_3

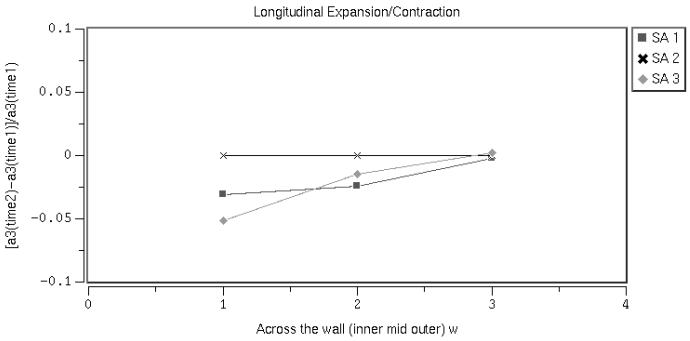

(c) τ

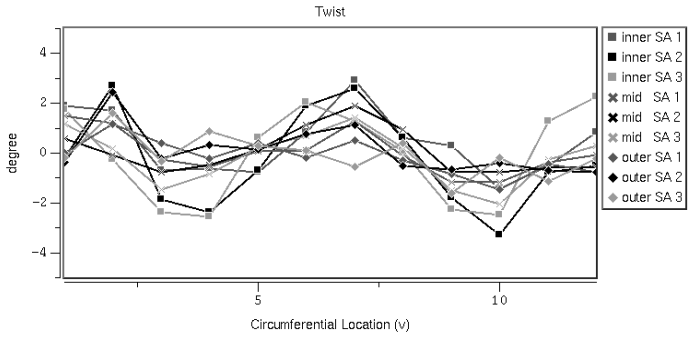

Figure 12.5: Gel model parameters

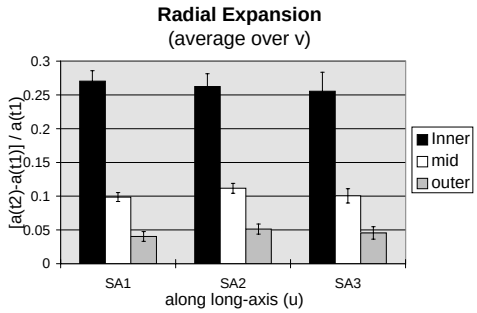

(a)

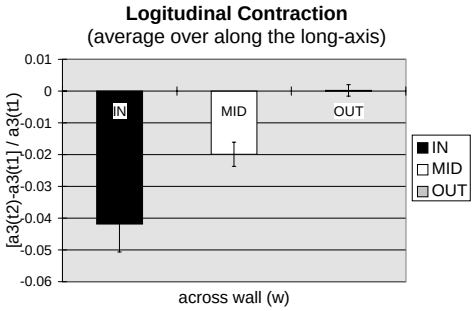

(b)

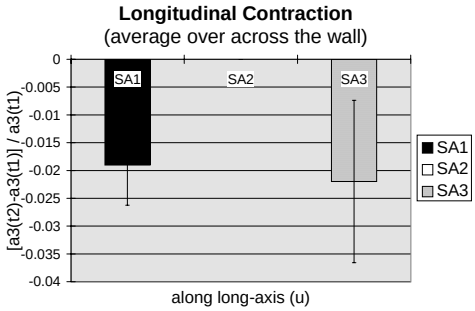

(c)

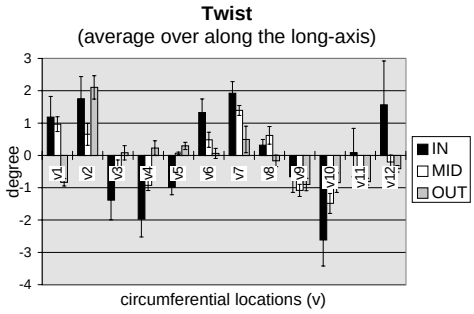

(d)

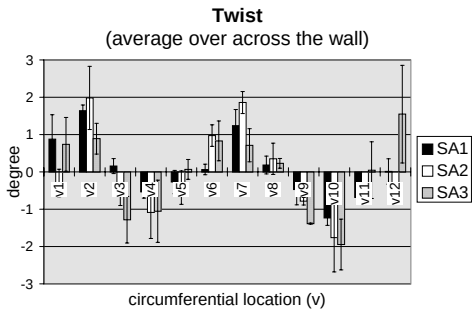

(e)

Figure 12.6: Gel model parameters (average)

STDEV$[\ {}^1\alpha(u,v,w), {}^2\alpha(u,v,w), \cdots, {}^{10}\alpha(u,v,w)\ ]$

	v_2	v_4	v_6	v_8	v_{10}	v_{12}	average
$(u_3,-,w_1)$	0.0024	0.0063	0.0132	0.0278	0.0126	0.0209	0.0116
$(u_4,-,w_1)$	0.0028	0.0037	0.0106	0.0214	0.0039	0.0045	0.0108
$(u_5,-,w_1)$	0.0026	0.0051	0.0109	0.0199	0.0086	0.0052	0.0112
$(u_3,-,w_2)$	0.0009	0.0006	0.0017	0.0035	0.0014	0.0022	0.0016
$(u_4,-,w_2)$	0.0010	0.0013	0.0016	0.0026	0.0010	0.0008	0.0017
$(u_5,-,w_2)$	0.0009	0.0009	0.0020	0.0028	0.0013	0.0007	0.0015
$(u_3,-,w_3)$	0.0016	0.0009	0.0025	0.0019	0.0006	0.0007	0.0011
$(u_4,-,w_3)$	0.0012	0.0005	0.0017	0.0015	0.0005	0.0018	0.0011
$(u_5,-,w_3)$	0.0013	0.0007	0.0019	0.0014	0.0006	0.0042	0.0016
average	0.0016	0.0022	0.0051	0.0092	0.0034	0.0046	0.0047

(a) inter-experiments variation of $\alpha(u,v,w)$

STDEV$[\ {}^1\tau(u,v,w), {}^2\tau(u,v,w), \cdots, {}^{10}\tau(u,v,w)]$

	v_1	v_3	v_5	v_7	v_9	v_{11}	average
$(u_3,-,w_1)$	0.5389	0.0754	0.2916	0.2299	0.1709	0.4166	0.2300
$(u_4,-,w_1)$	0.1079	0.2026	0.3955	0.3614	0.2930	0.1461	0.3452
$(u_5,-,w_1)$	0.3028	0.3456	0.3014	0.3376	0.3691	0.8055	0.4479
$(u_3,-,w_2)$	0.1408	0.0646	0.0551	0.0955	0.0860	0.0438	0.0745
$(u_4,-,w_2)$	0.0755	0.0772	0.0643	0.0925	0.0640	0.0594	0.0823
$(u_5,-,w_2)$	0.1195	0.0778	0.0398	0.0518	0.0935	0.1460	0.0956
$(u_3,-,w_3)$	0.1047	0.0512	0.0745	0.0349	0.0502	0.0789	0.0567
$(u_4,-,w_3)$	0.1109	0.0586	0.0619	0.0473	0.0552	0.0602	0.0679
$(u_5,-,w_3)$	0.1332	0.0863	0.0622	0.0753	0.0651	0.0513	0.0693
average	0.1816	0.1155	0.1496	0.1473	0.1386	0.1629	0.1633

(b) inter-experiments variation of $\tau(u,v,w)$

STDEV$[\ {}^1a_3(u,w), {}^2a_3(u,w), \cdots, {}^{10}a_3(u,w)]$

	w_1	w_2	w_3	average
$(u_3,\cdot,-)$	0.00121	0.00101	0.00068	0.00097
$(u_4,\cdot,-)$	0	0	0	0
$(u_5,\cdot,-)$	0.00156	0.00073	0.00063	0.00098
average	0.00092	0.00058	0.00044	0.00065

(c) inter-experiments variation of $a_3(u,w)$

Table 12.1: Test for reproducibility of the results

RMS	Mean	Max	Min
$0.2999 \pm 0.0068\ mm$	$0.2283 \pm 0.0061\ mm$	$1.2936 \pm 0.1180\ mm$	$0.0045 \pm 0.0027\ mm$

Table 12.2: Projection error statistics for the gel phantom model

inner boundary	outer boundary	both
$0.7887 \pm 0.0287\ mm$	$0.8865 \pm 0.0280\ mm$	$0.8550 \pm 0.0153\ mm$

Table 12.3: RMS error against the boundary data at time 2

the position of the corresponding SPAMM data point. The mean RMS error was $0.30 \pm 0.01\ mm$. Since the pixel size of the images is $0.625\ mm$, the error was smaller than 0.5 pixel. Table 12.2 shows the error statistics.

Accuracy

The shape of the gel model at time 2 are recovered solely based on the SPAMM data points, and we purposely did not use the boundary data set extracted from MRI-SPAMM images at time 2. Instead, we compared the observed boundaries from the MRI data and the boundaries of the model at the deformed state (time 2). The RMS errors (in mm) are given in Table 12.3. The mean RMS error was $0.86 \pm 0.02\ mm$. Although the error is almost 1.5 pixel size in this case, it is still acceptable considering that it also includes discretization error of the model[6]. We can observe that the error at the inner wall is smaller than the error at the outer wall, and we postulate that it is due to the fact that the inner wall has smaller radius which reduces the discretization error.

Comparison with physical data

In the short axis (SA) images, the direction of greatest stretch is approximately radial in all regions. Therefore, the maximum stretch is associated with wall-thickening. We computed the wall-thickening (WT) of the gel using the formula in (8.9), and compared it with the actual measurement of the gel as shown in Table 12.4. The wall-thickness is computed

[6]The circular cross section of the gel is approximated by a 12-sided polygon.

	inner wall radius (mm)	outer wall radius (mm)	wall thickness (mm)
time 1 :			
SA1	10.7087 ± 0.2204	30.7717 ± 0.4417	20.0629 ± 0.6621
SA2	10.6918 ± 0.1001	30.9904 ± 0.4038	20.2986 ± 0.5039
SA3	10.5784 ± 0.1003	31.0798 ± 0.4495	20.5014 ± 0.5498
time 2 :			
SA1	13.3708 ± 0.6202	31.7479 ± 0.4469	18.3771 ± 1.0671
SA2	13.6547 ± 0.5471	32.0095 ± 0.3594	18.3547 ± 0.9065
SA3	13.2289 ± 0.4955	32.1899 ± 0.3311	18.9611 ± 0.8266

Table 12.4: Actual wall thickness measurement of the gel phantom

	wall thickness computed from model (mm)		WT (wall thickening)	
	time 1	time 2	from model	from actual measurement
SA1	20.6082 ± 0.00000	18.9252 ± 0.4772	0.91834 ± 0.02316	0.91597
SA2	20.6082 ± 0.00000	19.3685 ± 0.5684	0.93985 ± 0.02758	0.90424
SA3	20.6082 ± 0.00000	19.2534 ± 0.6284	0.93426 ± 0.03049	0.92486

Table 12.5: Comparison of wall thickening (WT) parameter

from the average radii around inner and outer walls of the cylindrical gel.

The results of the comparison between the wall thickening (WT) parameters of the model and the actual measurement are summarized in Table 12.5. The last two columns of the table shows that WT from the model is very close to the physical measurements.

12.3 Problems and Future Work

Through the validation studies with the deformable gel phantom, we were able to verify the accuracy of the proposed technique. However, the currect experiment setup described in Section 12.1 did not provide us with the full 3-D deformation where missing through-plane motion becomes potential caveat. Moreover, the deformation of the phantom was not entriely under our control (for example, we did not expect to have any twisting motion).

In near future, we plan to perform another series of validation studies with a calibrated deformable phantom in a more controlled environment. The phantom will be designed so that we can apply constrained deformations which can be solved analytically for the given phantom. Then these analytic solutions (to be verified with optically measured deformation) will be compared with the results obtained from the proposed technique.

We will perform the similar error analysis on LV models themselves. In particular, we will verify the reproducibility of the results as well as the predictability by experimenting with an arbitrary subset of SPAMM data points to predict the excluded data points from the model. The discrepancy error at each image plane will be visualized so that we have a better idea of error distribution pertaining to the degree of through-plane motion.

We also plan to conduct systematically more experiments with more data to show the clinical usefulness. Any evaluation of the effect of disease or treatment requires a baseline reference to normal values and variation. Therefore, we will first apply the proposed technique to broad samples of normal subjects previously acquired at the Hospital of the University of Pennsylvania in order to define the normal patterns of cardiac motion. Then we will apply it to previously acquired data on patients with cardiac disease in order to link the LV motion with a particular illness in a quantitative way.

Chapter 13

Conclusion

The main focus of this dissertation is on the development of techniques for modeling and characterizing the heart wall motion with a small set of intuitive and clinically useful parameters. The specific contributions are as follows:

1. We have presented a new class of deformable model whose global parameters are functions (DMPF). It allows us to capture the local variations in a compact, accurate and intuitive way.

2. We have further developed the volumetric DMPF for the 3-D left ventricular wall motion analysis from MRI-SPAMM. In order to perform the proposed analysis,

   (a) We have identified those parameters that are sufficient to capture the original shape and the subsequent deformations of the LV,

   (b) We have developed techniques for calculating and distributing forces manifasted in MRI-SPAMM data, and

   (c) We have adapted the physics-based framework to shape and motion analysis based on the model parameters.

   With the volumetric model, we were not only able to compare endocardial deformation to epicardial deformation, but also to quantify the deformation anywhere in-between endocardium and epicardium.

3. We have applied the proposed technique to samples of normal subjects previously acquired at the Hospital of the University of Pennsylvania in order to define the normal patterns of cardiac motion.

4. We have also applied it to previously acquired patients' data in order to link the LV motion with a particular heart disease (e.g. hypertrophic cardiomyopathy) in a quantitative way.

5. We have developed visualization techniques for user-friendly processing of the analysis results, and finally

6. we have validated our methods by conducting studies with deformable phantoms and by performing error analyses.

Appendix A

Nomenclature

Φ	inertial frame of reference
ϕ	model frame of reference
$\mathbf{u}$	material coordinates $\mathbf{u} = (u, v, w)$
$\mathbf{q}$	generalized coordinates
$\mathbf{f}_q$	generalized forces
$\mathbf{x}$	position of a point on a deformable model wrt an inertial frame Φ
$\mathbf{s}$	position of a point on a deformable model wrt a model frame ϕ
$\mathbf{c}$	position of the origin of the model frame in Φ
$\mathbf{R}$	rotation matrix which gives orientation of ϕ relative to Φ
$\mathbf{J}$	Jacobian matrix of the shape primitive
$\mathbf{L}$	model Jacobian matrix
$\mathbf{D}$	damping matrix
$\mathbf{K}$	stiffness matrix
$\mathbf{S}$	SPAMM data point
$\mathbf{M}$	material point
$\mathbf{m}$	barycentric coordinates (m_a, m_b, m_c) with respect to a triangle $\mathbf{x}_a\mathbf{x}_b\mathbf{x}_c$
r	w location of a material point within a volume element
$\mathbf{f}_S$	force from a SPAMM data point
$\mathbf{f}_z$	force from a boundary data point
$\mathbf{f}$	3-D force distribution from data points

Appendix B

Quaternions

Quaternion algebra, which is originally worked out by Hamilton and Cayley in 1840's [23], provides a coherent structure for rotations. A quaternion is a 4-tuple which is represented by

$$\mathbf{q} = [\omega, v_1, v_2, v_3].$$

The interpretation given to a quaternion is a scalar and a 3-D vector, so that it may be written as:

$$\mathbf{q} = [\omega, \mathbf{v}],$$

where $\mathbf{v} = (v_1, v_2, v_3)^\top$. Let $\mathbf{q}_1 = [\omega_1, \mathbf{v}_1]$ and $\mathbf{q}_2 = [\omega_2, \mathbf{v}_2]$. Then some basic quaternion algebra is given as follows:

addition	:	$\mathbf{q}_1 + \mathbf{q}_2$	=	$[\omega_1 + \omega_2, \mathbf{v}_1 + \mathbf{v}_2]$
multiplication	:	$\mathbf{q}_1\mathbf{q}_2$	=	$[\omega_1\omega_2 - \mathbf{v}_1 \cdot \mathbf{v}_2,\ \omega_1\mathbf{v}_2 + \omega_2\mathbf{v}_1 + \mathbf{v}_1 \times \mathbf{v}_2]$
norm	:	$\|\mathbf{q}\|$	=	$\omega^2 + \mathbf{v} \cdot \mathbf{v}$
conjugate	:	$\mathbf{q}^*$	=	$[\omega, -\mathbf{v}]$
inverse	:	$\mathbf{q}^{-1}$	=	$\frac{\mathbf{q}^*}{\|\mathbf{q}\|}$
identity	:	$\mathbf{q}\mathbf{q}^{-1}$	=	$[1, 0, 0, 0]$

A unit quaternion is a symbol of the form $\omega + v_1\mathbf{i} + v_2\mathbf{j} + v_3\mathbf{k}$ where ω, v_1, v_2, and v_3 are real numbers satisfying

$$\omega^2 + v_1^2 + v_2^2 + v_3^2 = 1,$$

with

$$\mathbf{i}^2 = \mathbf{j}^2 = \mathbf{k}^2 = \mathbf{ijk} = -1.$$

If $\mathbf{q}_1$ and $\mathbf{q}_2$ are unit quaternions, then $\|\mathbf{q}_1\| = \|\mathbf{q}_2\| = 1$, $\|\mathbf{q}_1\mathbf{q}_2\| = 1$, and $\mathbf{q}_1^{-1} = \mathbf{q}_1^*$. Many properties of quaternions can be found in work by Shoemake [92, 93], where unit quaternions are thought of as points on the unit sphere in 4-D.

Rotation by angle θ about the unit vector $\mathbf{v} = (v_1, v_2, v_3)^\top$ corresponds to the quaternion

$$\cos\left(\frac{\theta}{2}\right) + v_1 \sin\left(\frac{\theta}{2}\right)\mathbf{i} + v_2 \sin\left(\frac{\theta}{2}\right)\mathbf{j} + v_3 \sin\left(\frac{\theta}{2}\right)\mathbf{k}.$$

Let $\mathbf{q} = [\omega, \mathbf{v}]$ be a unit quaternion. To perform a roation on a vector using a quaternion, we compute

$$\mathbf{q}\ [0, \mathbf{p}]\ \mathbf{q}^{-1},$$

which produces a quaternion whose scalar part is zero and whose vector part represents a rotation of $\mathbf{p}$ about the direction $\mathbf{v}$ with angle $\theta = 2\cos^{-1}\omega$. The magnitude of $\mathbf{v}$ becomes $\sin\frac{\theta}{2}$ from the unit quaternion formulation. Therefore, performing successive rotations corresponds to multiplying quaternions (i.e., the combination of rotation by $\mathbf{q}_1$ followed by $\mathbf{q}_2$ is given by its mutiplication $\mathbf{q} = \mathbf{q}_2\mathbf{q}_1$)[1]. The corresponding rotation matrix $\mathbf{R}$ can be written in terms of ω and $\mathbf{v}$ as follows:

$$\mathbf{R} = \begin{bmatrix} 1 - 2({v_2}^2 + {v_3}^2) & 2(v_1v_2 - \omega v_3) & 2(v_1v_3 + \omega v_2) & 0 \\ 2(v_1v_2 + \omega v_3) & 1 - 2({v_1}^2 + {v_3}^2) & 2(v_2v_3 - \omega v_1) & 0 \\ 2(v_1v_3 - \omega v_2) & 2(v_2v_3 + \omega v_1) & 1 - 2({v_1}^2 + {v_2}^2) & 0 \\ 0 & 0 & 0 & 1 \end{bmatrix} \tag{B.1}$$

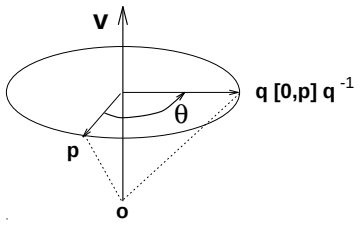

Figure B.1: Rotation by angle θ about the axis of rotation $\mathbf{v}$

[1] $\mathbf{q}_2(\mathbf{q}_1[0,\mathbf{p}]\mathbf{q}_1^{-1})\mathbf{q}_2^{-1} = (\mathbf{q}_2\mathbf{q}_1)[0,\mathbf{p}](\mathbf{q}_2\mathbf{q}_1)^{-1} = \mathbf{q}[0,\mathbf{p}]\mathbf{q}^{-1}$

Appendix C

Barycentric Coordinates

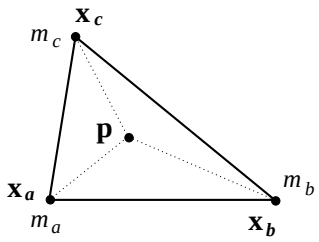

Barycentric combinations are weighted sums of points where the weights sum to one [33]. Consider a triangle with vertices $\mathbf{x}_a$, $\mathbf{x}_b$ and $\mathbf{x}_c$, and a point $\mathbf{p}$ on the same plane where the triangle lies. It is always possible to write $\mathbf{p}$ in terms of $\mathbf{x}_a$, $\mathbf{x}_b$ and $\mathbf{x}_c$ as a barycentric combination as follows:

$$\mathbf{p} = m_a\mathbf{x}_a + m_b\mathbf{x}_b + m_c\mathbf{x}_c; \qquad m_a + m_b + m_c = 1. \tag{C.1}$$

$\mathbf{m} = (m_a, m_b, m_c)$ are called barycentric coordinates of $\mathbf{p}$ with respect to $\mathbf{x}_a$, $\mathbf{x}_b$ and $\mathbf{x}_c$.

$$\begin{bmatrix} | & | & | \\ \mathbf{x}_a & \mathbf{x}_b & \mathbf{x}_c \\ | & | & | \end{bmatrix} \begin{bmatrix} m_a \\ m_b \\ m_c \end{bmatrix} = \begin{bmatrix} | \\ \mathbf{p} \\ | \end{bmatrix} \tag{C.2}$$

We can write (C.2) as:

$$\mathbf{X}\ \mathbf{M} = \mathbf{P}$$

Therefore,

$$\mathbf{M} = \mathbf{X}^{-1}\mathbf{P}. \tag{C.3}$$

Solving the linear system in (C.2) for $\mathbf{m}$, when 4 points $\mathbf{x}_a$, $\mathbf{x}_b$, $\mathbf{x}_c$, $\mathbf{p}$ are given, is analogous to applying Cramer's rule as follows:

$$\begin{aligned} m_a &= \frac{\text{area}(\mathbf{p}, \mathbf{x}_b, \mathbf{x}_c)}{\text{area}(\mathbf{x}_a, \mathbf{x}_b, \mathbf{x}_c)}; \\ m_b &= \frac{\text{area}(\mathbf{x}_a, \mathbf{p}, \mathbf{x}_c)}{\text{area}(\mathbf{x}_a, \mathbf{x}_b, \mathbf{x}_c)}; \\ m_c &= \frac{\text{area}(\mathbf{x}_a, \mathbf{x}_b, \mathbf{p})}{\text{area}(\mathbf{x}_a, \mathbf{x}_b, \mathbf{x}_c)}. \end{aligned} \tag{C.4}$$

In order for the equations in (C.4) to be well defined, the area$(\mathbf{x}_a, \mathbf{x}_b, \mathbf{x}_c)$ must be non-zero: i.e., in order for $\mathbf{X}$ in (C.3) to be invertible, $\mathbf{x}_a$, $\mathbf{x}_b$ and $\mathbf{x}_c$ should not be collinear.

Barycentric coordinates are *affinely invariant* so that if $\mathbf{p}$ have barycentric coordinates $\mathbf{m}$ with respect to $\mathbf{x}_i$ where $i = a, b, c$, $\Psi\mathbf{p}$ has the same barycentric coordinates m with respect to $\Psi\mathbf{x}_i$ where Ψ is an affine map.

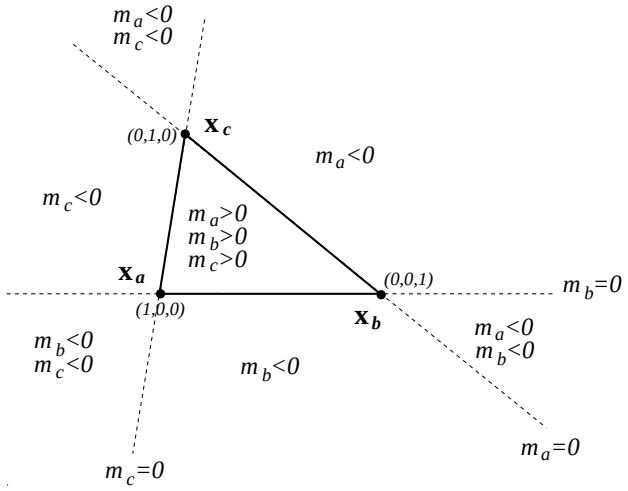

Figure C.1: Barycentric coordinates (m_a, m_b, m_c) with respect to $\mathbf{x}_a$, $\mathbf{x}_b$ and $\mathbf{x}_c$

The triangle $\mathbf{x}_a$, $\mathbf{x}_b$, and $\mathbf{x}_c$ defines a coordinate system in the plane. Based on the barycentric coordinates m_a, m_b and m_c we can identify where the point $\mathbf{p}$ lies with respect to the triangle as shown in Fig. C.1. For example, if $m_a > 0$, $m_b > 0$ and $m_c > 0$, $\mathbf{p}$ lies inside of the triangle.

Appendix D

Signed Distance from Point to Plane

which-side-of-plane test

In order to test which side the point $\mathbf{P}$ is located with respect to a given plane whose normal vector is $\mathbf{N}$, we compute the signed distance from the point to the plane [39] as follows: Choose any point $\mathbf{R}$ on the plane as shown in Fig. D. Then the signed distance d

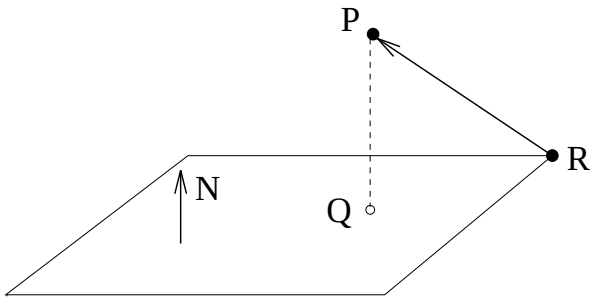

is computed as

$$d = \mathbf{N} \cdot (\mathbf{P} - \mathbf{R}). \tag{D.1}$$

If d is positive, the point $\mathbf{P}$ lies on the same side of the plane as its normal $\mathbf{N}$. If d is negative, $\mathbf{P}$ lies backside of the plane. Finally, if d is zero, $\mathbf{P}$ is on the plane. Based on d, we can compute the projected point $\mathbf{Q}$ on the plane as follows:

$$\mathbf{Q} = \mathbf{P} - d\mathbf{N}.$$

Bibliography

[1] A. Amini and J. Duncan. Pointwise tracking of left-ventricular motion in 3D. In *Proc. IEEE Workshop on Visual Motion*, pages 294–298, Princeton, NJ, 1991.

[2] T. Arts, W. C. Hunter, A. Douglas, M. M. Muijtjens, and R. S. Reneman. Description of the deformation of the left ventricle by a kinematic model. *J. Biomechanics*, 25(10):1119–1127, 1992.

[3] T. Arts, W. C. Hunter, A. S. Douglas, A. M. M. Muijtjens, J. W. Corsel, and R. S. Reneman. Macroscopic three-dimensional motion patterns of the left ventricle. *Advances in Experimental Medicine and Biology*, 346:383–392, 1993.

[4] T. Arts, P. C. Veenstra, and R. S. Reneman. Epicardial deformation and left ventricle wall mechanics during ejection in the dog. *Am. J. Physiol.*, 243:H379–H390, 1982.

[5] L. Axel, D. Bloomgarden, C-N Cheng, D. Kraitchman, and A. A. Young. SPAM-MVU: A program for the analysis of dynamic tagged MRI. In *Book of Abstracts: Society of Magnetic Resonance in Medicine*, page 724, 1993.

[6] L. Axel and L. Dougherty. Heartwall motion: Improved method of spatial modulation of magnetization for MR imaging. *Radiology*, 172:349–350, 1989.

[7] L. Axel, R. Gonçalves, and D. Bloomgarden. Regional heart wall motion: Two-dimensional analysis and functional imaging of regional heart wall motion with magnetic resonance imaging. *Radiology*, 183:745–750, 1992.

[8] H. Azhari, M. Buchalter, S. Sideman, E. Shapiro, and R. Beyar. A conical model to describe the nonuniformity of the left ventricular twisting motion. *Annals of Biomedical Engineering*, 20:149–165, 1992.

[9] R. Bajcsy and F. Solina. Three dimensional object representation revisited. In *Proc. the 1st International Conference on Computer Vision (ICCV87)*, pages 231–240, London, England, June 1987. IEEE Computer Society, IEEE Computer Society Press.

[10] M. Bajura, H. Fuchs, and R. Ohbuchi. Merging virtual objects with the real world: Seeing ultrasound imagery within the patient. *Computer Graphics*, 26:203–210, 1992.

[11] E. Bardinet, N. Ayache, and L. D. Cohen. Fitting of iso-surfaces using superquadrics and free-form deformations. In *Proc. IEEE Workshop on Biomedical Image Analysis*, pages 184–193, Seattle, WA, June 1994.

[12] A. H. Barr. Superquadrics and angle-preserving transformations. *IEEE Computer Graphics and Application*, 1:11–23, 1981.

[13] A. H. Barr. Global and local deformations of solid primitives. *Computer Graphics*, 18(3):21–30, July 1984.

[14] K.-J. Bathe and E. L. Wilson. *Numerical Methods in Finite Element Analysis*. Prentice-Hall, Englewood Cliffs, NJ, 1976.

[15] R. Beyar and S. Sideman. Effect of the twisting motion on the non-uniformities of transmural fiber mechanics and energy demands - a theoretical study. *IEEE Trans. Biomed. Eng.*, 32:764–769, 1985.

[16] T. Binford. Visual perception by computer. In *Proc. IEEE Conference on Systems and Control*, Dec 1971.

[17] W. Boehm. *Differential Geometry II*, chapter 21, pages 275–291. Academic Press, Inc., San Diego, CA, 1988.

[18] R. M. Bolle and B. C. Vemuri. On three-dimensional surface reconstruction methods. *IEEE Trans. Pattern Analysis and Machine Intelligence (PAMI)*, 13(1):1–13, 1991.

[19] T. E. Boult and A. D. Gross. Recovery of superquadrics from 3-D information. In *Proc. SPIE Intelligent Robots and Computer Vision*, volume 848, pages 358–365, Nov 1987.

[20] Britannica. *The New Encyclopædia Britannica*, volume 7. Encyclopaedia Britannica, Inc., Chicago, 15th edition, 1995.

[21] R. W. Brower, H. T. ten Katen, and G.J. Meester. Direct method for determining regional myocardial shortening after bypass surgery from radiopaque markers in man. *Am. J. Cardiol.*, 41:1222–1229, 1978.

[22] M. B. Buchalter, J. L. Weiss, W. L. Rogers, E. A. Zerhouni, M. L. Weisfeldt, R. Beyar, and E. P. Shapiro. Noninvasive quantification of left ventricular rotational deformation in normal humans using magnetic resonance imaging myocardial tagging. *Circulation*, 81:1236–1244, 1990.

[23] P. Burger and D. Gillies. *Interactive Computer Graphics*. Addison-Wesley Publishing Company, Inc., Wokingham, England, 1989.

[24] Goldstein D. C., Kundel H. L., Duabe-Witherspoon M. E., Thibault L. E., and Goldstein E. J. A silicone gel phantom suitable for multimodality imaging. *Investigative Radiology*, 22:153–157, 1987.

[25] G. Celniker. Deformable curve and surface finite elements for free-form shape design. *Computer Graphics*, 25:257–266, 1991.

[26] C. W. Chen and T. S. Huang. Epicardial motion and deformation estimation from coronary artery bifurcation points. In *Proc. 3rd International Conference on Computer Vision (ICCV90)*, pages 456–459, Osaka, Japan, Dec 1990.

[27] L. D. Cohen and I. Cohen. A finite element method applied to new active contour models and 3D reconstruction from cross sections. In *Proc. 3rd International Conference on Computer Vision (ICCV90)*, pages 587–591, Osaka, Japan, Dec 1990.

[28] R. W. Conners. Computer vision in digital radiography. In H. U. Lemke, M. L. Rhodes, C. C. Jaffee, and R. Felix, editors, *Computer Assisted Radiology*, pages 451–460, Berlin, Heidelberg, 1985. Springer-Verlag.

[29] J. J. Craig. *Introduction to robotics : mechanics and control.* Addison-Wesley Publishing Company, Inc., Reading, Mass., 1986.

[30] C. de Boor. *A practical guide to splines*, volume 27 of *Applied mathematical sciences.* Springer-Verlag, New York, 1978.

[31] D. DeCarlo and D. Metaxas. Blended deformable models. *IEEE Trans. Pattern Analysis and Machine Intelligence (PAMI)*, 18(4):443–448, April 1996.

[32] T. S. Denney and J. L. Prince. 3D displacement field reconstruction from planar tagged cardiac MR images. In *Proc. IEEE Workshop on Biomedical Image Analysis*, pages 51–60, Seattle, WA, June 1994.

[33] G. E. Farin. *Curves and Surfaces for Computer Aided Geometric Design.* Academic Press, Inc., San Diego, CA, 1988.

[34] S. E. Fischer, G. C. McKinnon, M. B. Scheidegger, W. Prins, D. Meier, and P. Boesiger. True myocardial motion tracking. *Magnetic Resonance in Medicine*, 31:401–413, 1994.

[35] D. Friboulet, I. E. Magnin, C. Mathieu, A. Pommert, and K. H. Hoehne. Assessment and visualization of the curvature of the left ventricle from 3D medical images. *Computerized Medical Imaging and Graphics*, 17(4/5):257–262, 1993.

[36] D. Friboulet, I. E. Magnin, and D. Revel. Assessment of a model for overall left ventricular three-dimensional motion from MRI data. *International Journal of Cardiac Imaging*, 8:175–190, 1992.

[37] Y. C. Fung. *Boimechanics: Motion, Flow, Stress and Growth.* Springer, New York, 1990.

[38] M. Gardiner. Mathematical games. *Scientific American*, 213, 1965.

[39] P. Georgiades. *Signed distance from point to plane*, chapter V. 3, pages 223–224. The Graphics Gems. AP Professional, Boston, 1992.

[40] D. N. Ghista and M. S. Hamid. Finite element stress analysis of the human left ventricle whose irregular shape is developed from single plane cineangiocardiogram. *Computer Programs in Biomedicine*, 7:219–231, 1977.

[41] A. E. Green and W. Zerna. *Theoretical Elasticity.* Oxford University Press, Ely House, London, 2nd edition, 1968.

[42] A. D. Gross and T. E. Boult. Error of fit measures for recovering parametric solids. In *Proc. 2nd International Conference on Computer Vision (ICCV88)*, pages 690–694, 1988.

[43] J. M. Guccione, K. D. Costa, and A. D. McCulloch. Finite element stress analysis of left ventricular mechanics in the beating dog heart. *J. Biomechanics*, 28(10):1167–1177, 1995.

[44] J. M. Guccione and A. D. McCulloch. Finite element modeling of ventricular mechanics. In L. Glass, P. Hunter, and A. McCulloch, editors, *Theory of Heart: biomechanics, biophysics, and nonlinear dynamics of cardiac function*, pages 121–144. Springer-Verlag, New York, 1991.

[45] D. C. Harrison, A. Goldblatt, E. Braunwald, G. Glick, and D. T. Mason. Studies on cardiac dimensions in intact unanesthetized man. 1. description of techniques and their validation. *Circ. Res.*, 13:448–455, 1963.

[46] P. B. Heffernan and R. A. Robb. A new method for shaded surface display of biological and medical images. *IEEE Trans. Medical Imaging*, 4(1):26–38, 1985.

[47] W. C. Huang and D. Goldgof. Adaptive-size meshes for rigid and nonrigid shape analysis and synthesis. *IEEE Trans. Pattern Analysisand Machine Intelligence (PAMI)*, 15(6):611–616, 1993.

[48] P. J. Hunter and B. H. Smaill. The analysis of cardiac function: A continuum approach. *Prog. Biophys. Molec. Biol.*, 52:101–164, 1988.

[49] R. F. Janz and R. J. Waldron. Predicted effect of chronic apical aneurysms on the passive stiffness of the human left ventricle. *Circ. Res.*, 42(2):255–263, 1978.

[50] C. Kambhamettu and D. Goldgof. Point correspondence recovery in non-rigid motion. In *Proc. IEEE Conference on Computer Vision and Pattern Recognition (CVPR92)*, pages 222–227, Champaign, Illinois, June 1992.

[51] H. Kardestuncer, editor. *Finite element handbook*. McGraw–Hill, New York, 1987.

[52] M. Kass, A. Witkin, and D. Terzopoulos. Snakes: Active contour models. *International Journal of Computer Vision*, 1(4):321–331, 1988.

[53] H. C. Kim, B. G. Min, M. M. Lee, J. D. Seo, Y. W. Lee, and M. C. Han. Estimation of local cardiac wall deformation and regional wall stress from biplane coronary cineangiograms. *IEEE Trans. Biomed. Eng.*, 32:503–511, 1985.

[54] J. Lessick, S. sideman, H. Azhari, M. Marcus, E. Grenadier, and R. Beyar. Regional three-dimensional geometry and function of left ventricles with fibrous aneurysms. *Circulation*, 84(3):1072–1086, 1991.

[55] D. Marr. *Vision*. W. H. Freeman and Company, New York, 1982.

[56] D. Marr and K. Nishihara. Representation and recognition of the spatial organization of three-dimensional shapes. In *Proc. Royal Society London B*, 1978.

[57] A. D. McCulloch, B. H. Smaill, and P. J. Hunter. Regional left ventricular epicardial deformation in the passive dog heart. *Circ. Res.*, 64:721–733, 1989.

[58] T. McInerney and D. Terzopoulos. A finite element model for 3D shape reconstruction and nonrigid motion tracking. In *Proc. 4th International Conference on Computer Vision (ICCV93)*, pages 518–523, Berlin, Germany, 1993.

[59] G. D. Meier, A. A. Bove, W. P. Santamore, and P. R. Lynch. Contractile function in canine right ventricle. *Am. J. Physiol.*, 239:H794–H804, 1980.

[60] D. Metaxas. *Physics-Based Modeling of Nonrigid Objects for Vision and Graphics*. PhD thesis, University of Toronto, 1992.

[61] D. Metaxas and D. Terzopoulos. Constrained deformable superquadrics and nonrigid motion tracking. In *Proc. IEEE Conference on Computer Vision and Pattern Recognition (CVPR91)*, pages 337–343, Hawaii, 1991.

[62] D. Metaxas and D. Terzopoulos. Recursive estimation of nonrigid shape and motion. In *Proc. IEEE Motion Workshop*, pages 306–311, Princeton, NJ, Oct 1991.

[63] D. Metaxas and D. Terzopoulos. Shape and nonrigid motion estimation through physics-based synthesis. *IEEE Trans. Pattern Analysis and Machine Intelligence (PAMI)*, 15(6):569–579, 1993.

[64] S. K. Mishra and D. B. Goldgof. Motion analysis and modeling of epicardial surfaces from point and line correspondences. In *Proc. IEEE Workshop on Visual Motion*, pages 300–305, Princeton, NJ, Oct 1991.

[65] C. C. Moore, W. G. O'Dell, E. R. McVeigh, and E. A. Zerhouni. Calculation of three-dimensional left ventricular strains form biplanar tagged MR images. *J. Mag. Res. Imag.*, 2:165–175, 1992.

[66] M. E. Mortenson. *Geometric Modeling*. John Wiley & Sons, 1985.

[67] C. Nastar and N. Ayache. Classification of nonrigid motion in 3D images using physics-based vibration analysis. In *Proc. IEEE Workshop on Biomedical Image Analysis*, pages 61–69, Seattle, WA, June 1994.

[68] R. Nevatia. Shape analysis and recognition. In *Machine Perception*, chapter 5, pages 61–89. Prentice-Hall, Inc., Englewood Cliffs, NJ, 1982.

[69] S. M. Nidorf and A. E. Weyman. Left ventricle II: Quantification of segmental dysfunction. In *Principles and practice of echocardiography*, pages 625–655. Lea & Febiger, Philadelphia, 1994.

[70] W. G. O'Dell, C. C. Moore, W. C. Hunter, E. A. Zerhouni, and E. R. McVeigh. Three-dimensional myocardial deformations: Calculation with displacement field fitting to tagged MR images. *Radiology*, 195(3):829–835, June 1995.

[71] W. G. O'Dell, C. C. Moore, and E. R. McVeigh. Displacement field fitting approach to calculate 3D deformations from parallel-tagged MR images. *J. Magn, Reson. Imag.*, 3(P):P208, 1993.

[72] P. V. O'Neil. *Advanced engineering mathematics.* Wadsworth Pub. Co., Belmont, Calif., 2nd edition, 1987.

[73] L. C. Palmon, N. Reichek, S. B. Yeon, N. R. Clark, D. Brownson, E. Hoffman, and L. Axel. Intramural myocardial shortening in hypertensive left ventricular hypertrophy with normal pump function. *Circulation*, 89(1):122–131, Jan 1994.

[74] J. Park, D. Metaxas, and L. Axel. Volumetric deformable models with parameter functions: A new approach to the 3D motion analysis of the lv from MRI-SPAMM. In *Proc. 5th International Conference on Computer Vision (ICCV95)*, pages 700–705, Cambridge, Massachusetts, June 1995.

[75] J. Park, D. Metaxas, and L. Axel. Analysis of left ventricular wall motion based on volumetric deformable models and MRI-SPAMM. *Medical Image Analysis*, 1(1):53–71, March 1996.

[76] J. Park, D. Metaxas, and A. A. Young. Deformable models with parameter functions: Application to heart wall modeling. In *Proc. IEEE Conference on Computer Vision and Pattern Recognition (CVPR94)*, pages 437–442, Seattle, WA, June 1994.

[77] J. Park, D. Metaxas, A. A. Young, and L. Axel. Model-based analysis of cardiac motion from tagged MRI data. In *Proc. Seventh Annual IEEE Symposium on Computer-Based Medical Systems*, pages 40–45, Winston-Salem, North Carolina, June 1994.

[78] J. Park, D. Metaxas, A. A. Young, and L. Axel. Deformable models with parameter functions for cardiac motion analysis from tagged MRI data. *IEEE Trans. Medical Imaging*, 15(3):278–289, June 1996.

[79] A. Pentland and B. Horowitz. Recovery of non-rigid motion and structure. *IEEE Trans. Pattern Analysis and Machine Intelligence (PAMI)*, 13(7):730–742, 1991.

[80] A. Pentland, B. Horowitz, and S. Sclaroff. Non-rigid motion and structure from contour. In *Proc. IEEE Workshop on Visual Motion*, pages 288–293, Princeton, NJ, Oct 1991.

[81] A. Pentland and S. Sclaroff. Closed-form solutions for physically based shape modeling and recognition. *IEEE Trans. Pattern Analysis and Machine Intelligence (PAMI)*, 13(7):715–729, 1991.

[82] A. Pentland and J. Williams. Good vibrations: Modal dynamics for graphics and animation. *Computer Graphics*, 23(3):215–222, 1989.

[83] W. H. Press, B. P. Flannery, S. A. Teukolsky, and W. T. Vetterling. *Numerical Recipes in C : The Art of Scientific Computing*. Cambridge University Press, Cambridge, UK, 1988.

[84] J. S. Rankin, P. A. McHale, C. E. Artentzen, D. Ling, J. C. Greenfield, and R. W. Anderson. The three-dimensional dynamic geometry of the left ventricle in the conscious dog. *Circ. Res.*, 39:304–313, 1976.

[85] R. A. Robb and C. Barillot. Interactive display and analysis of 3-D medical images. *IEEE Trans. Medical Imaging*, 8(3):217–226, 1989.

[86] W. Rogers, E. Shapiro, J. Weiss, M. Buchalter, F. Rademakers, M. Weisfeldt, and E. Zerhouni. Quantification of and correction for left ventricular systolic long-axis shortening by magnetic resonance tissue tagging and slice isolation. *Circulation*, 84:721–731, 1991.

[87] S. Sclaroff and A. Pentland. On modal modeling for medical images: Undercon-strained shape description and data compression. In *Proc. IEEE Workshop on Biomedical Image Analysis*, pages 70–79, Seattle, WA, June 1994.

[88] T. W. Sederberg and S. R. Parry. Free-form deformation of solid geometric models. *Computer Graphics*, 20(4):151–160, August 1986.

[89] A. A. Shabana. *Dynamics of Multibody Systems*. A Wiley-Interscience Publication, New York, 1988.

[90] P. Shi, A. Amini, G. Robinson, A. Sinusas, C. T. Constable, and J. Duncan. Shape-based 4D left ventricular myocardial function analysis. In *Proc. IEEE Workshop on Biomedical Image Analysis*, pages 88–97, Seattle, WA, June 1994.

[91] P. Shi, G. Robinson, C. T. Constable, A. Sinusas, and J. Duncan. A model-based integrated approach to track myocardial deformation using displacement and velocity constraints. In *Proc. 5th International Conference on Computer Vision (ICCV95)*, pages 687–692, Cambridge, Massachusetts, June 1995.

[92] K. Shoemake. Animating rotation with quaternion curves. *Computer Graphics*, 19(3):245–254, 1985.

[93] K. Shoemake. ARCBALL: A user interface for specifying three-dimensinal orientation using a mouse. In *Proceedings of Graphics Interface '92*, pages 151–156, May 1992.

[94] F. Solina. Shape recovery and segmentation with deformable part models. Technical Report MS-CIS-87-111, University of Pennsylvania, Philadelphia, PA, December 1987. Grasp Lab 128.

[95] A. J. M. Spencer. *Continuum mechanics*. Longman Inc., New York, 1980.

[96] R. Tennant and C. J. Wiggers. The effect of coronary occlusion on myocardial contraction. *Am. J. Physiol.*, 112:351–361, 1935.

[97] D. Terzopoulos. Multilevel computational processes for visual surface reconstruction. *Computer Vision, Graphics, and Image Processing*, 24:52–96, 1983.

[98] D. Terzopoulos. Regularization of inverse visual problems involving discontinuities. *IEEE Trans. Pattern Analysis and Machine Intelligence (PAMI)*, 8(4):413–424, July 1986.

[99] D. Terzopoulos and K. Fleischer. Modeling inelastic deformation: Viscoelasticity, plasticity, fracture. *Computer Graphics*, 22(4):269–278, 1988.

[100] D. Terzopoulos and D. Metaxas. Dynamic 3D models with local and global deformations: Deformable superquadrics. *IEEE Trans. Pattern Analysis and Machine Intelligence (PAMI)*, 13(7):703–714, 1991.

[101] D. Terzopoulos, J. Platt, A. Barr, and K. Fleischer. Elastically deformable models. *Computer Graphics*, 21(4):205–214, July 1987.

[102] D. Terzopoulos, A. Witkin, and M. Kass. Constraints on deformable models: Recovering 3D shape and nonrigid motion. *Artificial Intelligence*, 36:91–123, 1988.

[103] F. L. Villarreal, L. K. Waldman, and W. Y. W. Lew. A technique for measuring regional two-dimensional finite strains in canine left ventricle. *Circ. Res.*, 62:711–721, 1988.

[104] L. K. Waldman, Y. C. Fung, and J. W. Covell. Transmural myocardial deformation in the canine left ventricle: Normal in vivo three-dimensional finite strains. *Circ. Res.*, 57:152–163, 1985.

[105] Y. F. Wang and J-F Wang. Surface reconstruction using deformable models with interior and boundary constraints. In *Proc. 3rd International Conference on Computer Vision (ICCV90)*, pages 300–303, Osaka, Japan, Dec 1990.

[106] D. S. Weld and J. de Kleer, editors. *Qualitative Reasoning about Physical Systems.* Morgan Kaufmann Publishers, 1990.

[107] A. Young. Epicardial deformation from coronary cineangiograms. In L. Glass, P. Hunter, and A. McCulloch, editors, *Theory of Heart: biomechanics, biophysics, and nonlinear dynamics of cardiac function*, pages 175–207. Springer-Verlag, New York, 1991.

[108] A. Young and L. Axel. Non-rigid heart wall motion using MR tagging. In *Proc. IEEE Conference on Computer Vision and Pattern Recognition (CVPR92)*, pages 399–404, Champaign, Illinois, June 1992.

[109] A. A. Young and L. Axel. Three-dimensional motion and deformation of the heart wall: Estimation with spatial modulation of magnetization - a model-based approach. *Radiology*, 185:241–247, 1992.

[110] A. A. Young, L. Axel, L. Dougherty, D. K. Bogen, and C. S. Parenteau. Validation of tagging with MR imaging to estimate material deformation. *Radiology*, 188:101–108, 1993.

[111] A. A. Young, P. J. Hunter, and B. H. Smaill. Estimation of epicardial strain using the motions of coronary bifurcations in biplane cineangiography. *IEEE Trans. Biomed. Eng.*, 39:526–531, 1992.

[112] A. A. Young, H. Imai, C.-N. Chang, and L. Axel. Two-dimensional left ventricular deformation during systole using magnetic resonance imaging with spatial modulation of magnetization. *Circulation*, 89(2):740–752, Feb 1994.

[113] A. A. Young, D. L. Kraitchman, and L. Axel. Deformable models for tagged MR images: Reconstruction of two- and three-dimensional heart wall motion. In *Proc. IEEE Workshop on Biomedical Image Analysis*, pages 317–323, Seattle, WA, June 1994.

[114] A. A. Young, D. L. Kraitchman, L. Dougherty, and L. Axel. Tracking and finite element analysis of stripe deformation in magnetic resonance tagging. *IEEE Trans. Medical Imaging*, 14(3):413–421, 1995.

[115] A. A. Young, C. M. Kramer, V. A. Ferrari, L. Axel, and N. Reichek. Three-dimensional left ventricular deformation in hypertrophic cardiomyopathy. *Circulation*, 90(2):854–867, Aug 1994.

[116] E. A. Zerhouni, D. M. Parish, W. J. Rogers, A. Yang, and E. P. Shapiro. Human heart: Tagging with MR imaging - a method for noninvasive assessment of myocardial motion. *Radiology*, 169:59–63, 1988.